CR 114733
AVAILABLE TO THE PUBLIC

23671-6001-TU-00

(NASA-CR-114733) FEASIBILITY TEST OF A SOLID STATE SPIN-SCAN PHOTO-IMAGING SYSTEM (TRW Systems Group) 192 p HC $12.75 CSCL 14E

N74-17158

Unclas G3/14 30367

FEASIBILITY TEST OF A SOLID STATE SPIN-SCAN PHOTO-IMAGING SYSTEM

By N. P. Laverty

14 December 1973

Prepared under Contract NAS2-7592
by
TRW Systems Group, TRW, Inc.
One Space Park
Redondo Beach, CA 90278

for

AMES RESEARCH CENTER
NATIONAL AERONAUTICS AND SPACE ADMINISTRATION

23671-6001-TU-00

FEASIBILITY TEST OF A SOLID STATE SPIN-SCAN PHOTO-IMAGING SYSTEM

By N. P. Laverty

14 December 1973

Prepared under Contract NAS2-7592
by
TRW Systems Group, TRW, Inc.
One Space Park
Redondo Beach, CA 90278

for

AMES RESEARCH CENTER
NATIONAL AERONAUTICS AND SPACE ADMINISTRATION

CONTENTS

CONTENTS (Continued)

TABLES

TABLES (Continued)

TABLES (Continued)

ILLUSTRATIONS

ILLUSTRATIONS (Continued)

ILLUSTRATIONS (Continued)

1.0
SUMMARY

This report summarizes the results of a study conducted by TRW Systems Group under Contract No. NAS2-7592 from the NASA Ames Research Center to demonstrate the feasibility of using a solid-state photo-imaging system to obtain high resolution imagery from a Pioneer-type spinning spacecraft in future exploratory missions to the outer planets.

Feasibility has been demonstrated by the production of six images, simulating the characteristics of planets and satellites at distances from the sun from 5.2 AU (corresponding to Jupiter) to 19.2 AU (corresponding to Uranus). An experimental solid state photo-imaging system previously developed by TRW Systems used in these tests contained a linear array of 390 silicon phototransistors. This bipolar array, fabricated by triple diffusion in silicon, was developed by the TRW Microelectronic Center.

Photographic transparencies simulating the characteristics of the planets and satellites were illuminated to give exposure levels on the array corresponding to the levels that would be realized in the space flight application. Video data, recorded in digital form on magnetic tape, was used to produce photographic imagery by a laser-beam film recorder.

The photographs which were produced simulate monochrome imagery obtained in one spectral band from 0.4 to 1.1μm. The estimates of multispectral image quality presented in this report are based on the use of five spectral bands between 0.4 and 1.1μm, with spectral bandwidths corresponding to those of the experimental photo-imaging system developed by TRW. Reproduction of the multispectral imagery can be accomplished by a number of methods, one approach being to combine data from three of the spectral bands during ground data processing to produce conventional color photographs.

The quality of the monochrome imagery produced varies from acceptable to excellent, being highly dependent on the contrast of the simulated scene. A quantitative evaluation, based on the analysis of a photographic reproduction of a resolution chart, shows that a spatial resolution equivalent to the sampling (or Nyquist) frequency was obtained.

Evaluation of the photo-imaging system performance, based on electrical video signal analysis recorded on magnetic tape, shows that the signal-to-noise (S/N) ratios obtained at low spatial frequencies exceed the anticipated performance and that measured modulation transfer functions exhibited some degradation in comparison with the estimated values, primarily owing to the difficulty in obtaining a precise focus of the optical system in the laboratory with the test patterns in close proximity to the objective lens.

A preliminary flight model design of the photo-imaging system is developed based on the use of currently available phototransistor arrays. Image quality estimates that will be obtained are presented in terms of S/N ratios and spatial resolution for the various planets and satellites. Parametric design tradeoffs are also defined.

In addition, potential performance improvements are presented, based on anticipated advances in photodetector performance that may be realized in the near future.

2.0 INTRODUCTION

The organization of this report is as follows. Section 4 defines the scientific objectives for a typical photo-imaging experiment in future exploratory missions to the outer planets. The spectral variations in the geometric albedo of the planets considered in the study are presented.

Section 5 develops a preliminary design configuration of the photo-imaging system flight model, including the mechanical configuration, functional electronics diagrams, details of the signal processing method, and system specifications including the electrical interface definition with the spacecraft. The photo-imaging system performance is defined including estimates of image quality and image transmission capability when the planets Jupiter, Saturn, and Uranus are observed during typical encounters. The image transmission capability is defined with both linear encoding and delta modulation in the on-board processing of video data. Image quality estimates, as well as parametric tradeoffs in sensor design, are presented for instrument configurations, using both the currently available phototransistor arrays and improved photodetector arrays that may be available in the near future.

Section 6 presents the silicon phototransistor array characteristics which form the basis for the photo-imaging system design including details on physical, radiometric, and electrical characteristics. The performance is compared with contemporary television camera tubes (silicon diode array vidicon and silicon intensifier vidicon), and the susceptibility of the array to radiation is defined.

The method of performing the feasibility test demonstration, and the results obtained from the demonstration, are discussed in Section 7. First the equipment used in the tests is described in detail, including the experimental photo-imaging system, data collection facility, test pattern illuminator, software for processing video data, and the image reconstruction facility. An analysis verifies the validity of the radiometric exposure levels used in the laboratory tests as related to the exposure values that will be realized in space flight. The photographic test patterns used to simulate the planet and satellite characteristics are illustrated, and quantitative plots of the densimetric characteristics of the transparencies are presented.

The photographic reproductions obtained from the six simulated planetary images are qualitatively evaluated and quantitative data are presented from the results obtained by the reproduction of a photographic resolution chart.

A quantitative performance evaluation of the photo-imaging system is then presented based on analysis of the video data recorded on magnetic tape. This permits a true performance evaluation, eliminating degradation in the data quality due to dynamic range limitations of the recordings on photographic film.

3.0
SYMBOLS

Symbol	Description	Unit	Symbol for Unit
n_4	Photoelectrons generated during exposure interval	photoelectrons dc	–
a	Area of detector element	square meter	m^2
t_1	Exposure time	second	s
t_2	Optical transmission	percent	%
β	Solar phase angle	radian	rad
D_p	Solar distance	astronomical unit	AU
f	f-Number of optical system	–	–
h	Planck's constant	joule-second	J-s
c	Velocity of light	micrometer per second	μm/s
H_λ	Spectral solar irradiance	watts per square meter-micrometer	W/m^2-μm
ρ_λ	Spectral albedo of planet or satellite	percent	%
λ	Wavelength	micrometer	μm
$\bar{\lambda}$	Spectral quantum efficiency of photodetectors	photoelectrons per photon	–
S_4	Signal amplitude	photoelectrons, pk-pk square wave	
m_0	Modulation contrast of planetary object	percent	%
n_2	Noise on collector-base junction at end of charge cycle	electrons, root-mean-square	electrons rms
NES	Dark noise level, noise equivalent energy density-6000°K radiation temperature (0.4 – 8μm)	joule per square meter	J/m^2
D	Dynamic range of video signal above dark noise	–	–
n_5	Noise in signal processing electronics	electrons, root-mean-square	electrons rms
n_6	Quantization noise	electrons, root-mean-square	electrons rms
n_7	rss Value of random noise components	electrons, root-sum-square	electrons rss
n_8	rss Value of quantization noise and random noise	electrons, root-sum-square	electrons rss
S_9	Signal-to-noise ratio	current ratio	pk-pk square wave/rss noise
T(k)	Response of sensor to square wave of increasing spatial frequency	percent	%
n_1	Photoelectrons generated per unit of planet irradiance	photoelectrons, dc	–
n_9	Photoelectrons generated per unit of illuminator irradiance	photoelectrons, dc	–
f_1	Effective f-number of experimental photo-imaging system	numerical value	–
t_λ	Spectral transmission of experimental photo-imaging system	percent	%
S_λ	Spectral irradiance of test pattern illuminator	watts per square meter	W/m^2-μm
E	Exposure on phototransistor array	joules per square meter	J/m^2
R	Ratio of test pattern radiance of 2650°K radiation temperature to planetary radiance for generation of equivalent number of photoelectrons	numerical value	–
n_{max}	Electron charge induced by test pattern highlight	photoelectrons, dc	–
n_{min}	Electron charge induced by test pattern lowlight	photoelectrons, dc	–
$\overline{NES}$	Average noise level induced by irradiance on array (Noise equivalent energy density – 6000°K radiation temperature, 0.4 – 0.8 μm)	J/m^2	–

4.0
SCIENTIFIC OBJECTIVES OF PHOTO-IMAGING EXPERIMENT

The scientific objectives of a typical photo-imaging experiment in future exploratory missions using a spinning spacecraft of the Pioneer type which have been considered in this study as follows:

a. To obtain imagery of the sunlit portions of the planets Jupiter, Saturn, and Uranus from the spacecraft for a period of about one week, when the distance from the planet decreases from about one hundred planet radii to a minimum value of two to ten radii, depending on (1) the encounter trajectory periapsis distance, (2) the location of the periapsis relative to the planet–sun direction, and (3) possible interference, in the case of Jupiter, from the high-energy electron belts with 10 planet radii. The imagery of Jupiter will have higher resolution to that obtained in the best photographs from the earth (1000 km) by a factor between 10 and 50 (20 to 100 km). This imagery may be obtained using the full spectral range of the phototransistor array, or (as an option) using narrow-band optical filters to obtain multispectral imagery.

   The imagery obtained can be used for the following areas of investigation:

   1. Delineation of the structure of the visible surface of the planets at high spatial resolution. In the case of Jupiter, this would include detailed representations of belts, zones, and their boundaries, as well as transient features of the belts and zones and the Great Red Spot

   2. By comparison of successive images, observations of the temporal variations of transient features would be indicative of circulation and other meteorological characteristics

   3. By the use of several spectral filters, improved data could be obtained of the reflectivity of the visible surface as a function of latitude at several wavelength intervals

   4. Correlation with measurements taken by other instruments. In particular, correlation with data obtained by a scanning infrared radiometer would be of value. While the infrared instrument would provide high temperature resolution at low spatial resolution, the optical photo-imaging experiment would obtain correlative data in the visible region of the spectrum with high spatial resolution

5. Correlation with earth-based observations. With the proper selection of the date of arrival of the spacecraft, the planet-earth-sun angle geometry could permit observation of the planet after sunset from the observatories on the earth

6. Possible determination of the altitude structure of cloud formation from imagery obtained of the terminator. Photographs of the terminator from nearly overhead will point out altitude irregularities of a mottled nature (like the surface of an orange peel), in a manner similar to photographs obtained of lunar craters near the terminator. If the altitude differences are functions of latitude only, photographs from the spacecraft at an angle of approximately 135 deg to the sun line may indicate these differences by apparent irregularities in the terminator

7. Determining the visible aspect of high latitude regions. As in the observation of the terminator, observation of high latitude regions cannot be made from earth-based or earth-orbiting instruments. Images of high latitude or polar regions of Jupiter can be obtained from a passing spacecraft; however, this requires an encounter trajectory which is substantially inclined to the equatorial plane of Jupiter.

b. To obtain imagery of the satellites of Jupiter and Saturn. In the case of Jupiter, the satellites are in orbits which are nearly circular and close to the equatorial plane. The orbital radii range from 6 to 26 Jupiter radii from the planet center for the four major satellites. The specific geometry of the trajectory of the spacecraft relative to these satellites depends upon the encounter targeting near Jupiter as well as on the time of arrival. However, it is likely that any trajectory selected for investigation of the environment of Jupiter will also provide opportunities for observations of the satellites from distances of no more than 10 Jupiter radii, so that the resolution obtained would be at least an order of magnitude better than that of the best current earth-based observations. It is reasonable to assume that improving the resolution from 1000 km to 100 km will reveal a great deal of additional information about the nature of satellites with diameters from 3000 to 5000 km. Specifically, the following information may be obtained:

1. Gross surface features may be observable, providing information regarding the physical structure of the satellites

2. Successive images may offer the possibility of determining rotation rates of the satellites about their own axes

3. With more accurate determination of satellite diameters, their albedos and densities may also be estimated more accurately.

While these objectives can be expected to be attained when the spacecraft is targeted solely on the basis of mission considerations not involving the Jovian satellites, specific targeting which aims toward a close encounter with one of these satellites would offer the opportunity to improve the resolution of the imagery even further. Such specific targeting, in all probability, could be incorporated without significantly detracting from other mission objectives, which are more closely related with the planet and its environment rather than with the satellites.

c. To obtain distant imagery of the planets for the purpose of correlation with the navigation of the spacecraft in the vicinity of the planets. These images could be taken a number of weeks or months prior to encounter, and similarly, several weeks or months after encounter.

4.1 Planets and Planetary Satellites Considered

In the design study, the following planets and planetary satellites were selected. These selections are consistent with those planets being considered by NASA for future exploratory missions.

TABLE I. — PLANETS AND PLANETARY SATELLITES CONSIDERED IN DESIGN OF PHOTO-IMAGING SYSTEM

Planet or Planetary Satellite	Distance From the Sun, AU	Geometric Albedo
Jupiter	5.20	See Figure 7
Io	5.20	0.92
Europa	5.20	0.85
Saturn	9.55	See Figure 7
Titan	9.55	0.32
Uranus	19.2	See Figure 7

Data on the values of the solar distances were obtained from Reference 1, as were the numerical values of albedo for Io and Europa. The value of albedo for Titan was obtained from Reference 2. For the three planets, spectral albedo data as defined in Figure 1, were used, obtained from Reference 3.

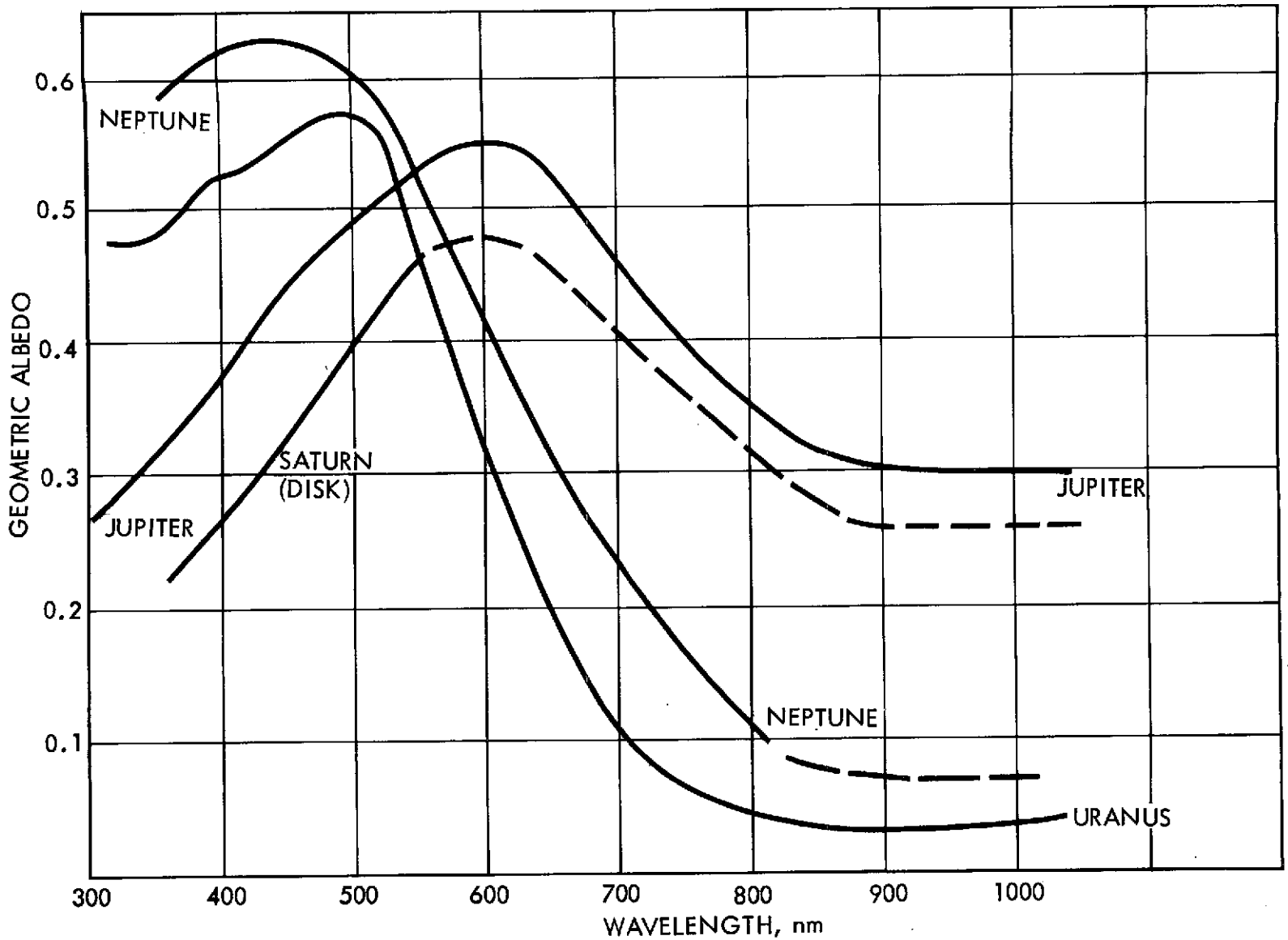

FIGURE 1. — GEOMETRIC ALBEDOS FOR OUTER PLANETS

5.0
PHOTO-IMAGING SYSTEM FLIGHT MODEL CONFIGURATION

A preliminary design configuration of the photo-imaging system flight model has been developed, compatible with the Pioneer-type spacecraft characteristics in future missions to the outer planets. The primary emphasis in developing this design was to obtain high resolution imagery of the outer planets and their satellites, higher by one to two orders of magnitude than the resolution that can be obtained in earth-based photography. The preliminary design configuration has not been detailed completely, but is presented in sufficient depth to give a representative sizing of the photo-imaging system.

In addition to obtaining monochrome imagery in one spectral band, from 0.4 to 1.1 μm, multispectral imaging capability is provided. Multispectral data can be obtained sequentially in five spectral bands from 0.4 to 1.1 μm.

The design parameters of the photo-imaging system are based on using currently available bipolar silicon phototransistor arrays. To obtain the maximum performance (S/N ratio and resolution) from these devices, a low f-number (f/1.23) optical system is used as a baseline design. A catadioptric configuration, similar to the Farrand catadioptric lens system No. 1, is recommended to minimize weight, which would greatly increase if a refractive optic were used.

In the near future, improved photodetector arrays, currently in the developmental stage, may become available. The anticipated reduction in dark noise level and a corresponding increase in sensitivity will allow a reduction in the optical system diameter permitting the use of a small refractive optic if maximum performance from the imaging system is not required.

The system configuration for either type of photodetector is based on 8-bit digital video signal encoding to obtain low-noise imagery over the 1000/1 dynamic photodetector range. With the phototransistors, an additional two bits is required to measure the variations in detector responsivity and dark current. Only one additional bit will be required when the improved photodetectors are used.

For preflight or inflight calibration, an eight-step gray scale (dark plus eight gray shades) will be required with the phototransistors, whereas only a two-point calibration – dark and maximum illumination level – will be required with the improved arrays.

The mechanical, electrical, and performance characteristics of the photo-imaging system are described in the following sections.

5.1 General Description

A conceptual illustration of the photo-imaging system, installed in an outer planets Pioneer type of spacecraft is presented in Figure 2, and a design layout is shown in Figure 3.

The sensor head assembly will consist of the phototransistor arrays, the optical system, a folding mirror, and a six-position color filter selector (five spectral filters and one clear aperture), as well as a circular variable neutral density filter wheel. The functions of the neutral density filter wheel are (a) to control the exposure on the photodetector array with variation in the cone angle (pointing angle) of the pointing mirror, thus compensating for the exposure increase at small cone angles, and (b) to provide a gray scale for periodic in-flight calibration using an internal calibration lamp. In addition, this assembly will contain the preamplifiers, multiplexer, subprogrammers, and electronics required for multiplexing the analog signals from the photodetector arrays prior to digital encoding of the video data.

Above the sensor head assembly, an elliptical pointing mirror will direct the optical line-of-sight toward the desired planet or satellite, with the cone angle variation covering the range of 70 to 175.5 deg from the spin axis of the spacecraft.

The effective field-of-view of the optical system is 0.15 mrad x 58.5 mrad (31 arc-s x 3.35 deg), with the field-of-view plane parallel to the spacecraft spin axis. Spacecraft rotation provides the motion necessary to scan the object plane. The nominal size of one frame of imagery will be 3.35 x 3.35 deg. With the photo-imaging sensor operating in a "pushbroom" scanning mode at distances

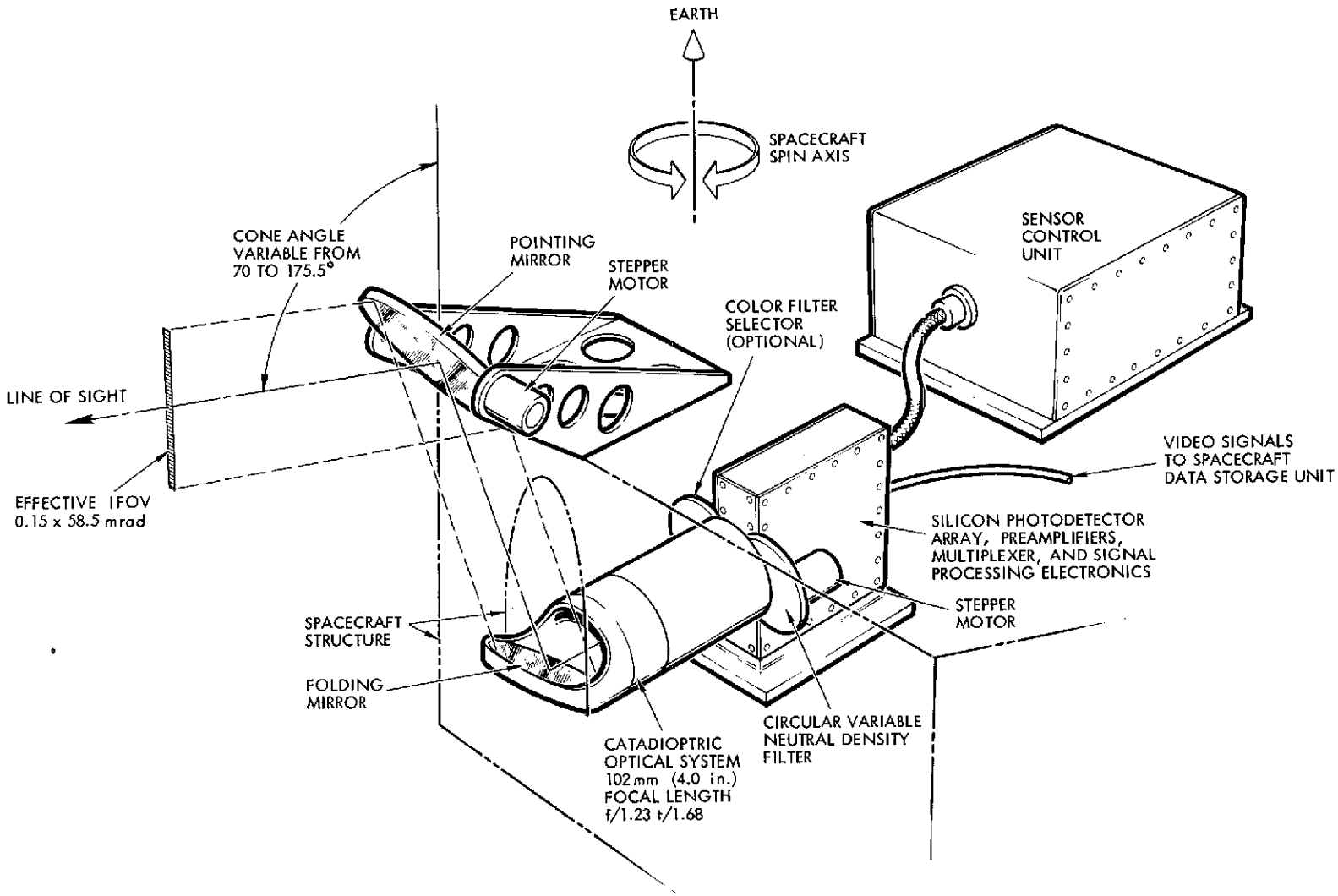

FIGURE 2. – PHOTO-IMAGING SYSTEM INSTALLATION ON OUTER PLANET SPACECRAFT

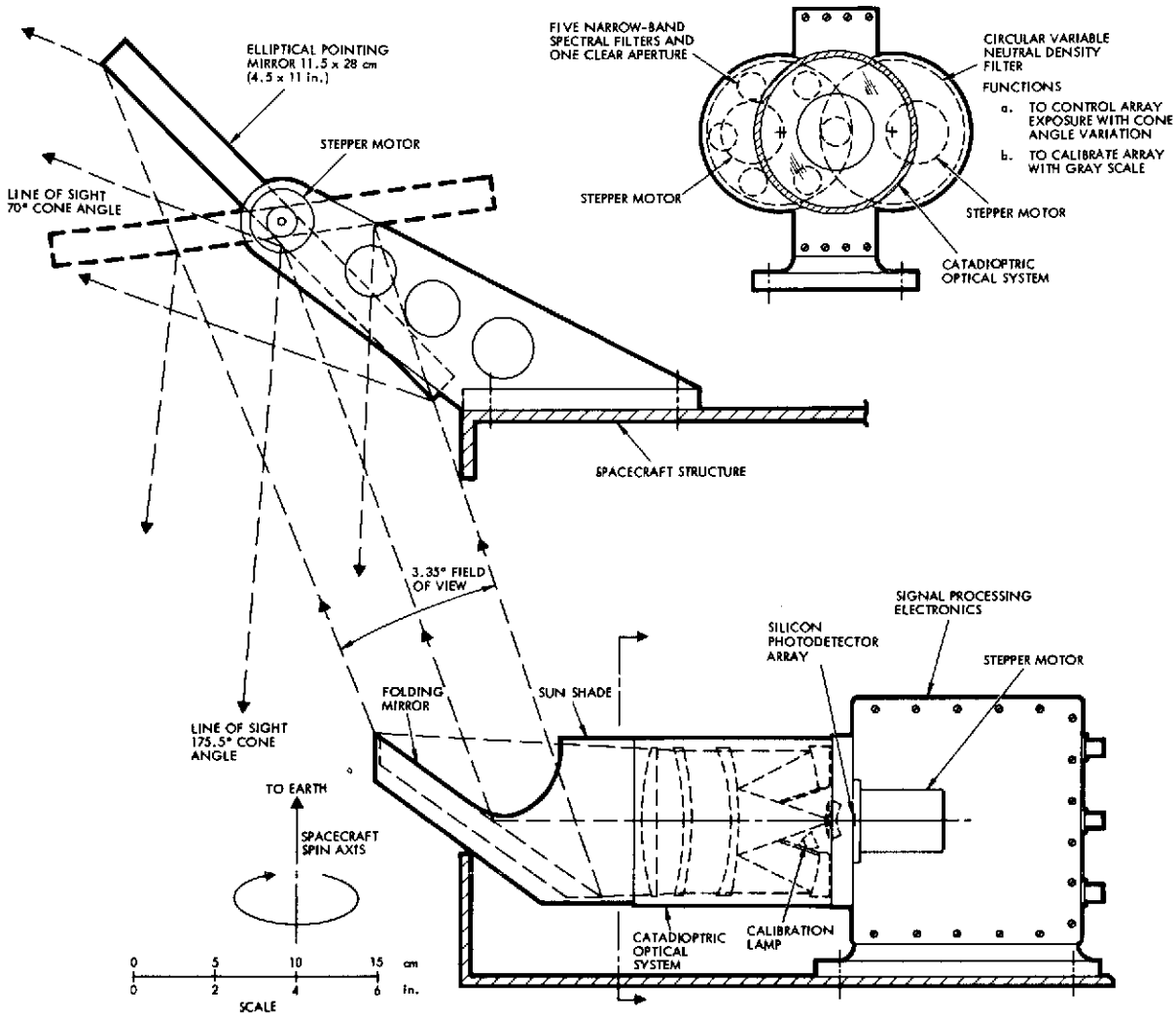

FIGURE 3. – DESIGN LAYOUT OF SOLID STATE SPIN-SCAN PHOTO-IMAGING SYSTEM

from a planet where the object is contained within the 3.35 deg angular field-of-view, a complete image of the planet will be obtained during a small fraction of one spacecraft revolution.

The positions of the color filter wheel, circular variable neutral density filter, and pointing mirror will be controlled by incremental stepping motors in turn controlled by input signals consisting of a series of narrow pulses. Stepper motors of the type used on the spin-scan cloud camera in the ATS satellite are proposed (IMC Magnetics Model 015-802), inasmuch as these components have been proved in space flight. By using the same type of stepper motor for all three of these functions, and by sequential operation of the pointing mirror, filter wheel, and neutral density filter, it will be possible to time-share a common set of control electronics for the three stepper motors.

The sensor control unit will contain the electronic servo control circuit for the stepper motors as well as the programmer that will control the timing functions for the sensor head assembly electronics. In addition, the power supply regulation circuits will be housed within the control unit.

From the sensor head assembly, the video output signals will consist of five multiplexed lines of analog data, fed through coaxial cables to five D/A converters. These converters should be located in close proximity to the digital memory within the spacecraft data storage unit. This arrangement will provide an optimum interface between the A/D converters and the memory by permitting 10-bit data from the five converters to be supplied in parallel on five groups of ten lines, at a rate of 0.5 Mb/s. By using multiple parallel inputs to the memory, rather than a smaller number of serial inputs, the power requirement of the memory during the write-in cycle is minimized.

5.2 Electronic Configuration

A functional diagram of the major photo-imaging system elements is illustrated in Figure 4, including a summary of the interfaces with the spacecraft. Table II summarizes input and output signals. The interfaces are configured for compatibility with the characteristics of an outer planet Pioneer

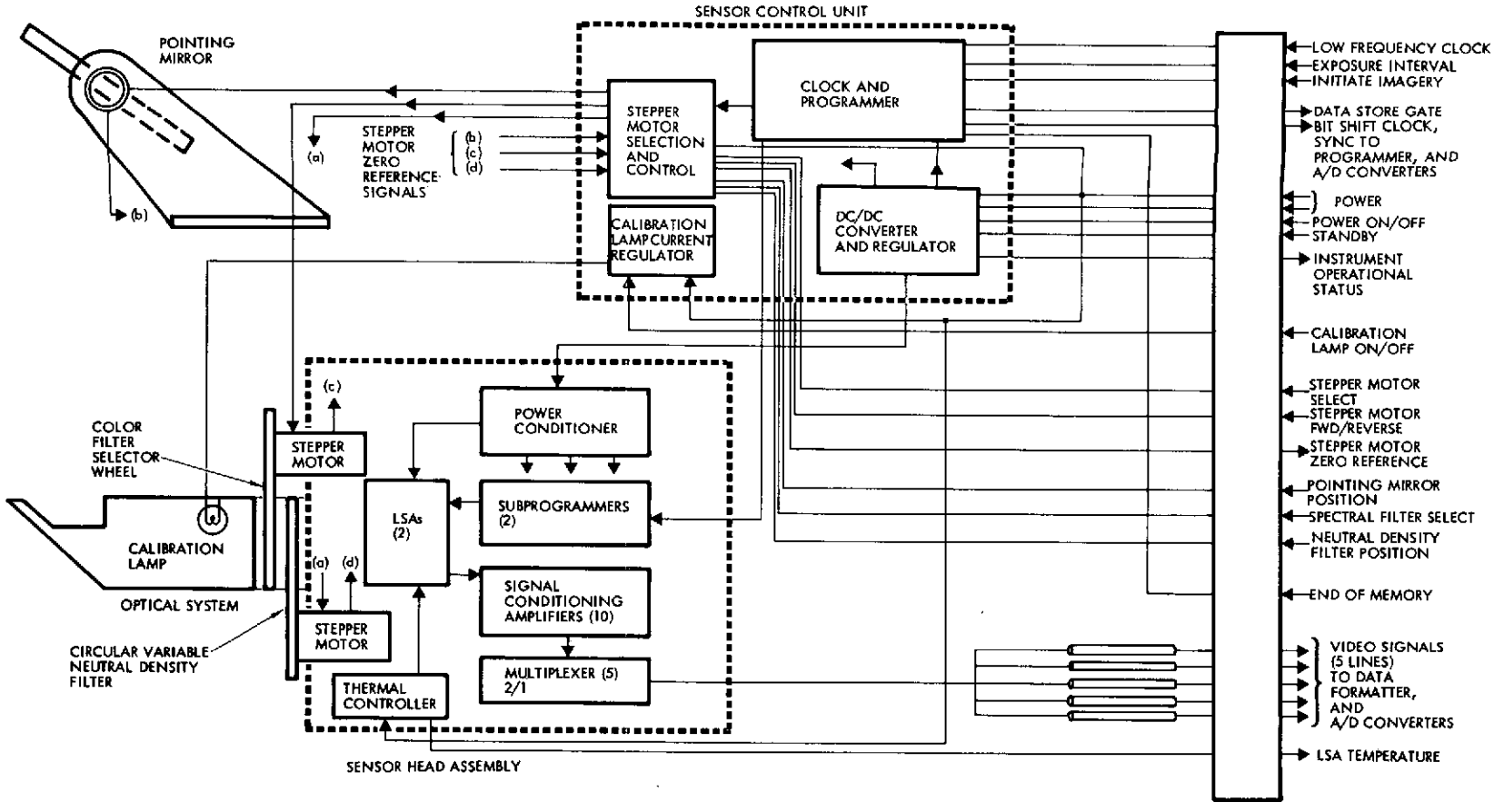

FIGURE 4. – FUNCTIONAL DIAGRAM: PHOTO-IMAGING SYSTEM

TABLE II. – SUMMARY OF INPUT AND OUTPUT SIGNALS

Item	Description	Source
Inputs to Photo-Imaging System		
Power	+28 Vdc	Spacecraft Power Supply
Power ON/OFF	Pulse (ground command)	CDU[a]
Standby	Pulse (ground command)	CDU
Stepper motor select	Pulse (ground command)	CDU
Stepper motor fwd/rev	Pulse (ground command)	CDU
Pointing mirror position	10-Bit word (ground command)	CDU
Spectral filter select	7-Bit word (ground command)	CDU
Neutral density filter position	7-Bit word (ground command)	CDU
Exposure interval	12-Bit word (ground command)	CDU
Initiate imagery	11-Bit word (ground command) (Referenced to roll index pulse)	CDU
Calibration lamp ON/OFF	Pulse (ground command)	CDU
Low frequency clock	2048 Hz	DTU[b]
End of memory	Pulse at last memory location	DSU[c]
Outputs From Photo-Imaging System		
Bit shift signal Sync to programmer, A/D converters, and DSU	0.5 MHz square wave	Programmer
Data store gate	Gate, 0.112- to 3.549-s duration	Programmer
Video signals	Five coaxial lines Multiplexed analog data Sampling rate = 0.5 Ms/s 780 bursts of data/line Burst duration = 78 μs	Sensor head assembly
Stepper motor zero reference	One bilevel signal	Stepper motor
Instrument operational status	Five bilevel signals	DC/DC converter and regulator
LSA temperature	One bilevel signal	LSA thermal control

[a]Command Distribution Unit

[b]Digital Telemetry Unit

[c]Data Storage Unit

type of spacecraft (Table III) developed by the NASA Ames Research Center (Reference 5). The data on C-MOS memory characteristics in the table are a subsequent contribution by TRW Systems.

A power level of +28 Vdc will be supplied to the photo-imaging system from the spacecraft, with subsequent power conversion within the sensor by a dc/dc converter. Functions within the sensor will be timed by a crystal-controlled clock operating at a frequency of 4.0 MHz. The clock will provide timing for the programmer, which in turn controls the two LSA subprogrammers providing the read, erase, and bias timing functions.

A submultiple frequency of the clock in the programmer, 0.5 MHz, will be generated within the programmer and used as both a bit shift signal and a timing reference for controlling the LSA exposure interval. The output at this frequency will be accumulated and compared with a 12-bit word from the command distribution unit (CDU) obtained from ground command. The exposure interval will vary with both the spacecraft spin rate and the cone (pointing) angle. This word length provides integration intervals over a range of 0.286 to 9.01 ms, with quantization of 1.4% of the former value, thus maintaining linearity of the imagery to this level at the highest spin rate (5 rpm). Imagery initiation during the spin cycle will be controlled by one 11-bit word, referenced to the roll index pulse of the spacecraft, provided by a star sensor (observing Canopus). The 11-bit word will provide a quantization increment of 10.5 arc-min for the roll index pulse.

The video signals from the sensor head assembly will be furnished on five coaxial lines, with analog signals on each line consisting of multiplexed data sampled at the rate of 0.5 ms/s. For a complete frame of imagery, there will be 780 bursts of data per line (using two LSAs and 390 lines per frame of data). The duration of each burst will be 78 μs, consisting of the output of 39 photodetector elements with a sampling width of 2 μs per sample. Additional details on the video signal processing circuit are contained in the second part of this discussion.

In conjunction with the video signals, the programmer will provide a data store gate to the data storage unit (DSU) of the spacecraft. This gate will vary in duration from 0.112 to 3.549 s, corresponding to the length of one frame of imagery with the duration dependent on the spacecraft spin rate and the cone angle (pointing angle of the line-of-sight).

TABLE III. – SUMMARY OF OUTER PLANET PIONEER SPACECRAFT PARAMETERS

Parameter	Value
Science Payload Complement	
Weight	40.8 kg (90 lb)
Power	45 W
Spacecraft Spin Rate	4.8 rpm ±20% (nominal), 2 rpm (minimum)
Telemetry	
Frequency	X-band (8.4 GHz)
Power	12 W
Data Rate (50% available for transmission of imagery)	
At Jupiter	16,384 b/s
At Saturn	4,096 b/s
At Uranus	1,024 b/s
Data Storage (Capacity)	Capacity: — Weight (kg/lb): — Volume (cm^3/in^3): — Power (W): — Status: —
C-MOS Solid State Memory	Capacity: 0.307 Mb; Weight (kg/lb): 1.00/2.2; Volume (cm^3/in^3): 1369/84; Power (W): 1.0 (Write-In), 0.67 (Readout), 0.40 (Hold Mode); Status: Flown on several NASA spacecraft. Proposed for HEAO
Attitude Control	
Spin Rate	Controllable to ±0.1% at nominal spin rate of 4.8 rpm
Attitude Measurement	
Roll Attitude (spin)	Telemetered to ±0.5°
Spin Axis	Telemetered to < 0.15° when pointing error to earth is < 2°
Electrical Power	±28 Vdc ±1% short term deviation ±1% long term drift with 0.1 V to 0.2 V drop-through fuse and wiring
Thermal Control	Control of experimental equipment 0 to 90° F in equipment compartments. External experiments must provide own temperature control
Signals Available to Scientific Instruments	
Roll Index Pulse	One pulse per spacecraft revolution
Roll Index Pulse Jitter	< 0.5° using Canopus reference, < 1.25° using Sun reference
Sector Generator Pulse	512, 64, and 8 pulses per spacecraft revolution
High Frequency Clock	32.768 KHz
Low Frequency Clock	2.048 KHz
Word Gate	Indicates time of reading out digital data to telemetry
Function Commands	Pulse on receipt of ground command
On-Off Commands	Step signal on receipt of ground command
End of Memory	A pulse when Data Storage Unit reaches last memory location.

A bit shift signal also will be provided to the DSU at a rate of 0.5 MHz, roviding synchronization for the programmer, the A/D converters, and the pacecraft memory, which will be located near the spacecraft memory in he DSU.

Data will be written into the memory in synchronism with the bit shift ignal from the photo-imaging system and will be read out in synchronism ith clock signals from the digital telemetry unit (DTU).

It is proposed that five C-MOS memory units of the size specified in Table III, be used to accommodate the 1.52-mb data load from the imaging ensor during one frame time. Each of the five units will consist of ten layers, ith each layer providing 120 x 256 bits of memory, for a total of 307,200 bits er unit. C-MOS memories have been flown in several NASA spacecraft programs and are proposed by TRW Systems for use on the High Energy Astronomical Observatory (HEAO).

Stepper motor operation will be performed in the following manner. nasmuch as the three stepper motors can be operated in sequence, a common et of control electronics can be used, selected by ground command. The motors operate on 10 ms input pulse providing a 90^{o} motion of the stepper motor. The motors will be geared down using the following procedure. For mirror pointing, 1024 increments will be used to cover the pointing range in one angle for 70 to 175.5 deg (105.5 deg of motion of the line-of-eight, and 52.8 deg of mirror motion). This will provide a line-of-sight pointing of ncrements of 6.2 arc-min.

The timing reference will be the low frequency spacecraft clock at 2.048 KHz. The frequency will be reduced to 2 Hz by a 10-stage counter. The stepper motor will be operated at two pulses per second during the return to he zero position, requiring 512 seconds or 8.5 minutes to return to zero from maximum displacement. Prior to the photo-imaging sequence, the mirror will be slewed to a new position at the pulse rate of two per second, with the mirror position defined by a 10-bit word from ground command. At this rate, the verage power requirement of the stepper and control circuit is 0.5 W. During the photo-imaging sequence, where the rate of change of the line-of-sight is very low, requiring only two increments per minute (as in a typical Jupiter encounter), the average power requirement will be only 0.01 W.

The neutral density filter wheel will operate in a similar manner. Primarily, the filter provides an increase in filter density and reduction in array exposure as the cone (pointing) angle is reduced, thus preventing over-exposure of the array because of the increase in dwell time at small cone angles. A secondary function provides an eight-step gray scale (dark plus eight light levels) for in-flight calibration of the array using the calibration lamp. In this case, the stepper motor would be geared so that 128 steps will provide a full rotation over the full filter density range.

To compensate for cone angle changes, the rate of incrementing the filter wheel will be very slow, with very low power consumption, in the order of 0.01 W. During calibration, the wheel will be incremented at the rate of two pulses (or increments) per second, with a power consumption of 0.5 W. The position of this wheel will be controlled by a 7-bit word from ground command.

For the spectral filter selector wheel, which has only six positions (five filters plus one clear aperture), 128 steps for a complete rotation will again be used. However, to change the selection of filters, it is proposed that the stepper motor be pulsed at only one pulse per second. The time required to move from one filter position to the adjacent filter would be 21 seconds. By the use of the lower pulse rate, the average power consumption will be 0.25 W. The position will be controlled by a 7-bit word from ground command.

Signal Processing Electronics

The photo-imaging system photodetectors consist of two large-scale arrays (LSAs), each consisting of a linear array of 195 detector elements, aligned to form a single 390 element array.

The phototransistors operate in an electron charge storage mode (Figure 43), in which the photon-generated current discharges the capacitance of a reverse-biased p-n junction from a preset charge level. The current required to recharge the capacitance during the readout interval is proportional to the irradiance on the array elements. After the current generated by each detector element during the integration interval is sampled, the remaining charge on the photojunction is erased, and the photojunction is then biased in preparation for the next integration interval.

Located on the microelectronic LSA chip are 195 preamplifiers, switches, and a shift register (Figure 23). By the use of the shift register, five groups of 39 detector elements on each LSA are interrogated in-parallel, with serial readout of the 39 elements. The outputs of the five 39-element groups are then amplified by five amplifiers in a microelectronic signal conditioning electronics (SCE) chip, mounted on the same substructure as the LSA chip.

In this application, the nominal integration or exposure time will vary from 0.286 to 9.10 ms, depending on the spacecraft spin rate and the cone (or pointing) angle of the line-of-sight from spacecraft to planet. The time required for sampling signal current from each element of the array is 2 μs. For each group of 39 elements, the total sampling time is 78 μs.

By operating the two LSAs in sequence (Figure 5), common A/D conversion electronics can encode the signal analog amplitude from the photodetector elements in each of the two arrays. In Figure 5, the five analog outputs of the first LSA are designated A_1, B_1, C_1, D_1, and E_1, and the outputs of the second LSA are designated A_2, B_2, C_2, D_2, and E_2.

The five outputs from each of the two arrays are amplified by two sets of five signal conditioning amplifiers in the signal processing electronics unit (Figure 6). The two groups of five signals are then multiplexed at a low rate to permit subsequent time-sharing of the digital encoding electronics.

Two alternate encoding methods are illustrated, i.e., linear and differential pulse code modulation (delta modulation). In the linear method, the current sample from each detector element is processed by a sample-and-hold circuit and then converted to digital form by a 10-bit A/D converter. A/D conversion occurs at the rate of one conversion every 2 μs. The outputs from the A/D converters are stored in a shift register and then multiplexed onto ten parallel lines, with an output data rate on each line of 0.5 mb/s. These data are then sent to a data formatter. The formatter is used to format data prior to spacecraft memory storage and to insert a frame sync code.

If the alternate method of differential pulse code modulation rather than linear encoding is desired, the number of imagery frames transmitted during a mission can be increased. In comparison with 10-bit linear encoding, the

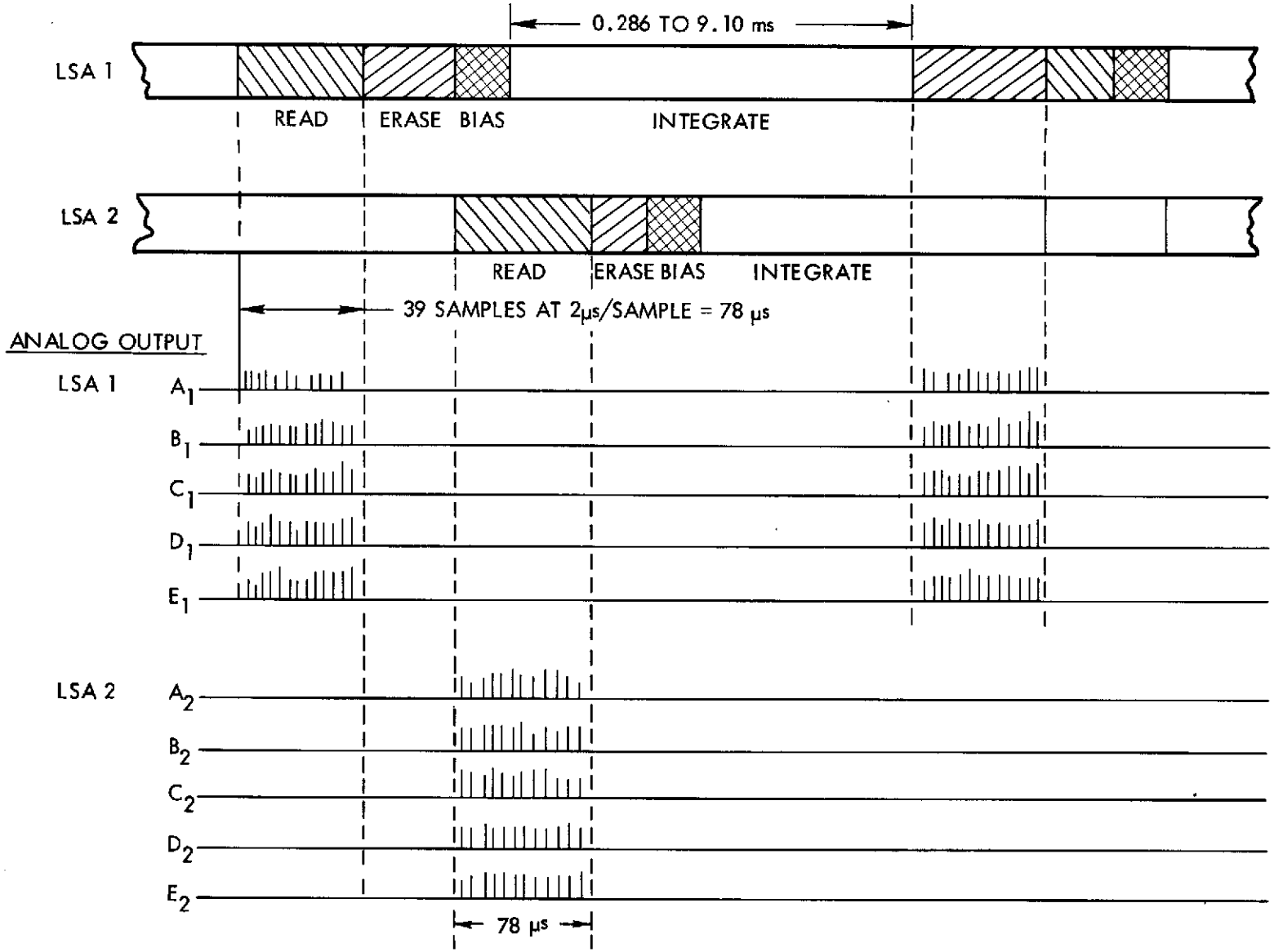

FIGURE 5. – LSA READOUT SEQUENCE

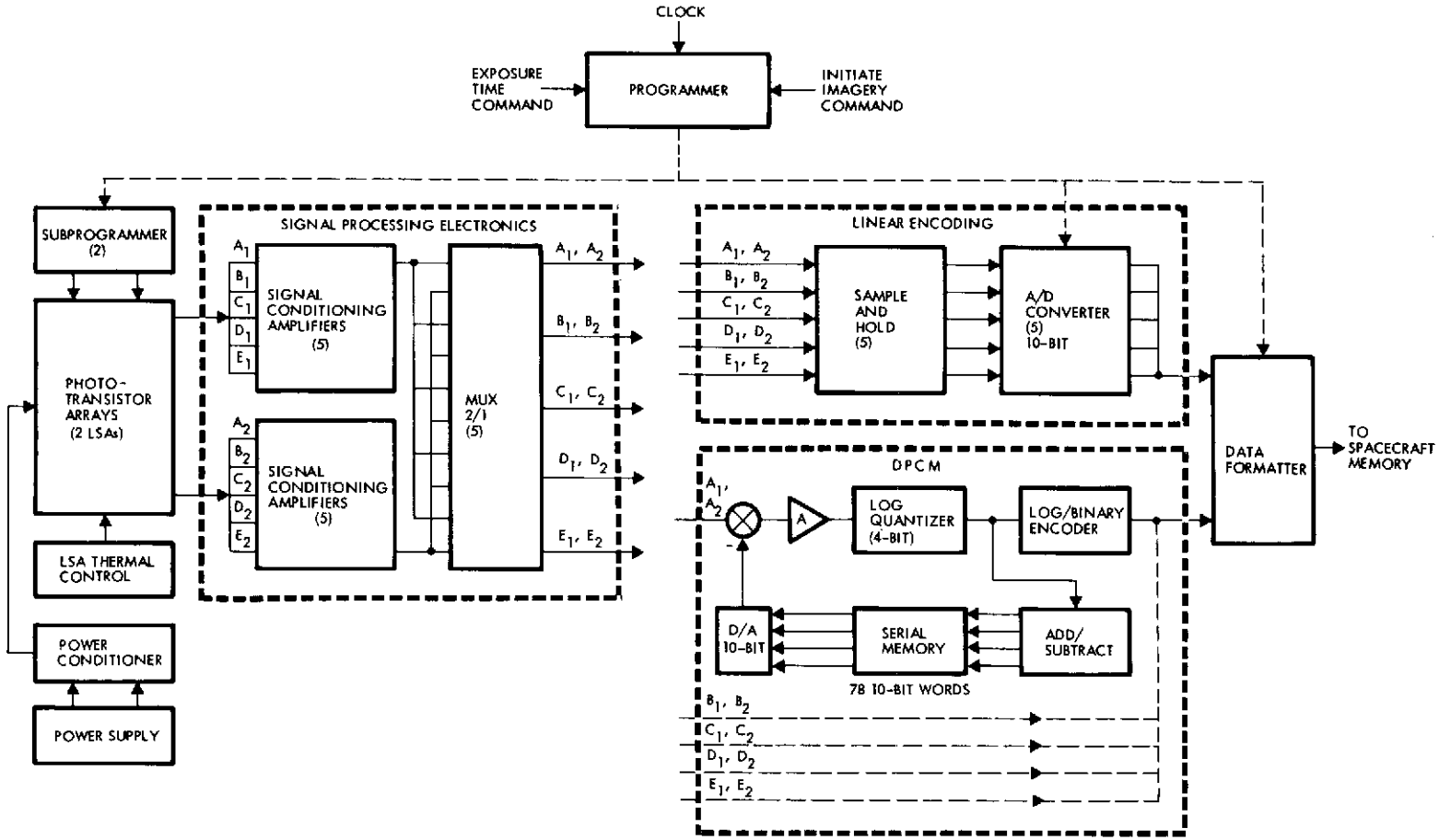

FIGURE 6. – FUNCTIONAL DIAGRAM OF SIGNAL PROCESSING (LINEAR ENCODING OR DPCM)

use of 4-bit delta modulation will increase the number of data frames by a factor of approximately 2.5.

The method illustrated in Figure 5 is that of a 4-bit logarithmic DPCM with periodic transmission of the absolute data value using 10-bit linear encoding. Figure 5 illustrates one of the five delta modulation channels. The last absolute measure of data from each detector is stored in a MOS shift register memory, which is shifted in synchronism with the incoming data samples. The shift register memory drives a 10-bit D/A converter that produces an analog current to be subtracted from the input signal. The signal representing the difference is encoded by the logarithmic quantizer, consisting of 16 parallel comparators, and a 4-bit delta word is generated in serial form as an output signal. In addition, the delta word is binarily weighted and is added to, or subtracted from, the D/A input signal. This updates the present signal value estimate from one detector element and is then returned to memory to be used during the next quantization interval.

Periodically, the absolute signal value from each detector element will be transmitted. Ten 10-bit words are held in refresh storage memory for each data line and inserted into the output after each LSA interrogation. In this manner, the absolute output value from each detector element is transmitted for every 39 detector output samples.

Using delta modulation, the periodic insertion of the 10-bit whole word of data into the data stream will be performed by the formatter.

Additional signal processing electronics elements include the programmer containing count-down chains for generating LSA subprogrammer timing signals, A/D encoding logic, and the data formatter. The programmer will be controlled by an internal crystal-controlled clock and will receive an exposure (integration time) command for the LSAs. The length of the exposure time is a function of spacecraft spin rate and the cone (pointing) angle of the line-of-sight. The programmer will also receive a spacecraft command to initiate the accumulation of image data based on the line-of-sight position related to the spacecraft attitude within the roll (spin) cycle.

The two LSA subprogrammers used to control the shift register on the LSA chip, the switching and clamping functions within the photodetector

preamplifiers, and to provide timing signals for erasing and applying bias to the photo-junctions prior to the integration interval.

Phototransistor array temperature control is provided by a heating element maintaining a constant ±0.5°F to minimize variations in signal current offset because of dark current variations.

The estimated signal processing electronics, parts count and power requirements using either linear encoding or delta modulation, are defined in Table IV.

To reduce the power requirement when using linear encoding, the use of A/D converters based current thin-film hybrid circuit technology is assumed. In comparison to conventional A/D converters using discrete components, with 6-W power requirement for each converter, using thin-film hybrid design will reduce this requirement to one watt.

If delta modulation is used, the electronic elements designated in the table will be fabricated using a combination of thin film and medium-scale integrated chip technology, with the design optimized for the data rates of this application.

5.3 Specifications

A summary of preliminary specifications for the photo-imaging system is presented in Table V, based upon the preliminary design configuration developed in this study. As noted in Table IV, the power estimates for the linear encoding electronics are based on the use of thin-film hybrid A/D converters to be developed specifically for this application, using currently available technology. The power estimates for the delta modulation electronics are also based upon the development of several components for this application, using currently available thin-film/MSI technology. In both cases, the configuration of the specialized components will be optimized for the output data rates of the photo-imaging system.

TABLE IV. – PARTS COUNT AND POWER ESTIMATE,
SIGNAL PROCESSING ELECTRONICS

Component	Linear Encoding		Delta Modulation	
	Parts	Power	Parts	Power
Clock and Programmer (1)	20	0.8	20	0.8
Array electronics				
LSAs (2)	2	0.1	2	0.1
Subprogrammer (2)	30	0.3	30	0.3
Amplifier (5)/Mux (5)	20	0.2	20	0.2
Power conditioning (1)	60	0.4	60	0.4
Thermal controller (1)	65	0.5	65	0.5
	177	1.5	177	1.5
Linear Encoding				
Sample and hold (5)	75	5.0		
A/D converters (5)[a]	40	5.0[a]	N/A	
	115	10.0		
DPCM				
Amplifier (5)			20	1.0
D/A (5)			5	1.3[b]
Serial memory (5)			100	2.5
Adder (5)	N/A		30	2.0[b]
Quantizer (5)			60	2.0[b]
Log/binary logic (5)			20	0.5[b]
			235	9.3
Formatter (1)	50	1.5	50	1.5
dc/dc converter (1)	46	2.8	46	2.6
Totals	408	16.6	528	15.7

[a]Using thin-film hybrid technology

[b]Using thin-film and MSI technology

TABLE V. – PHOTO-IMAGING SYSTEM SPECIFICATIONS

System Parameter	Specification
RADIATION DETECTOR	
Type	Silicon phototransistors
Configuration	Linear array
Number of photodetectors	390
Dynamic range	100/1
OPTICAL SYSTEM	
Configuration	Catadioptric
f-number	1.23
t-number	1.68
Focal length	10.2 cm (4.0 in.)
Diameter	9.5 cm (3.8 in.)
Instantaneous field of view	31 arc-s x 3.35 deg
SPECTRAL RANGE	
Broad-band	0.4 – 1.1μm
Multispectral	0.4 – 0.5μm 0.5 – 0.6μm 0.6 – 0.7μm 0.7 – 0.8μm 0.8 – 1.1μm
IMAGE DATA	
Frame size	3.35 x 3.35 deg 390 x 390 TV lines
Pixels/line	390
Pixels/frame	152, 100
Encoding level	
Video	8 bits[a]
Dark current, LSA gain	2 bits[a]
Data bits/frame	
With linear encoding	1.521 Mb
With 2.5/1 data compression	0.608 Mb
Line exposure time	
For ω S/C = 5 rpm	0.286 ms[b]
For ω S/C = 2 rpm	9.10 ms[c]

System Parameter	Specification
IMAGE DATA (cont'd)	
Frame scan time	
For ω S/C = 5 rpm	0.112 s[b]
For ω S/C = 2 rpm	3.549 s[c]
Transmission time/frame[d]	
Without data compression	$3_m\ 6_s$ at Jupiter $12_m\ 23_s$ at Saturn $49_m\ 31_s$ at Uranus
With data compression (2.5/1)	$1_m\ 14_s$ at Jupiter $4_m\ 57_s$ at Saturn $19_m\ 48_s$ at Uranus

Physical Characteristics			Power (W)	
	Weight (Kg/lb)	Volume (cm^3/$in.^3$)	Photo-imaging linear/ΔMod	Calibration linear/ΔMod
Sensor Head Assembly	4.3 / 9.5	3810 / 232	1.5	1.5
Pointing Mirror and Structure	2.2 / 4.9 (50% lightweight)	6520 / 396	See item below	
Sensor Control Unit	6.2 / 13.6	6280 / 384		
Clock/programmer			0.8	0.8
dc/dc converter			2.8 / 2.6	2.8 / 2.6
Stepper motors			0.01	0.5
Digital encoding electronics (in S/C DSU)	2.0 / 4.4	2070 / 126		10 / 9.3
Encoding electronics			10 / 9.3	10 / 9.3
Formatter			1.5	1.5
Calibration Lamp				0.2 / 0.2
TOTALS	14.7 / 32.4	18,680 /1138	16.6 / 15.7	17.3 / 16.4

[a] 1 bit with improved photodetectors

[b] At 90° cone angle

[c] At 175.5° cone angle

[d] Using one-half of available data bandwidth

5.4
Performance

The image transmission capability of the proposed photo-imaging system has been analyzed for the three planets considered in the study assuming (a) linear encoding of data and (b) data compression. The anticipated quality that will be obtained in both monochrome and multispectral planet imagery has been determined using both currently available phototransistor arrays and improved photodetectors with higher sensitivity, which will be available within the near future. Parametric tradeoffs in sensor design versus image quality have been developed using both the phototransistor and the improved detector arrays, and are presented graphically for the viewing conditions at the three planets.

5.4.1
Image Transmission Capability

The geometry of a typical encounter with the planet Jupiter is illustrated in Figure 7. The photo-imaging sequence initiated at a distance of 100 Jupiter radii (154 hours before encounter), allows the entire planet to be viewed until 41 hours prior to encounter, when the planet image will completely fill the 58.5 mrad sensor field-of-view. From this time to the nearest encounter, imagery of selected areas of the planet can be obtained with increasing resolution.

The maximum resolution that can be obtained during the photo-imaging sequence is defined in Table VI in terms of the linear subtense of one line of the scan pattern (one TV line) at the planet's surface. Corresponding data also is presented for the planets Saturn and Uranus.

Actual resolution estimates that will be obtained, including scene radiance and modulation contrast effects, are presented in Sections 5.4.2 and 5.4.3.

During the Jupiter encounter, the number of images that can be obtained without the use of data compression is 2980 (Table VII); and with data compression, this number can be as high as 7491. Without data compression, 605 images can be obtained from Saturn and 84 from Uranus. With data compression, the numbers would be increased to 1515 and 212, respectively.

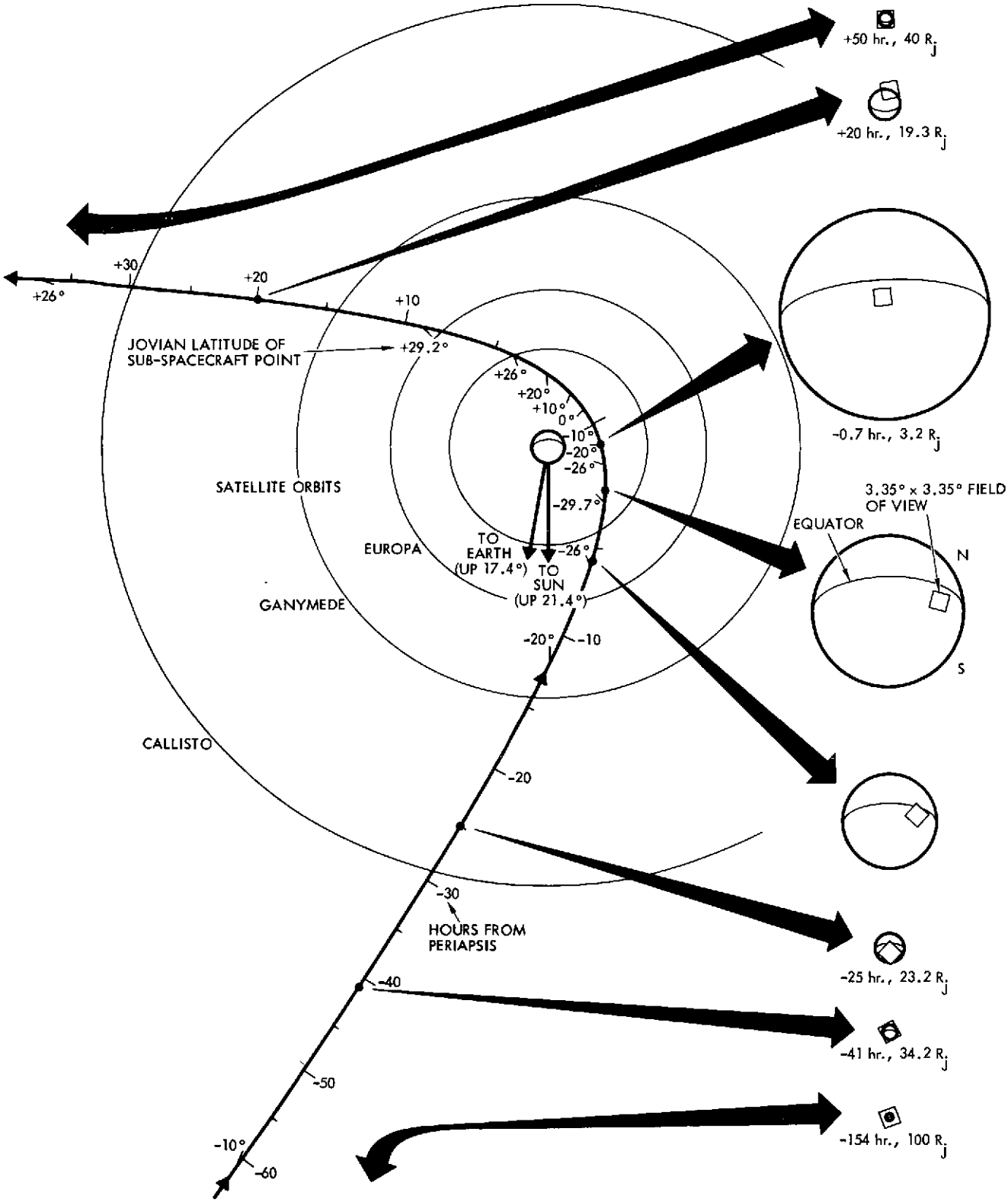

FIGURE 7. – JUPITER PHOTO-IMAGING SEQUENCE

TABLE VI. PHOTO-IMAGING SYSTEM RESOLUTION

Planet	Distance From Planet, Rp	Range, km x 10^6	Image Size On A Side, km x 10^3	Resolution, km/TVL
Jupiter	100	7.14	Entire Planet	1071
	40	2.86	Entire Planet	428
	25	1.79	104.4	268
	10	0.71	41.7	107
	5	0.36	20.9	54
Saturn	100	6.04	Entire Planet	906
	40	2.41	Entire Planet	362
	25	1.51	88.4	227
	10	0.60	35.3	91
	5	0.30	17.7	45
Uranus	100	2.35	Entire Planet	353
	40	0.94	Entire Planet	141
	25	0.59	34.4	88
	10	0.23	13.7	35
	5	0.12	6.9	18

TABLE VII. – IMAGE TRANSMISSION CAPABILITY FOR OUTER PLANET MISSIONS

Planet and Solar Distance, AU	Image Sequence Initiation		Data Rate (12 W, X-Band), b/s	Image Transmission Time, (a)		Number of Images Transmitted (~100 Rp to Nearest Encounter) (b)	
	Time From Encounter, hr	Distance From Planet		Without Data Compression	With Data Compression	Without Data Compression	With Data Compression
Jupiter, 5.2	-154	7.14×10^6 km ($100\ R_J$)	16,384	3^m6^s	1^m14^s	2980	7491
Saturn, 9.5	-125	6.04×10^6 km ($100\ R_S$)	4,096	12^m23^s	4^m57^s	605	1515
Uranus, 19.2	-35	2.35×10^6 km ($100\ R_U$)	1,024	49^m31^s	19^m48^s	42	106

[a] Assumes one-half of data bandwidth used for transmission of imagery.

[b] Number of data bits/frame = 1.521 Mb without data compression.
= 0.608 Mb with data compression.

The photo-imaging system also has multispectral capability, and sequential images can be obtained in any of five spectral bands. Operating in this mode, the total number of images would remain unchanged.

5.4.2 Image Quality

In solid-state spin-scan photo-imaging systems studies performed by TRW Systems (Reference 5), the imagery quality was determined using both the currently available phototransistor arrays and improved photodetector arrays that may be available in the near future.

Image Quality Using Phototransistor Arrays

With the currently available phototransistor arrays, the following spacecraft spin rates are required for high quality monochrome (broad-band) and multispectral imagery.

Planet or Satellite	Spacecraft Spin Rate, rpm	
	Broad-band	Multispectral
Jupiter	5	2
Io	5	2
Europa	5	2
Saturn	2	2
Titan	2	2
Uranus	2	Not feasible

The reduction in spacecraft spin rate from 5 to 2 rpm is required to maintain a satisfactory S/N ratio, compensating for either the reduction in the level of solar irradiance on the more distant planets, or the reduction in exposure on the phototransistor arrays when operating in a multispectral (narrow-band) mode. Image quality can be defined by determination of the S/N ratio as a function of spatial frequency, when observing a scene of specified radiance and modulation contrast.

These data presented in Figure 8 are for the planet Jupiter. The S/N ratios are computed for five values of scene modulation contrast, from 5 to 100%. These are plotted as a function of spatial frequency at the image plane of the sensor, with the spatial frequency of 32.8 lpm corresponding to the instantaneous field-of-view of one detector element, or the one-scan-line width in the 390 TV line raster. This spatial frequency also corresponds to the electronic sampling or Nyquist frequency.

A S/N ratio of 6/1 is generally considered as a criterion of satisfactory image quality. Figure 8 shows that excellent image quality will be obtained for all levels of scene modulation contrast, with the exception of the lowest modulation level at the resolution limit of the sensor.

Corresponding data are presented in Figure 9 for Uranus, at a distance from the sun of 19.2 AU. Because of the lower solar irradiance level, 50% modulation contrast of the scene will be required to obtain a satisfactory S/N ratio at the resolution limit of the sensor.

Appendix B contains additional data on broad-band system performance for all planets and satellites considered.

Figure 10 illustrates the performance that can be obtained when operating in the multispectral mode during the planet Jupiter observation. Again, high image quality will be obtained in all five spectral bands, with performance being marginal only in the infrared band (0.8 to 1.1 μm) at the resolution limit.

When Saturn is observed (Figure 11), satisfactory imagery can be obtained in the multispectral mode up to approximately one-half of the resolution limit (corresponding to an IFOV of 0.30 mrad) in the four spectral bands covering the range from 0.4 to 0.8 μm. Satisfactory imagery will not be obtained in the infrared band because of the lower albedo of the planet in this range.

Image Quality Using Improved Photodetectors

Continuing effort in the development of silicon photodetector arrays will result in improved performance of spin-scan photo-imaging systems. Potential improvements are primarily a reduction in the noise-equivalent-signal (NES), or dark noise, and improved quantum efficiency, particularly in the infrared

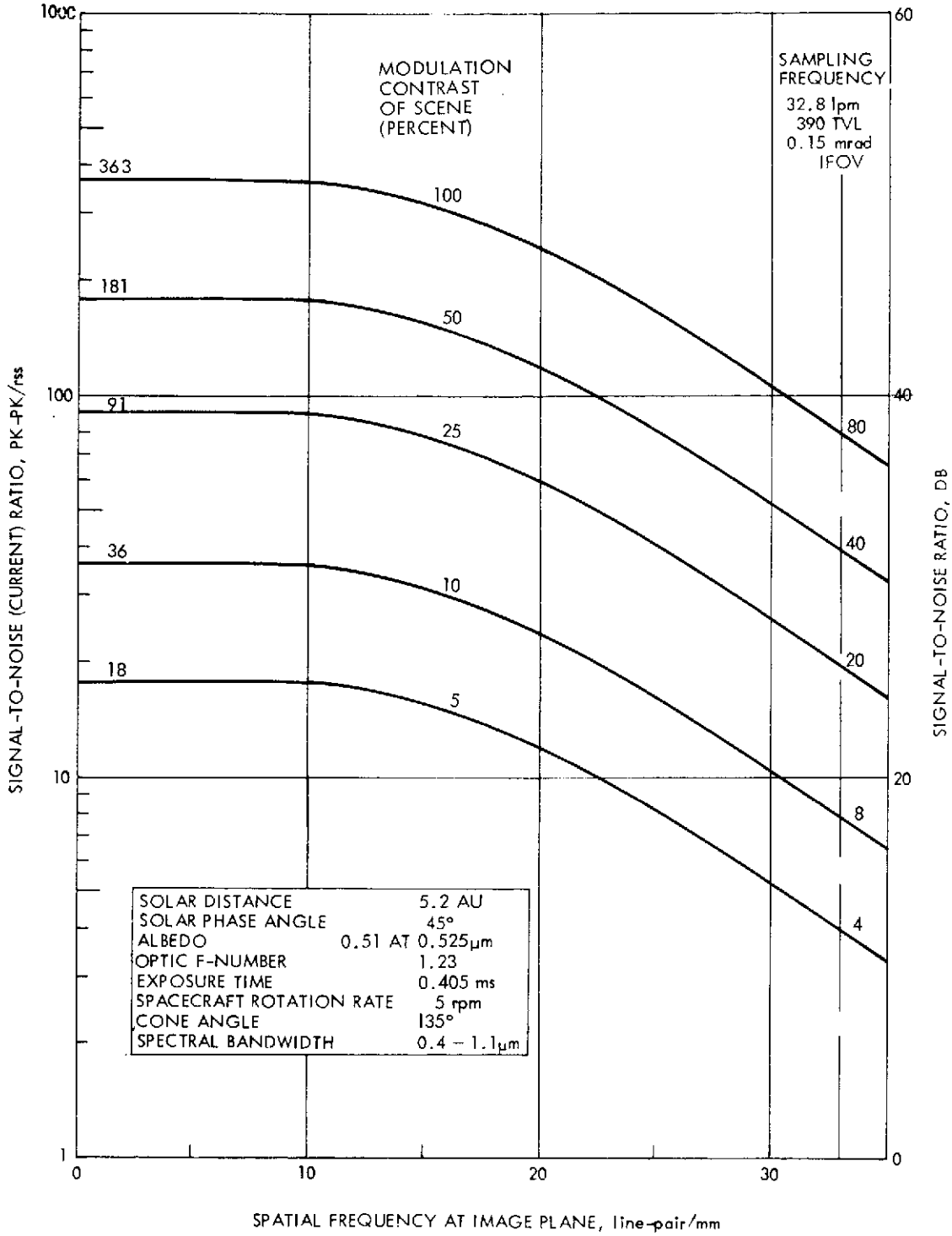

FIGURE 8. – PHOTO-IMAGING SYSTEM PERFORMANCE OBSERVING JUPITER (BROAD-BAND MODE)

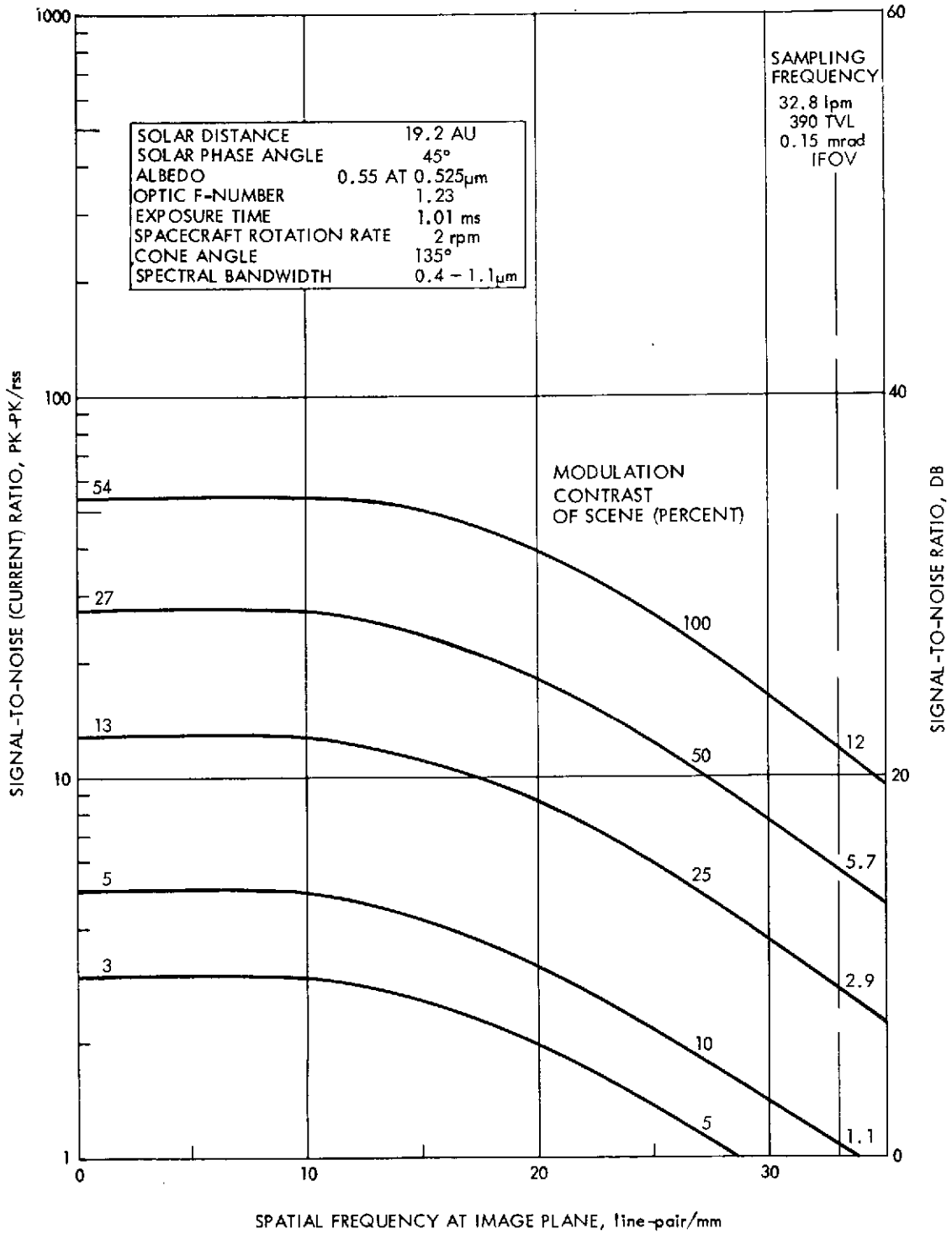

FIGURE 9. – PHOTO-IMAGING SYSTEM PERFORMANCE OBSERVING URANUS (BROAD-BAND MODE)

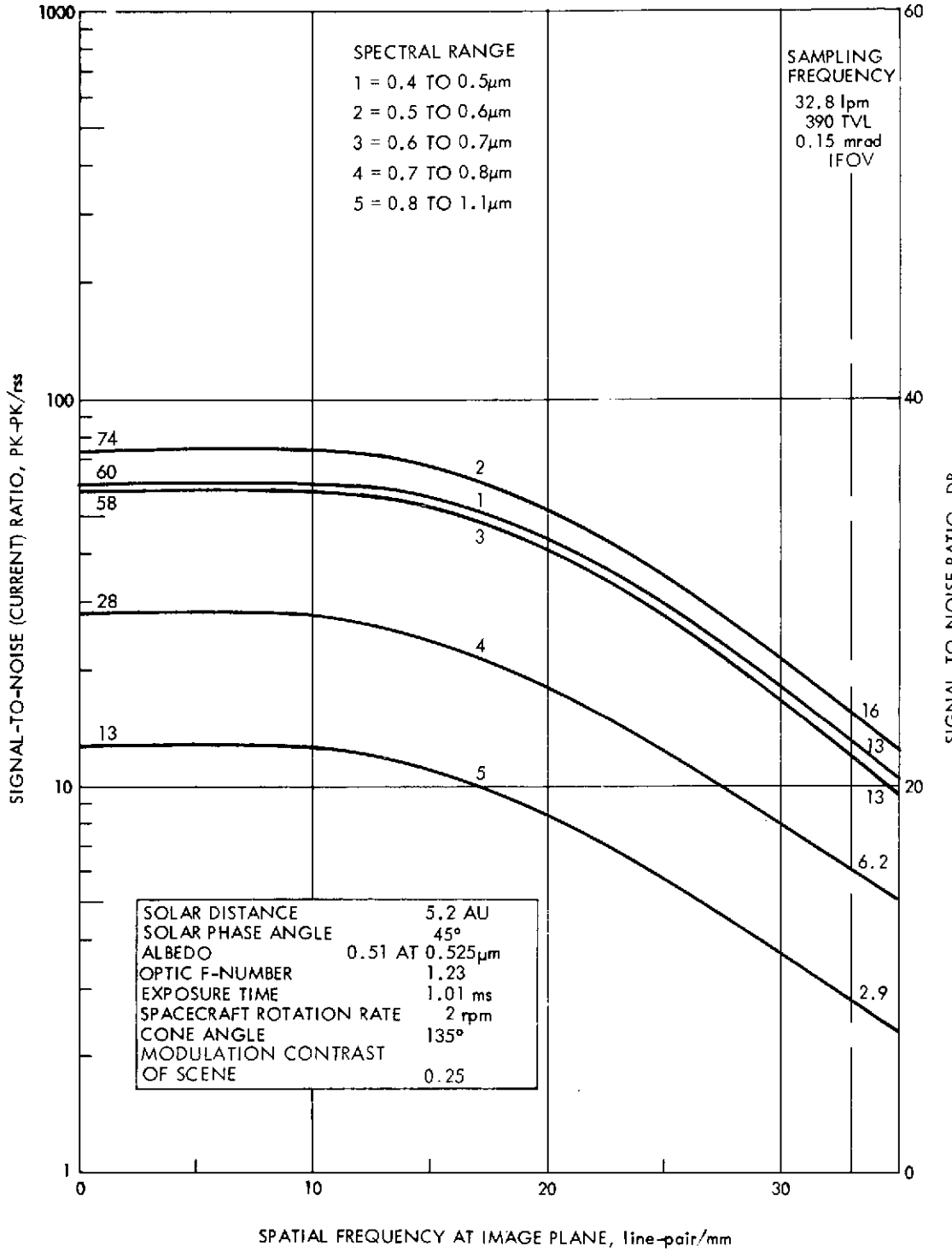

FIGURE 10. – PHOTO-IMAGING SYSTEM PERFORMANCE OBSERVING JUPITER (MULTISPECTRAL MODE)

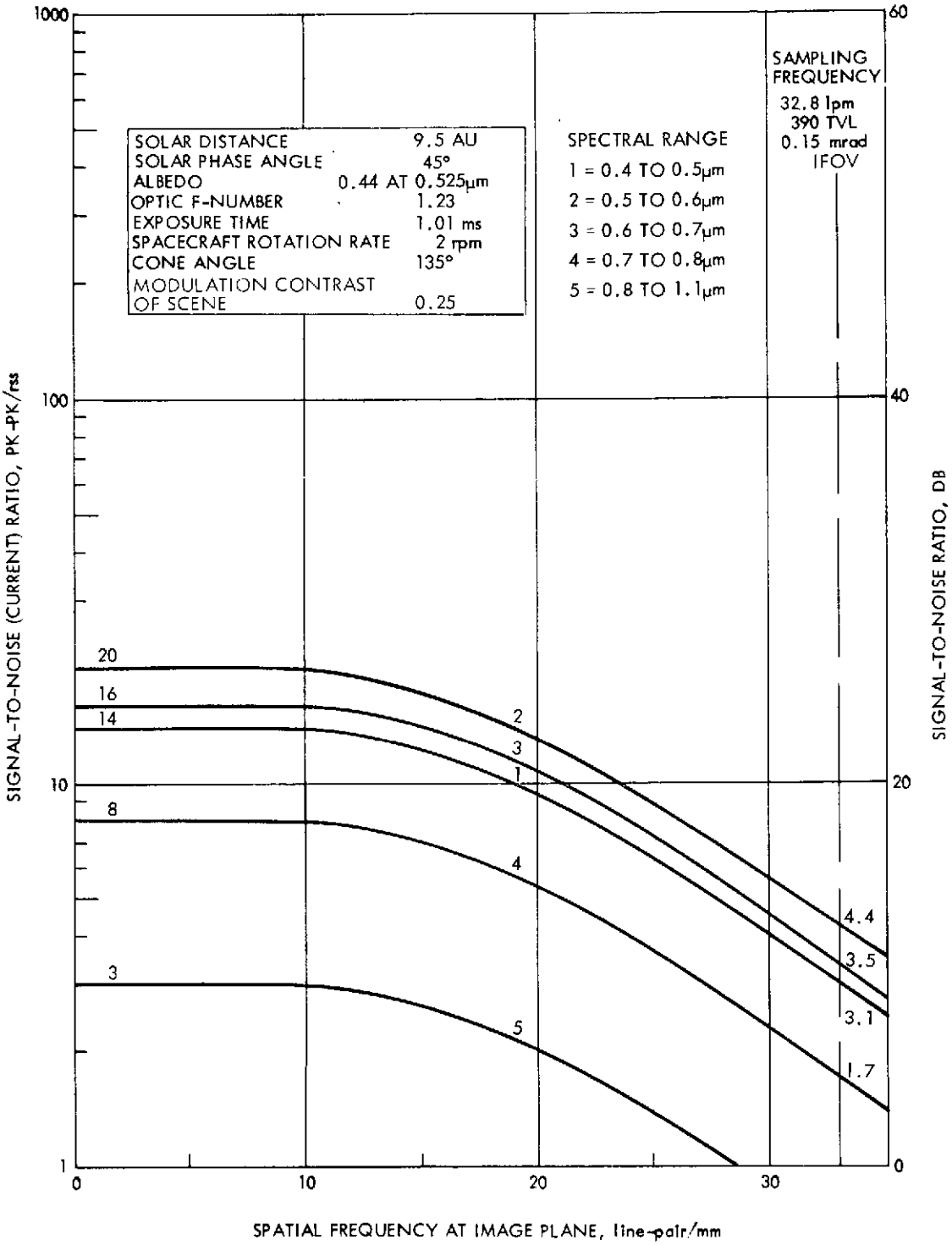

FIGURE 11. – PHOTO-IMAGING SYSTEM PERFORMANCE OBSERVING SATURN (MULTISPECTRAL MODE)

range of the spectrum. The NES can be improved by reducing dark current leakage, capacitance sampling noise, feedback capacitance noise, and preamplifier thermal and shot noise. Laboratory tests of development samples of improved photodetectors exhibit potential improvements in the NES by a factor of approximately six, reducing the value of the NES to the order of 0.2 $\mu J/m^2$, equivalent to a noise level of less than 200 photoelectrons, rms.

The spacecraft spin rates which will be required to obtain satisfactory imagery with the improved arrays will be as follows,

Planet or Satellite	Spacecraft Spin Rate, rpm	
	Broad-band	Multispectral
Jupiter	5	5
Io	5	5
Europa	5	5
Saturn	2	2
Titan	2	2
Uranus	2	2

Computations to determine the imagery quality show a marked improvement over those obtained with the current arrays. First, considering broad-band operation (Figure 12) when observing Jupiter, the S/N ratios are more than doubled with a S/N ratio of 11 being obtained at the resolution limit when observing a scene with only 5% modulation contrast.

At Uranus, the S/N ratios are increased by a factor of approximately four, with a scene modulation contrast of only 12% producing a S/N ratio of 6/1 (Figure 13).

When used in the multispectral mode, satisfactory imagery of Jupiter (Figure 14) can be obtained using a 5 rpm spacecraft spin rate, and performance in the infrared band (0.8 to 1.1 μm) is now satisfactory where it was previously marginal.

Multispectral imagery at Uranus (Figure 15), previously not possible, is now feasible; however, because of the extremely low level of illumination at this planet and the low value of albedo in the infrared range, performance in the infrared range (bands 4 and 5) will be marginal.

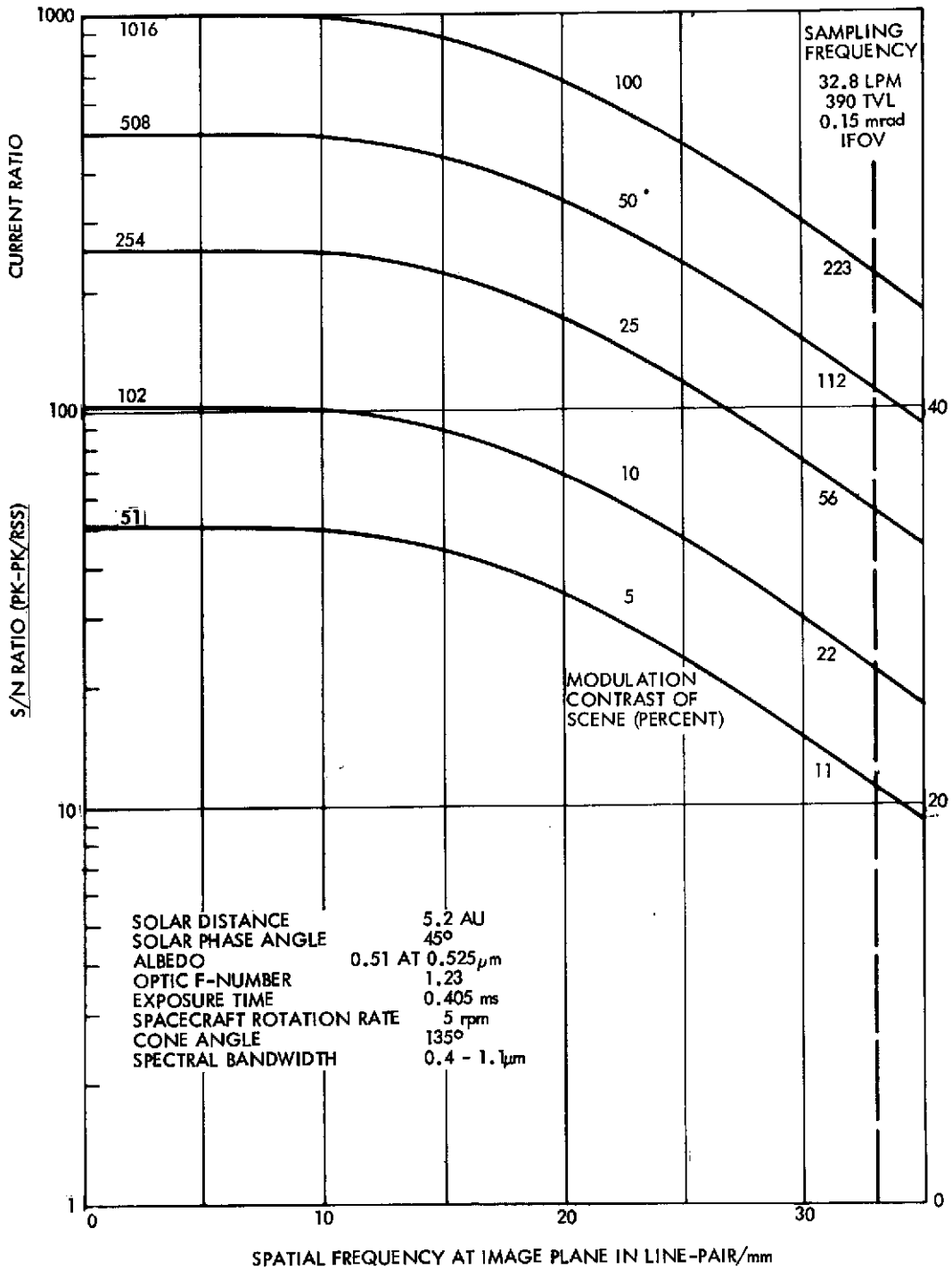

FIGURE 12. – PHOTO-IMAGING SYSTEM PERFORMANCE OBSERVING JUPITER WITH IMPROVED PHOTODETECTORS (BROAD-BAND MODE)

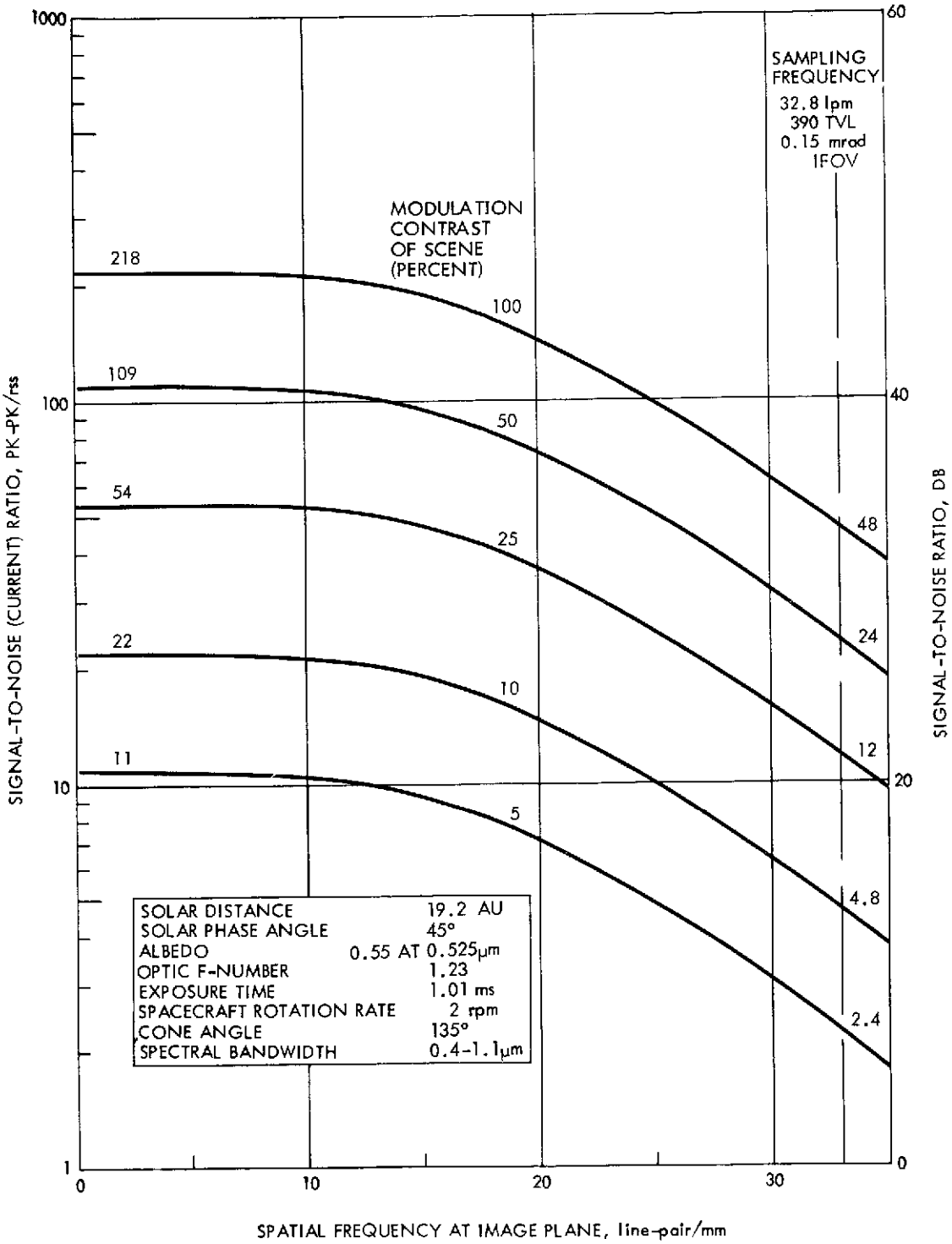

FIGURE 13. – PHOTO-IMAGING SYSTEM PERFORMANCE OBSERVING URANUS WITH IMPROVED PHOTODETECTORS (BROAD-BAND MODE)

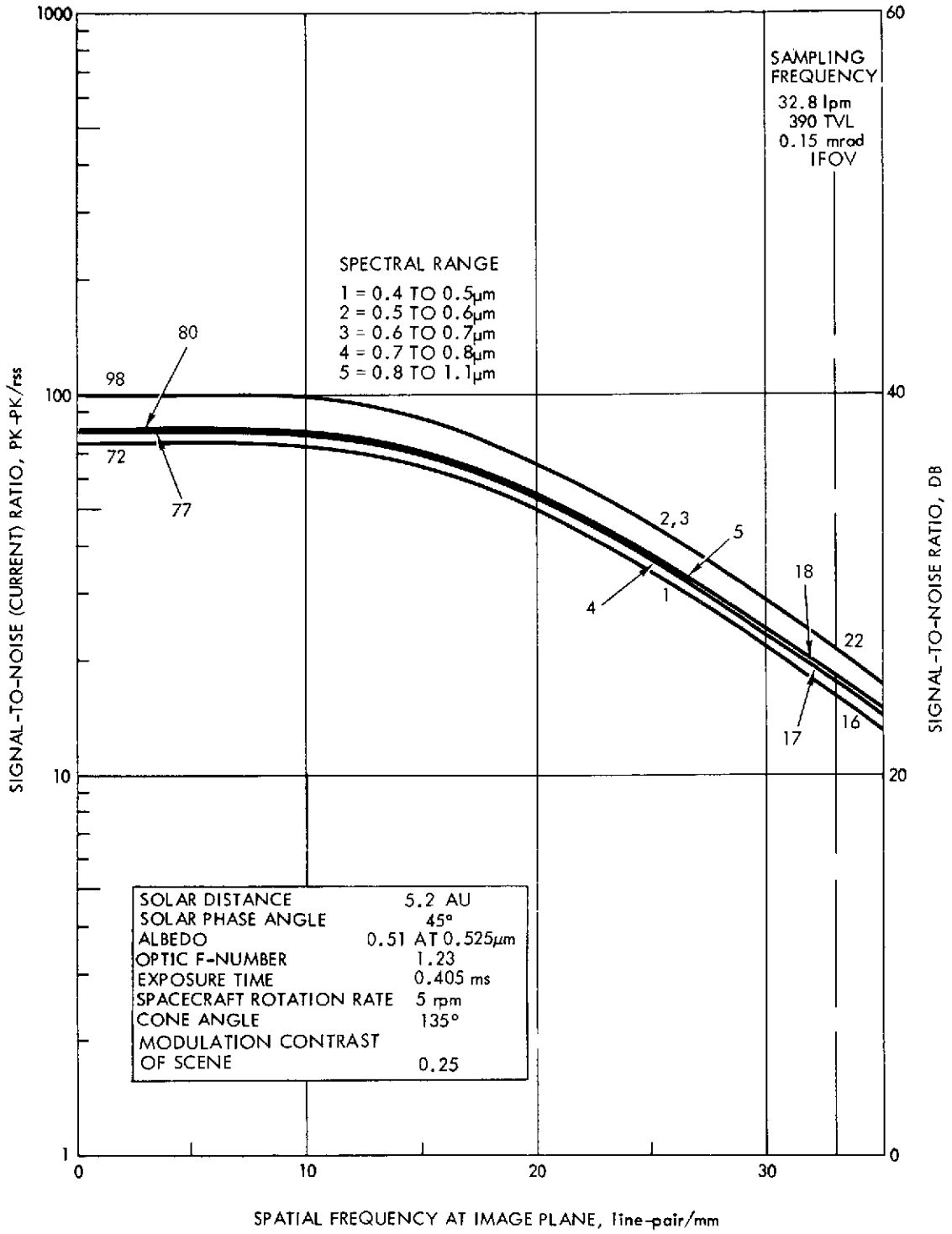

FIGURE 14. – PHOTO-IMAGING SYSTEM PERFORMANCE OBSERVING JUPITER WITH IMPROVED PHOTODETECTORS (MULTISPECTRAL MODE)

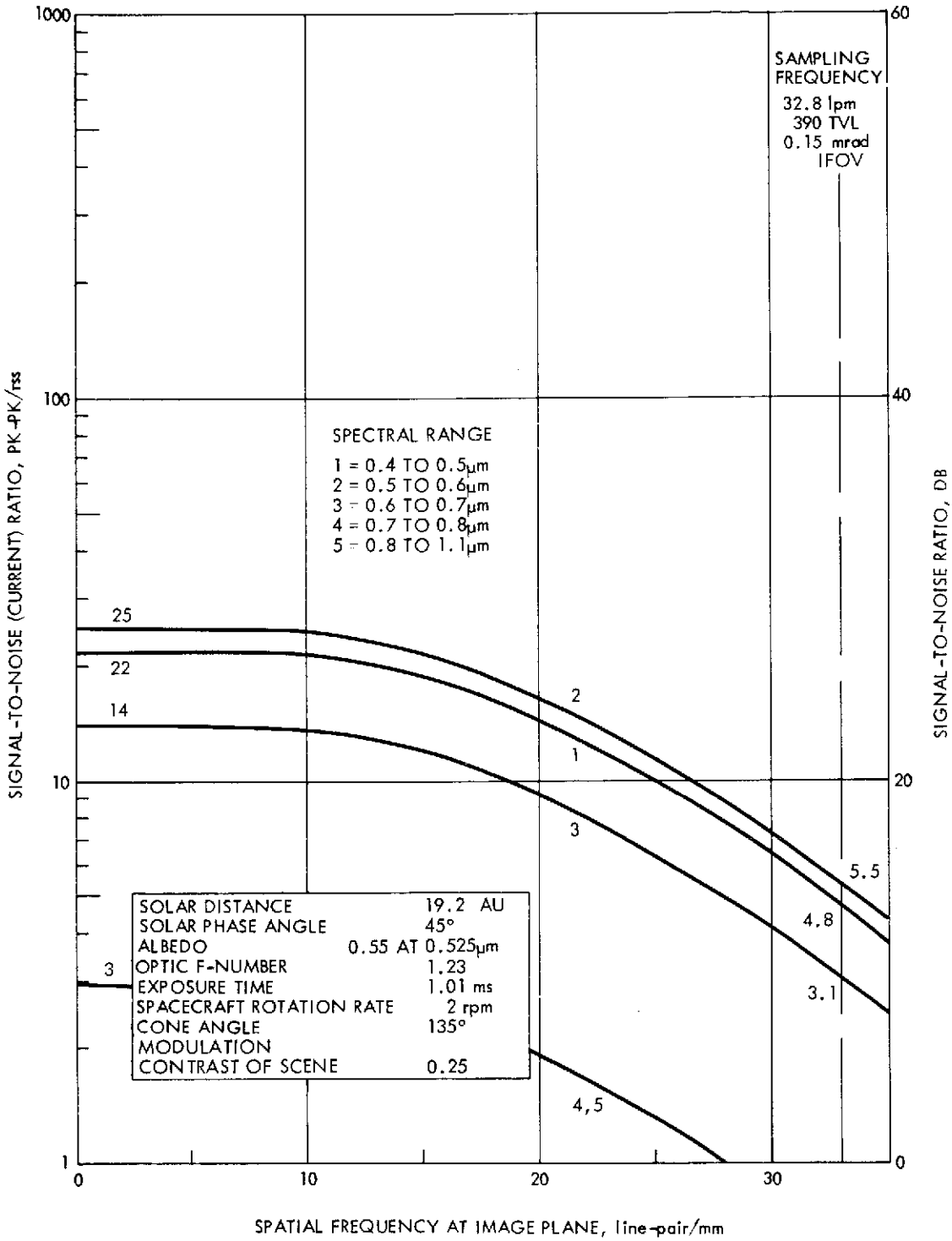

FIGURE 15. – PHOTO-IMAGING SYSTEM PERFORMANCE OBSERVING URANUS WITH IMPROVED PHOTODETECTORS (MULTISPECTRAL MODE)

5.4.3
Parametric Tradeoffs

For use by the scientific experimenter, parametric models defining the tradeoffs between the planet (or satellite) and spacecraft characteristics, photo-imaging system design, parameters, and image quality (S/N and spatial resolution) have been developed for photo-imaging systems using currently available phototransistor arrays and improved photodetector arrays.

From these models, tradeoffs between the following parameters can be determined:

a. Instantaneous field-of-view (IFOV)

b. Linear resolution at the planet or satellite surface

c. Spacecraft spin rate

d. Planet phase factor

e. Photo-imaging system lens diameter

f. Scene modulation contrast

g. Spectral bandwidth of the photo-imaging system (broad-band or multispectral operation mode)

h. S/N ratio at zero spatial frequency (S/N ratio when observing very broad features on planetary surface

i. S/N ratio at the sampling, or Nyquist, frequency (corresponding to one scan-line width or at an IFOV of 0.15 mrad).

Models using phototransistor arrays, are illustrated in Figures 16, 17, and 18 for the planets Jupiter, Saturn, and Uranus. Improved photodetector models are shown in Figures 19, 20, and 21.

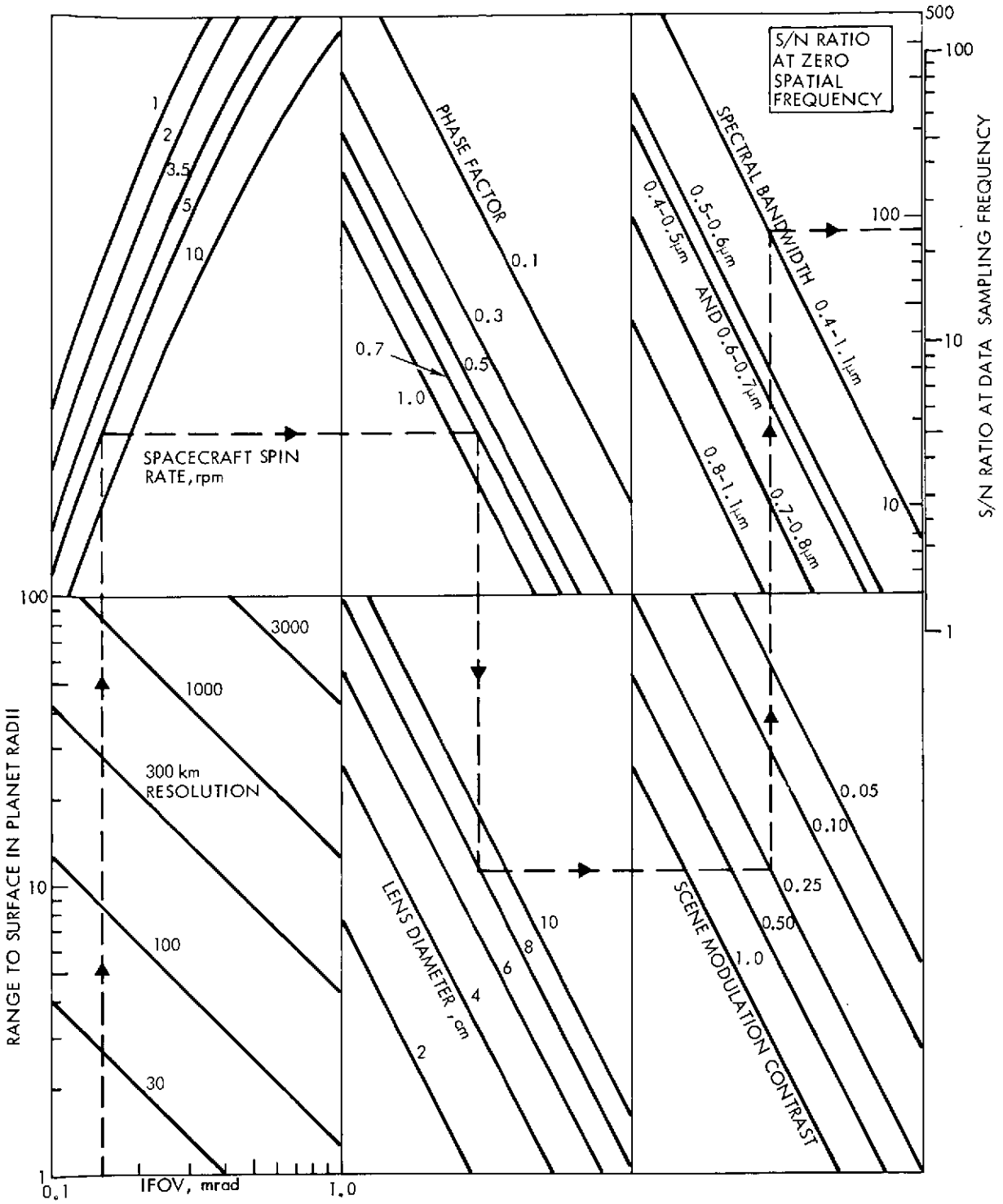

FIGURE 16. – PARAMETRIC MODEL, PHOTO-IMAGING SYSTEM PERFORMANCE OBSERVING JUPITER WITH PRESENT PHOTOTRANSISTORS

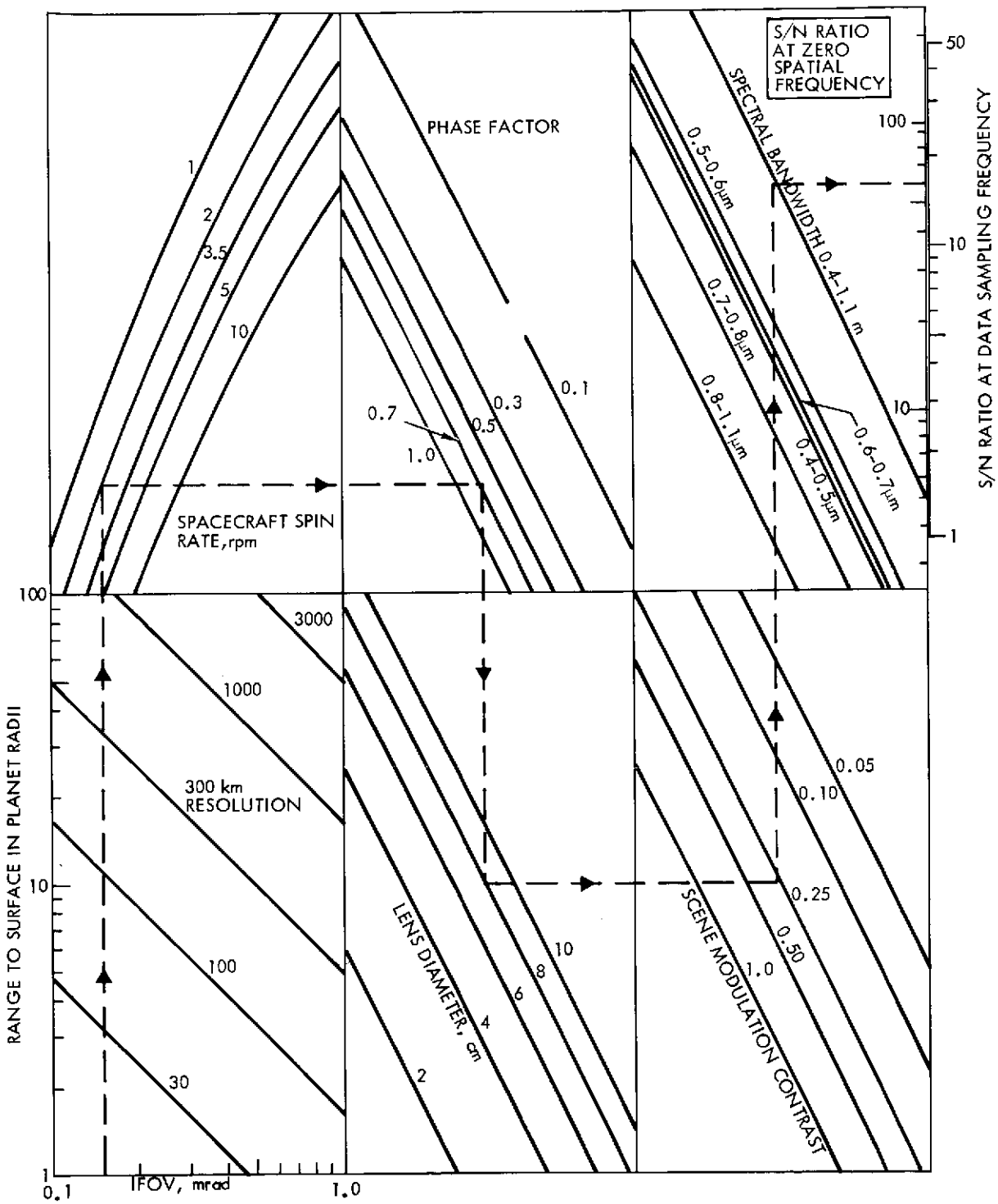

FIGURE 17. – PARAMETRIC MODEL, PHOTO-IMAGING SYSTEM PERFORMANCE OBSERVING SATURN WITH PRESENT PHOTOTRANSISTORS

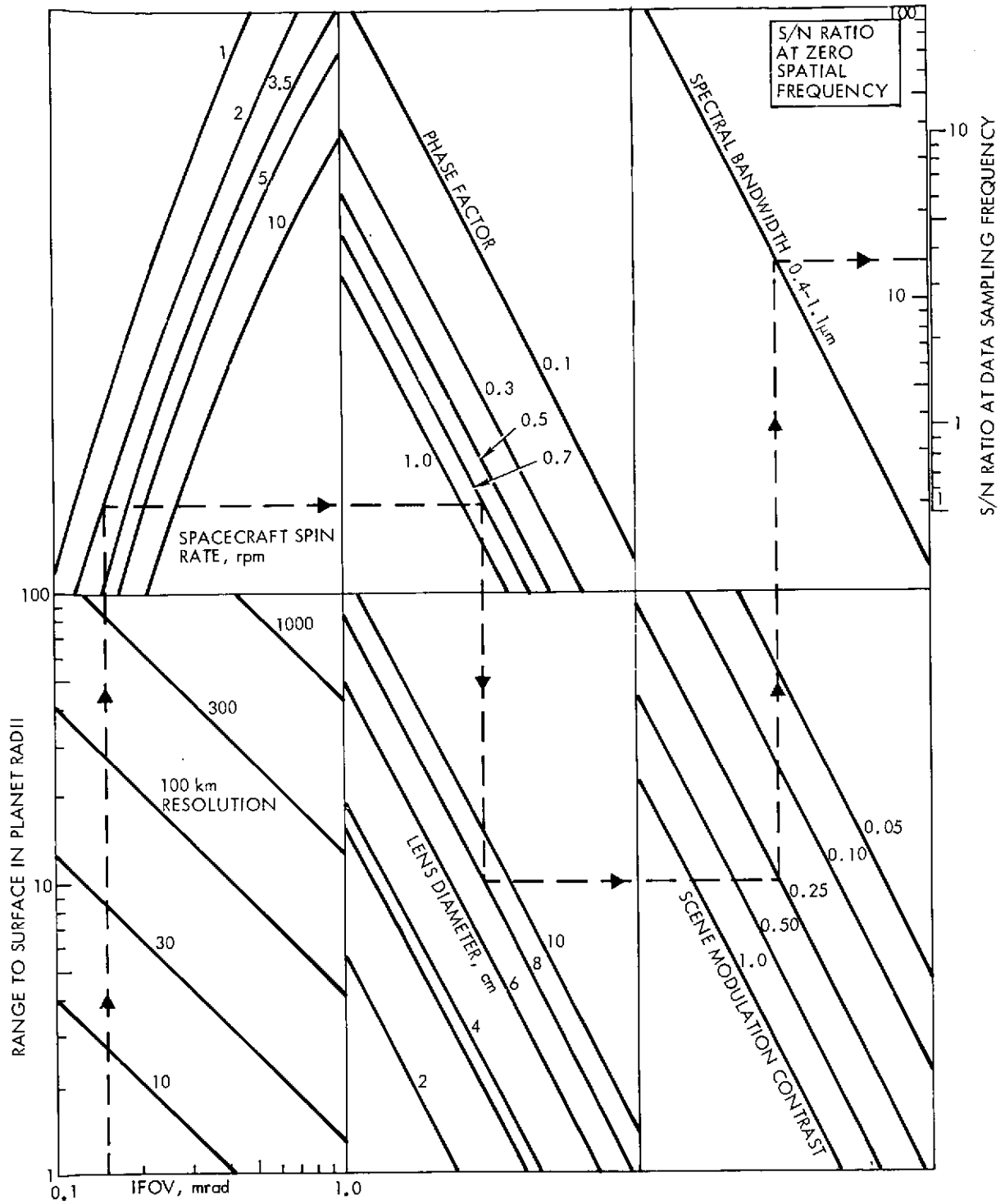

FIGURE 18. – PARAMETRIC MODEL, PHOTO-IMAGING SYSTEM PERFORMANCE OBSERVING URANUS WITH PRESENT PHOTOTRANSISTORS

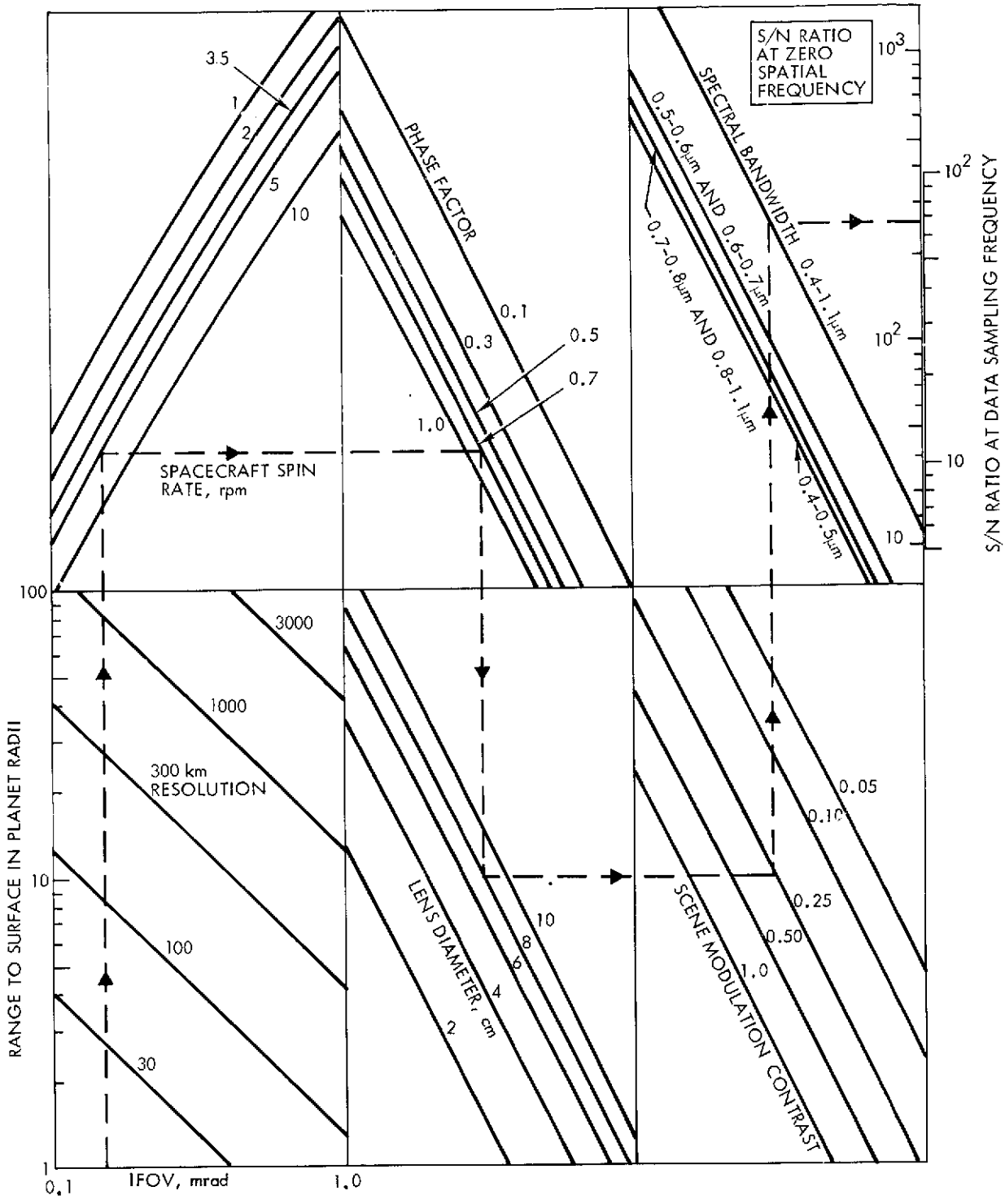

FIGURE 19. – PARAMETRIC MODEL. PHOTO-IMAGING SYSTEM PERFORMANCE OBSERVING JUPITER WITH IMPROVED PHOTODETECTORS

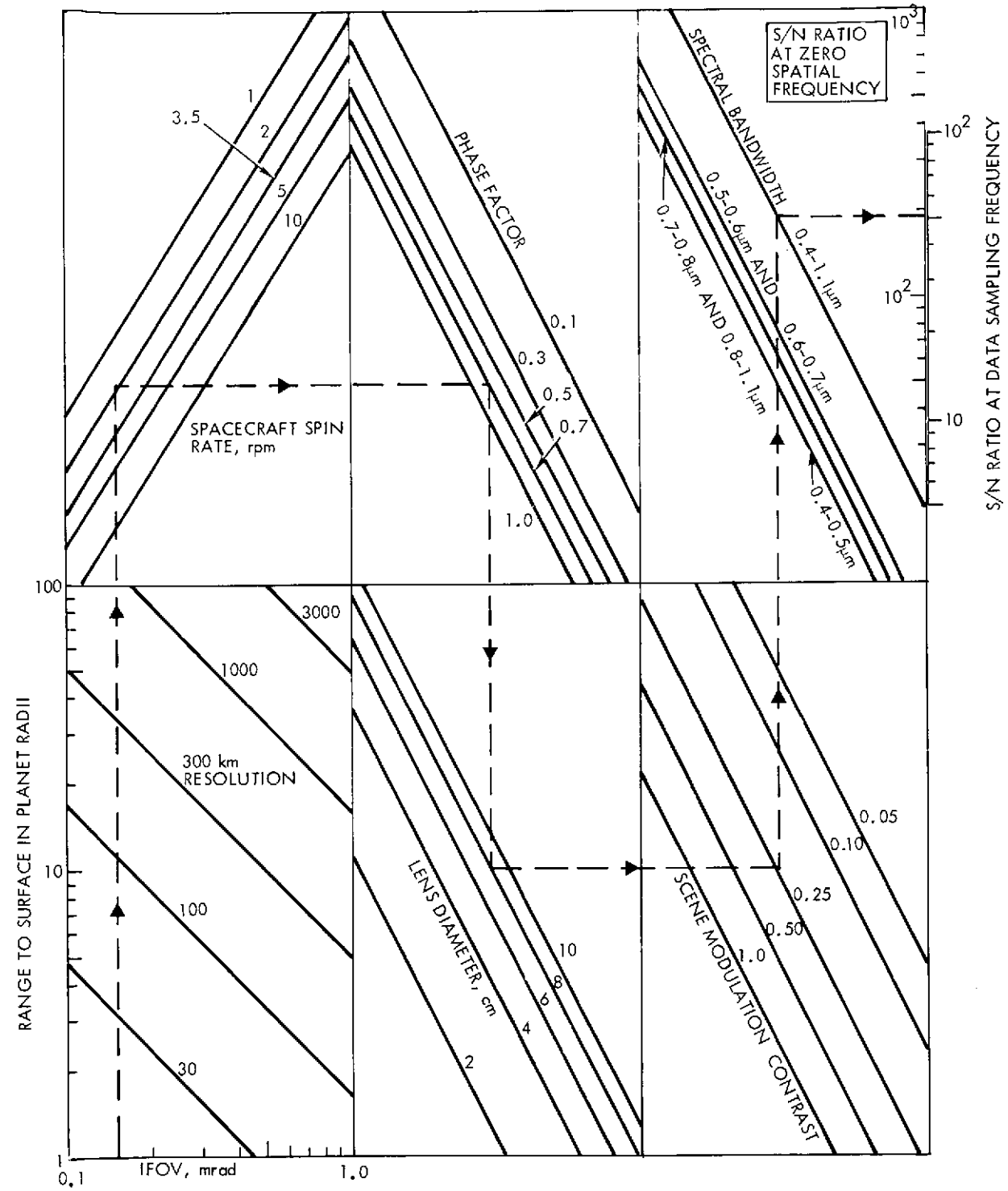

FIGURE 20. – PARAMETRIC MODEL, PHOTO-IMAGING SYSTEM PERFORMANCE OBSERVING SATURN WITH IMPROVED PHOTODETECTORS

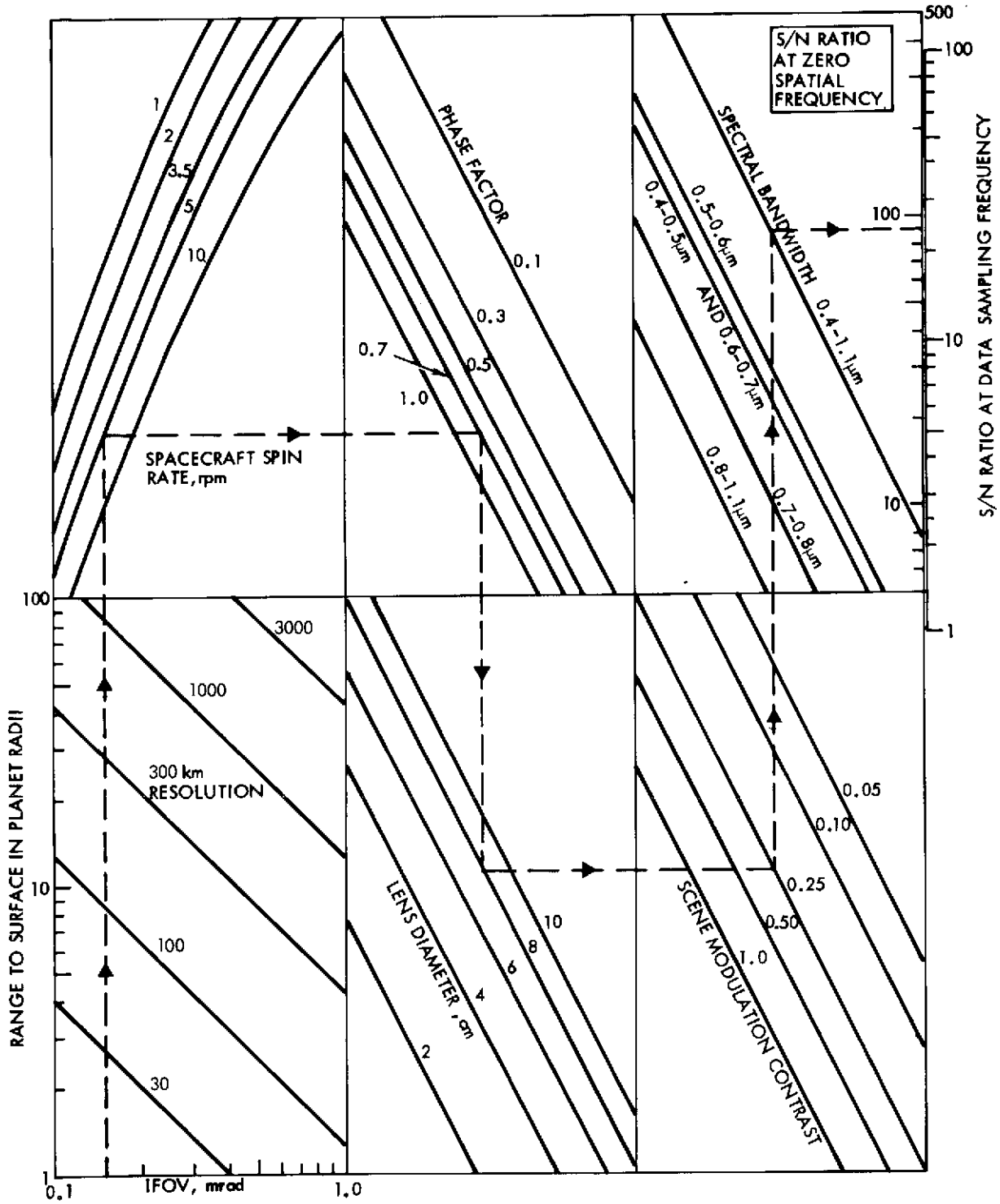

FIGURE 21. – PARAMETRIC MODEL, PHOTO-IMAGING SYSTEM PERFORMANCE OBSERVING URANUS WITH IMPROVED PHOTODETECTORS

6.0
CHARACTERISTICS OF PHOTOTRANSISTOR ARRAYS

The basic element of the photodetector array consists of a large scale array (LSA) chip containing 195 phototransistors and preamplifiers and a second signal conditioning electronics (SCE) chip containing five amplifier channels mounted on a common LSA substructure assembly (Figure 22). The five signals from the SCE require additional signal conditioning, multiplexing, and digital data processing.

6.1
LSA Configuration

The LSA phototransistors, fabricated by triple-diffusion in silicon on a single chip (Figure 23), are arranged in two rows: one of 97 elements and the other of 98 elements. If a single row of closely-spaced elements were used, excessive cross-talk would result from penetration of the incident radiation into the base material. The staggered configuration provides sufficient spacing between adjacent elements to reduce the amount of cross-talk between adjacent detector elements to a value of less than two percent.

The size of the photosensitive area of each phototransistor is 18μm x 23μm (0.7×10^{-3} x 0.9×10^{-3} in.), and the pitch spacing along the array is 15.2μm (0.6×10^{-3} in.). The two rows of phototransistors are separated by a distance of 30.4μm (1.2×10^{-3} in.). The overall length of the total array of 195 phototransistors is 2.97 mm (0.117 in.). To form an extended array, adjacent chips can be aligned within a tolerance of 2.5μm (0.1×10^{-3} in.) along or normal to the array, and the vertical (z-axis) positioning of the chips can be held to the same tolerance. Extended arrays can be made to conform either to a flat or to a curved surface.

The LSA chip consists not only of the phototransistor elements, but also 195 stages of amplification (one for each element) as well as a shift register and a multiplexer. The multiplexer is used to commutate the outputs of the 195 preamplifiers onto five signal leads, each containing the serial output of 39 preamplifiers. These five signal leads are hard-wired to the second chip containing the five SCE amplifiers which further amplify the five serial signals

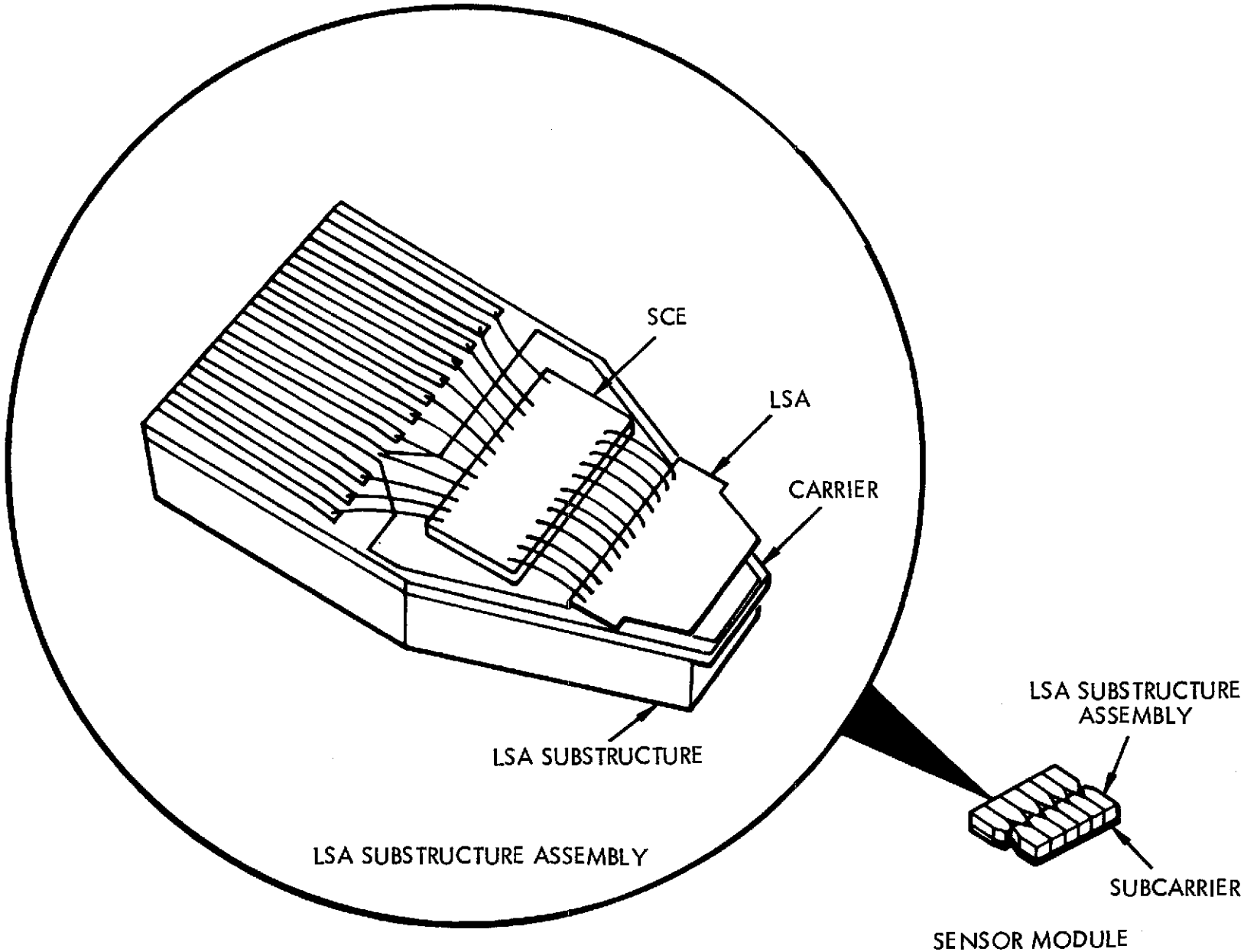

FIGURE 22. – DETECTOR ARRAY STRUCTURAL CONFIGURATION

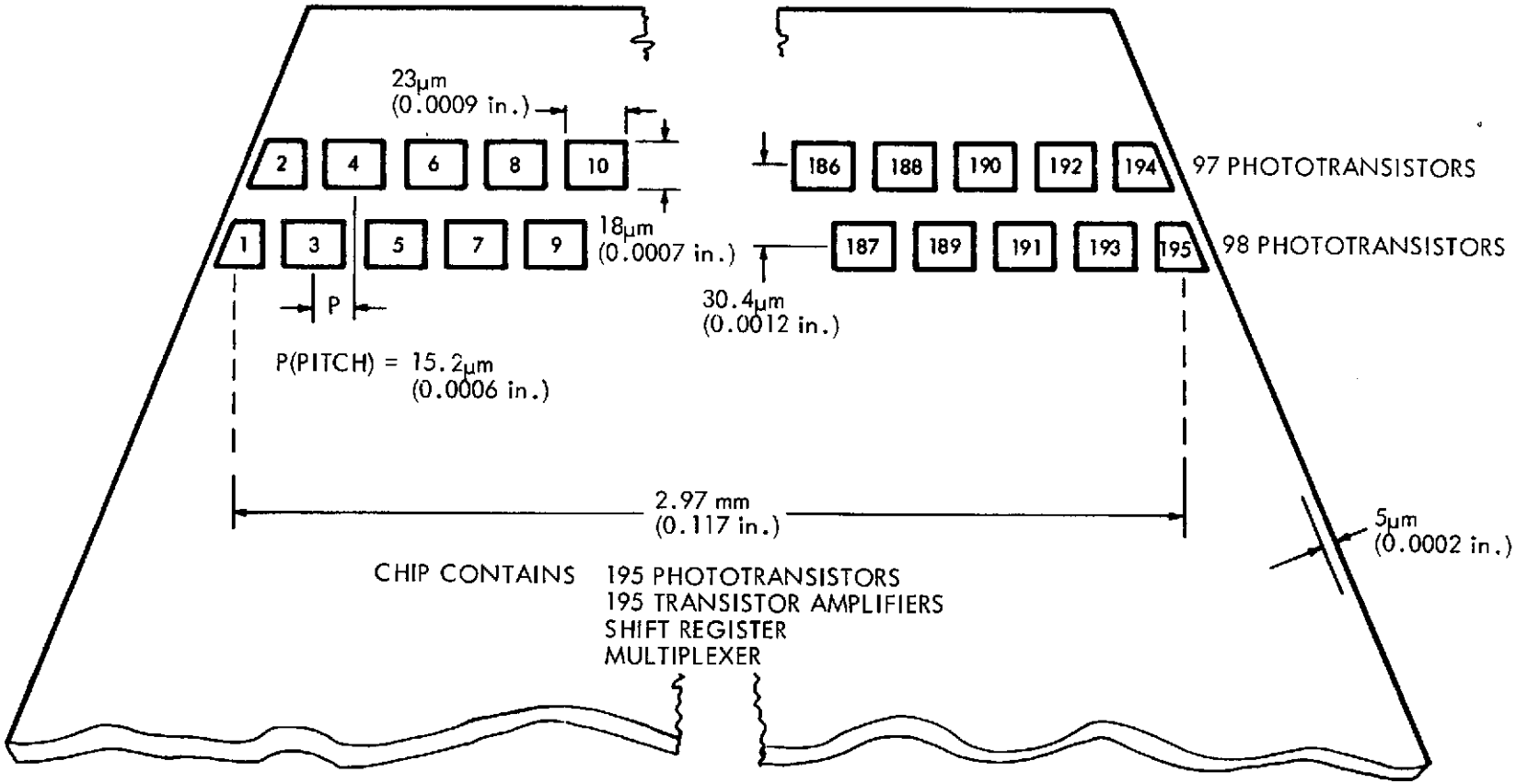

FIGURE 23. – LSA CHIP GEOMETRY

prior to digital processing of the signals. The digital processing electronics, external to the LSA and SCE chip, are fabricated of integrated circuits and discrete components.

6.2
Equivalent Circuit

The equivalent circuit of the LSA consists of a phototransistor and an amplifier transistor arranged in a Darlington configuration (Figure 24). Initially, the charge on the base-collector capacitance of the phototransistor is neutralized by a pumping transistor (denoted by ERASE switch). Bias is then applied to the base-collector capacitance by the S3 switch. During the light exposure interval, radiation incident on this junction generates electron-hole pairs which results in discharge of the bias applied to the junction, the amount of discharge being proportional to the amount of energy absorbed during the exposure interval. This change in the current output of the phototransistor during the exposure interval is increased by the gain of the amplifier transistor (preamplifier). Multiplexing of the 195 signals from the phototransistors is accomplished as follows. The collectors of the 195 amplifier transistors (preamplifiers) are connected together in five groups of 39 (195 total). Readout is accomplished by the closing of the readout switches (S3), in sequence, under the control of a shift register. The switching of 39 switch transistors in sequence results in a serial output from 39 preamplifiers. With five groups of 39 being interrogated in parallel, readout of the signal from the 195 phototransistors is accomplished. The readout, or sampling, of the output of each preamplifier is accomplished in 2μs, with 78μs being required for serial sampling of a group of 39. After this sampling, the photojunctions of the phototransistors are again biased and the cycle is repeated.

On the SCE chip, five amplifiers are used to increase the level of the five signals from the LSA chip prior to the conversion of the video signal from analog to digital. Each of the amplifiers has two stages of gain. The clamp switch, S1, is used to reset the signal to a reference level between each of the 39 serial samples from the LSA sensor. The POWER ON switch is used to apply power to the SCE amplifier to initiate operation.

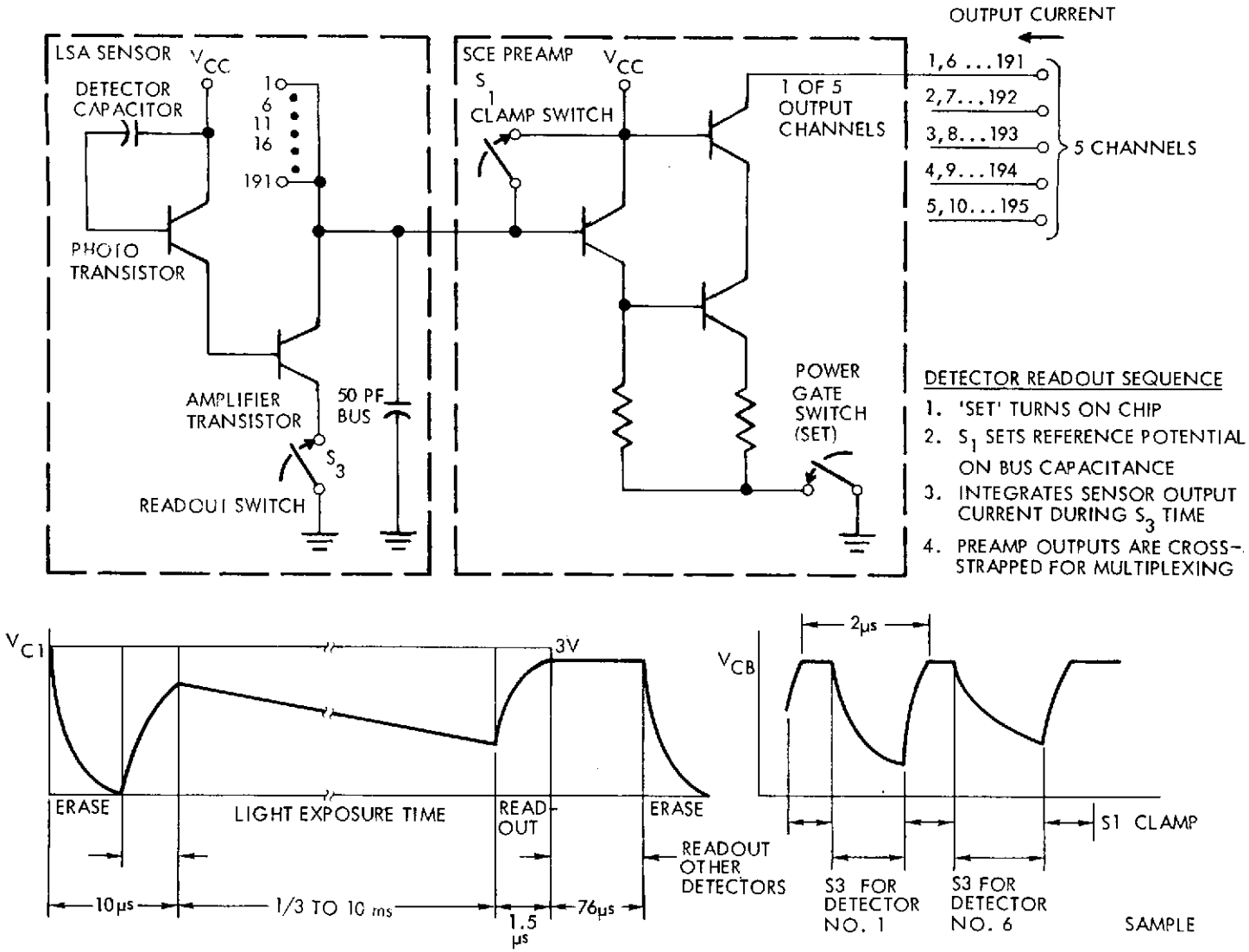

FIGURE 24. – LSA/SCE CIRCUIT DIAGRAM

6.3
Performance Characteristics

The quantum efficiency of the phototransistors is illustrated in Figure 25 for two values of base-collector diffusion depth. A diffusion depth of 5.2μm is currently used. If increased sensitivity in the near-infrared range is desired, the deeper diffusion depth of 13.5μm can be used. The inflections in the curves are caused by the interference of light in the silicon dioxide passivation layer on the photodetectors.

The variation in responsivity of the current from the LSA–SCE combination is illustrated in Figure 26. The gamma is near unity, with a dynamic range of $10^3/1$. Three-sigma variation in output at maximum integrated exposure level is 2/1, and the dark noise level, expressed as noise equivalent signal (NES), is 1.2×10^{-3} W/m^2. An integration time of 10^{-3} second is used that corresponds to an integrated energy density of 1.2μJ/m^2.

The spatial frequency response of the arrays, defined by the modulation transfer functions both parallel and normal to the array, is approximately 30% at the limiting resolution of 32.8 line-pair/mm (Figure 27). The shapes of the modulation transfer functions are determined not only by the geometrical size of the photosensitive area of the phototransistors, but also by the sensitivity contour of the photosensitive area. These contours are measured by a laser beam probe with an effective beam diameter of approximately 1μm.

The performance characteristics of the phototransistor arrays are summarized in Table VIII. The results of tests performed to determine susceptibility to environmental radiation are presented in Table IX.

In Table X, the characteristics of the phototransistor arrays are compared with those of the silicon intensifier vidicon and silicon diode array vidicon. The phototransistors offer the following advantages over the television camera tubes: (a) high geometric accuracy, resulting in simplicity of image reconstruction, (b) image reconstruction without fiducial marks for geometric reference, (c) highlight areas free from blooming of electron charge, (d) highlight charge free from electron beam bending, (e) lifetime unlimited by thermionic filament use, (f) linear variation of signal current with exposure to illumination, and (g) high radiometric accuracy. Note that the limiting resolution of the phototransistor array is specified as 390 TV lines. This value applies to

an array consisting of two chips of 195 detector elements. If more chips are used in an array, the limiting resolution will be correspondingly higher. With respect to responsivity (current vs detector irradiance), the phototransistor arrays and silicon diode array vidicon are comparable.

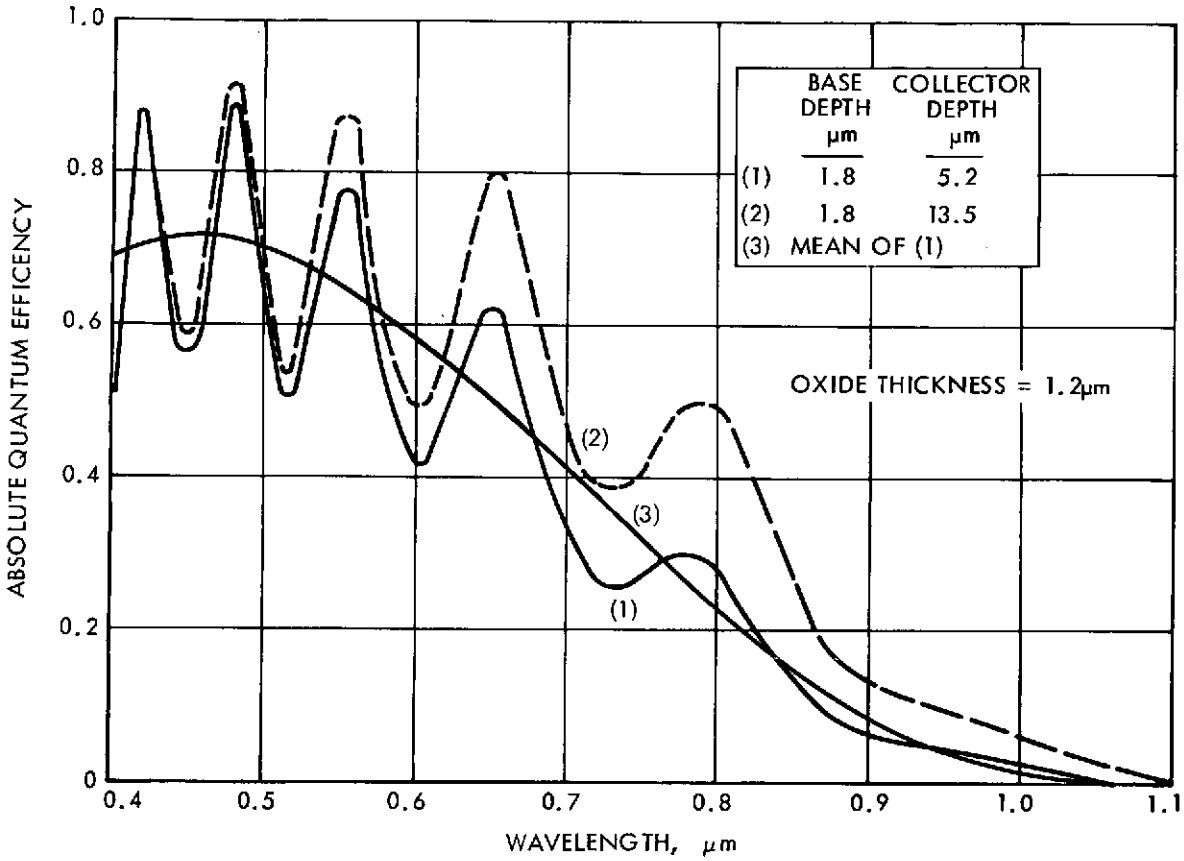

FIGURE 25. – ABSOLUTE QUANTUM EFFICIENCY OF DETECTOR ARRAY (THEORETICAL)

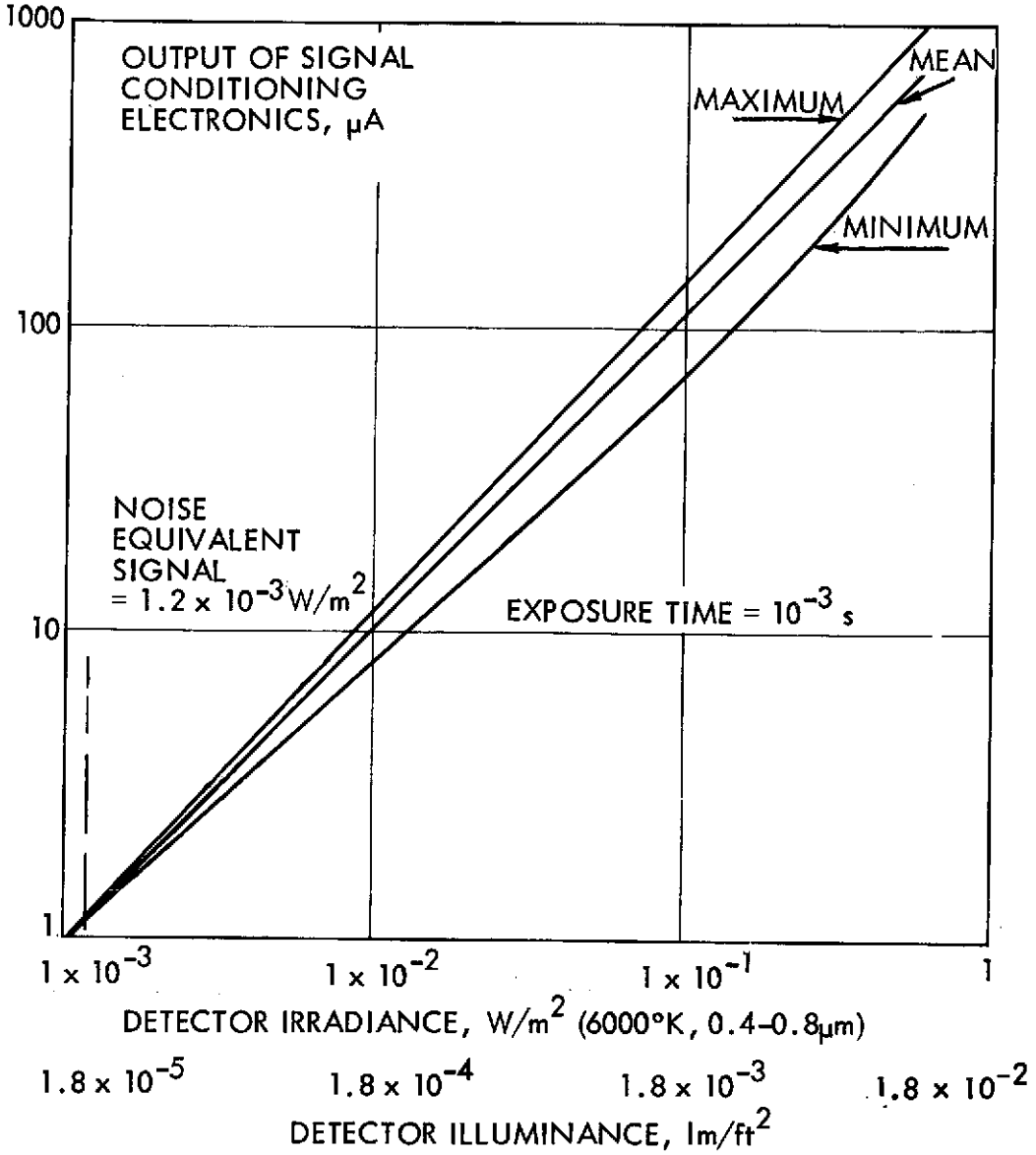

FIGURE 26. — VARIATION IN RESPONSIVITY OF 195 DETECTOR ELEMENTS ON A SINGLE LSA

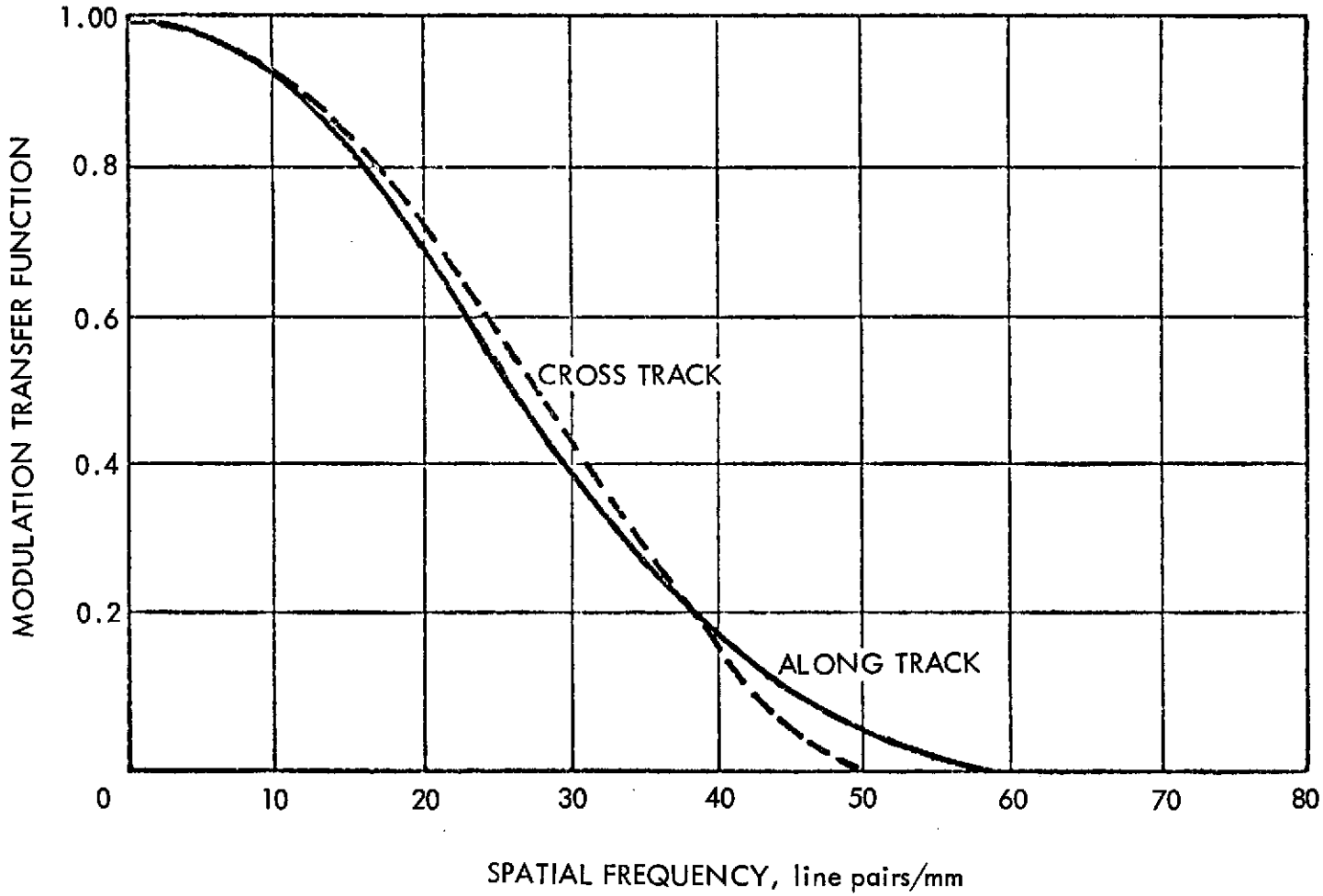

FIGURE 27. — PHOTOTRANSISTOR MODULATION TRANSFER FUNCTION

TABLE VIII. – PHOTOTRANSISTOR ARRAY PERFORMANCE CHARACTERISTICS

Parameter	Value
System dark noise (Noise Equivalent Signal)	[a] NES $\leq 1.2 \times 10^{-6}$ J/m^2
Maximum light intensity	[a] 1.2 W/m^2
Detector element size	18 x 23μm (0.7 x 0.9 mil)
MTF (33 line-pair/mm)	0.27 along array 0.25 parallel to array
Alignment accuracy	±2.5μm (±0.1 mil) chip-to-chip (X, Y axes) ±2.5μm (±0.1 mil) (Z axis)
Dynamic range	1000/1 (normal operating range)
Integration time	0.3 to 10 ms

[a] With irradiance of 6000°K radiation temperature over spectral range from 0.4 to 0.8μm with nominal integration time of 1 ms.

TABLE IX. – SUMMARY OF RADIATION TESTS ON SILICON PHOTOTRANSISTORS

Radiation source	Fluence	Reduction in n-p-n beta (current gain)
Gamma (Cobalt-60)	10^5 rad	10%
Neutrons (1 MeV)	10^{13} n/cm^2	20%
	10^{14} n/cm^2	75%
Electrons[a, b]	Not tested	—

[a]Damage from 100 MeV electrons (unshielded) will be approximately the same as that due to 1 MeV neutrons

[b]Energy required to create on electron hole-pair in phototransistor = 2.5 eV. Equivalent dark noise level = 0.66×10^6 photoelectrons/s

TABLE X. – COMPARISON OF SILICON PHOTOTRANSISTOR ARRAY WITH SIT AND SDA VIDICONS

Features	Phototransistor Array	SIT Vidicon	SDA Vidicon
Limiting resolution	[a] 390 TVL	[b] 600 TVL	[c] 750 TVL
Dynamic range	[d] $10^3/1$ [e] $2 \times 10^4/1$	[f] $10^6/1$	[c] $10^3/1$
Geometric distortion	[g] ±0.05%	[h] 4%	[i] 1% estimate
Electron beam bending toward highlights	N/A	[j] 1% max	[j] 1% max
White fiducial marks for geometric reference	Not required	Development required	Development required
Image blooming	1% cross-talk between adjacent elements	Problem area	Problem area
Lifetime - operating	LSA-tested to 3×10^6 hr w/o failure or degradation	TBD	TBD
Radiation resistance	10^3 rad (gamma) with no degradation	TBD	TBD

[a] Two LSA arrays
[b] RCA C21117B data sheet
[c] RCA C23136 data sheet
[d] With fixed integration time
[e] With 20/1 variation in integration time
[f] With $10^3/1$ variation in target gain
[g] $\pm 0.1 \times 10^{-3}$ alignment error between five LSAs
[h] R. W. Engstrom, E-O Systems Design, 6-71
[i] Assumes same distortion as 2-in. RBV
[j] Personal communication, RCA AED

7.0
FEASIBILITY DEMONSTRATION TESTS

The feasibility of obtaining imagery of the outer planets and their satellites from a spinning Pioneer type of spacecraft is demonstrated by simulation in the laboratory using an experimental model of a solid state photo-imaging system previously developed by TRW Systems.

With illuminated photographic transparencies used to simulate the characteristics of the planets and satellites, video data in digital form are recorded on magnetic tape from a data collection facility, also developed by TRW Systems.

Using gray-scale calibration data from the sensor, the video data are then corrected to eliminate the effect of variations in photodetector dark current and gain by means of processing by a CDC 6500 computer, and are formatted into a form suitable for reproduction on a laser beam recorder at a vendor's facility.

The flight model of the photo-imaging system will have a broad spectral bandwidth and will use an optical system with a low f-number. The experimental camera, designed to obtain multispectral imagery, uses four relatively narrow spectral bands and has an optical system with an f-number higher than that of the flight model. Only one spectral band is used in this demonstration.

To simulate the performance of the flight model in laboratory tests, the radiance levels of the test patterns must be increased to levels higher than those of the planets and the exposure time must also be increased to obtain the same exposure (in watt-seconds) and S/N ratios as the flight model.

The following method is applied to determine the test pattern radiance levels for the laboratory demonstration:

a. An analysis is performed to determine the S/N ratios obtained by the flight model photo-imaging system, when observing the outer planets and satellites illuminated by solar radiation of 6000°K radiation temperature.

b. The increase in planetary radiance levels is computed, using a simplified model of the experimental photo-imaging system in the laboratory, which will result in performance (S/N ratios) equivalent to the flight model. A uniform or "square" spectral passband is assumed for the experimental system in the model, and the increases in test pattern radiance levels assume that patterns are illuminated by radiation of 6000°K radiation temperature.

c. The test pattern radiance levels are then corrected to equivalent values of incandescent illumination (2860°K radiation temperature), and correction is also made for the true spectral passband characteristic of the experimental system.

d. A test program plan is developed from these data, with the optical transparencies simulating planetary images at illumination levels covering the range from Jupiter at 5.2 AU to Uranus at 19.2 AU.

In the following pages of this section, the equipment used in the feasibility demonstration is described, the test program is developed, and the results of the demonstration are presented.

Experimental Photo-Imaging System

The engineering model of a solid state multispectral photo-imaging system has been developed to demonstrate the capability of producing high-resolution multispectral imagery using TRW high density phototransistor arrays. The model (Figures 28 and 29) uses three linear arrays consisting of one 6-chip array (1170 detectors) and two 2-chip arrays (390 detectors each array). The 6-chip array is used to demonstrate high-resolution monochrome capability, while simultaneous data collection from three 2-chip arrays, each sensing a different spectral band (green, red, near-IR), provides multispectral capability.

A single lens assembly with a speed of f/4 and color-corrected over the spectral range of 0.5 to 1.0 μm is used for collection of the broadband radiation and for imaging at the four planes. Spectral band separation is achieved through a unique arrangement of dichroic filters and internally reflecting prisms (beam splitters). The four spectral bands provided are from 0.5 to 0.6, from 0.6 to 0.7, from 0.7 to 0.8, and from 0.8 to 1.0 μm. The effective focal length is 100 mm with a FOV of 10.8 deg. The optical system is capable of operation with object distances of 100 cm and infinity.

Figure 30 is a functional block diagram of the system. The sensor, simulating spacecraft motion normal to the array, is mounted on a motor-driven precision rotary table to provide the proper spatial sampling rates of the image. Rack-mounted equipment provides power, timing signals, and video signal

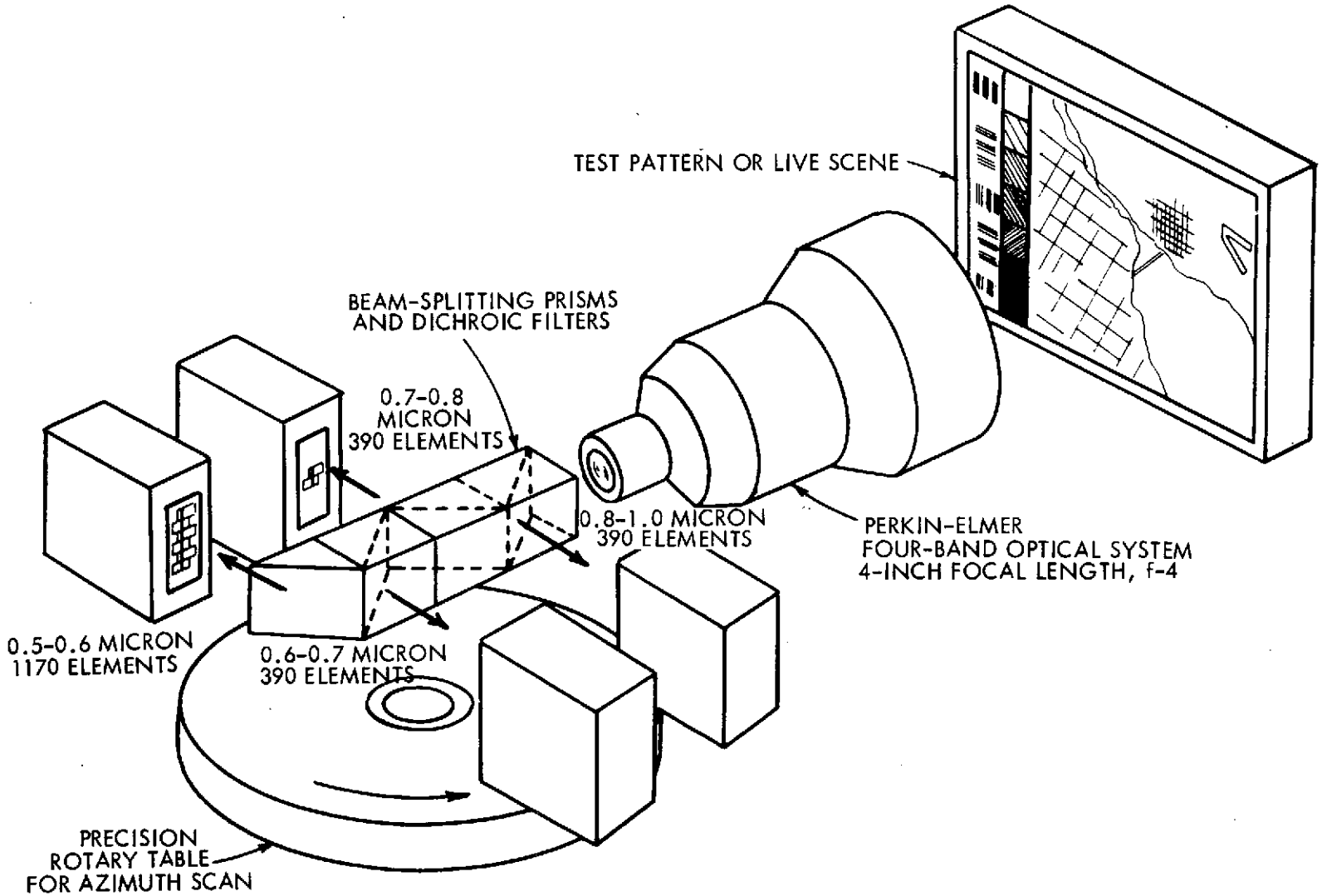

FIGURE 28. – SOLID STATE MULTISPECTRAL PHOTO-IMAGING SYSTEM

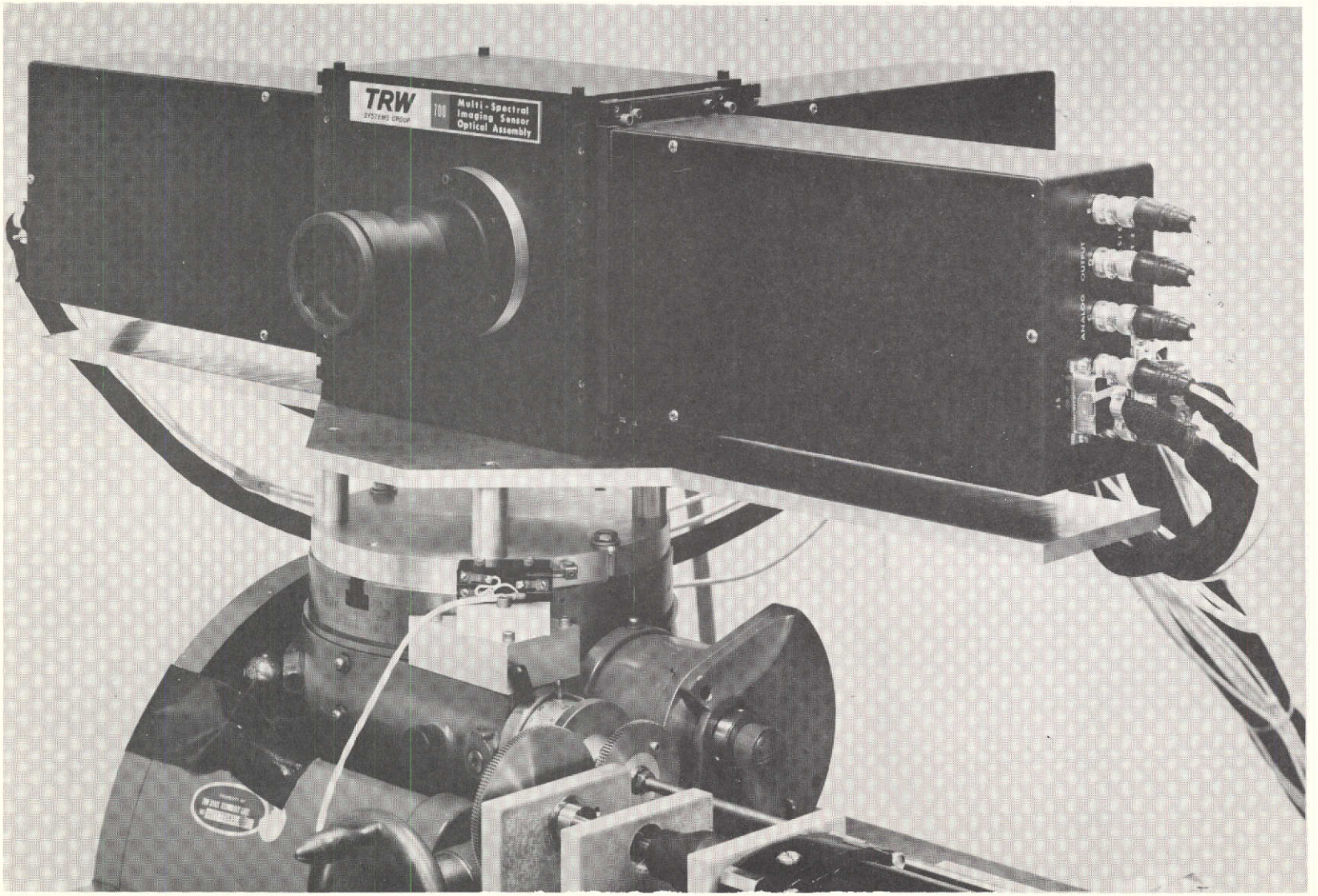

FIGURE 29. – EXPERIMENTAL PHOTO-IMAGING SYSTEM ON ROTARY TABLE

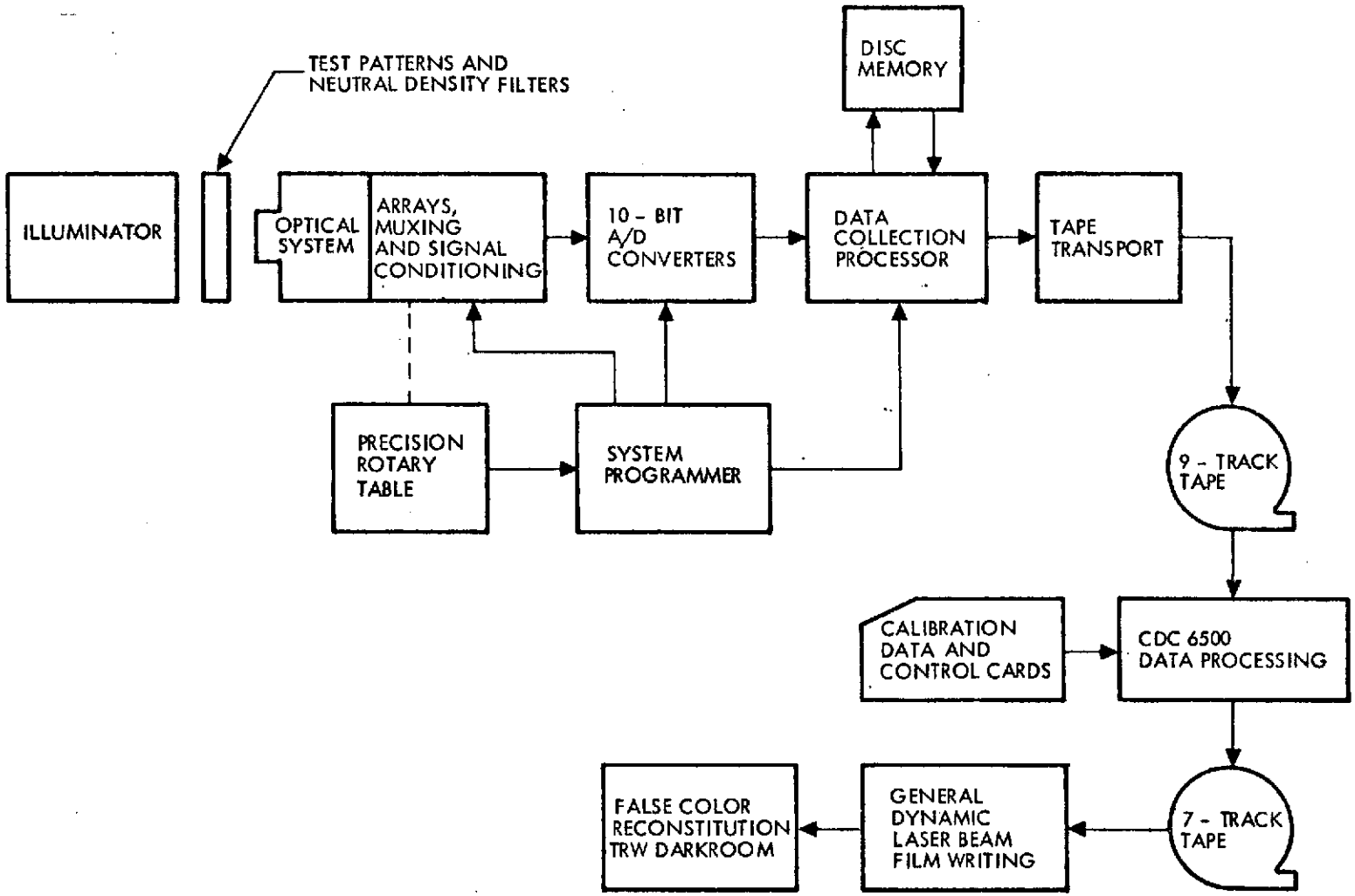

FIGURE 30. – FUNCTIONAL BLOCK DIAGRAM OF THE SYSTEM

encoding. The digital video data from the analog-to-digital converters are collected with a high-speed data collection facility with a capacity of approximately 2-million bits. The output of the data collection facility is recorded on 9-track computer-compatible magnetic tape. Computer software is used to linearize the detector response, reformat the data, and generate gray levels (density increments) to a film writer. A laser beam film-writer generates B&W photographic images from the digital data.

In the proposed test program, monochrome imagery will be obtained in the laboratory by simulating planetary imagery that would be obtained from a spinning spacecraft. Only one of the four spectral bands of the experimental multispectral photo-imaging system will be used: the 0.5 μm to 0.6 μm spectral band. To simulate the 2-chip (390-detector element) array of the space-borne camera, only two of the 6 chips of the array in this spectral band will be used.

Data Collection Facility

The data collection facility, which records input data on magnetic tape in a format suitable for computer processing, consists of a data collection processor, a disc memory, and a magnetic tape transport with formatter. Input data are received from analog-to-digital converters working in parallel and controlled by a programmer. A block diagram of the system is shown in Figure 31, and the equipment is shown in Figure 32.

Data buffering in the form of an LSI random-access memory in the processor and the disc memory is required to attain data-rate compatibility with the tape recorder.

Image Generation Software

A software program has been developed for reformatting the data collected on digital tape to obtain compatibility with the laser beam film-writer used for image reconstruction at a vendor's facility. This program also provides for

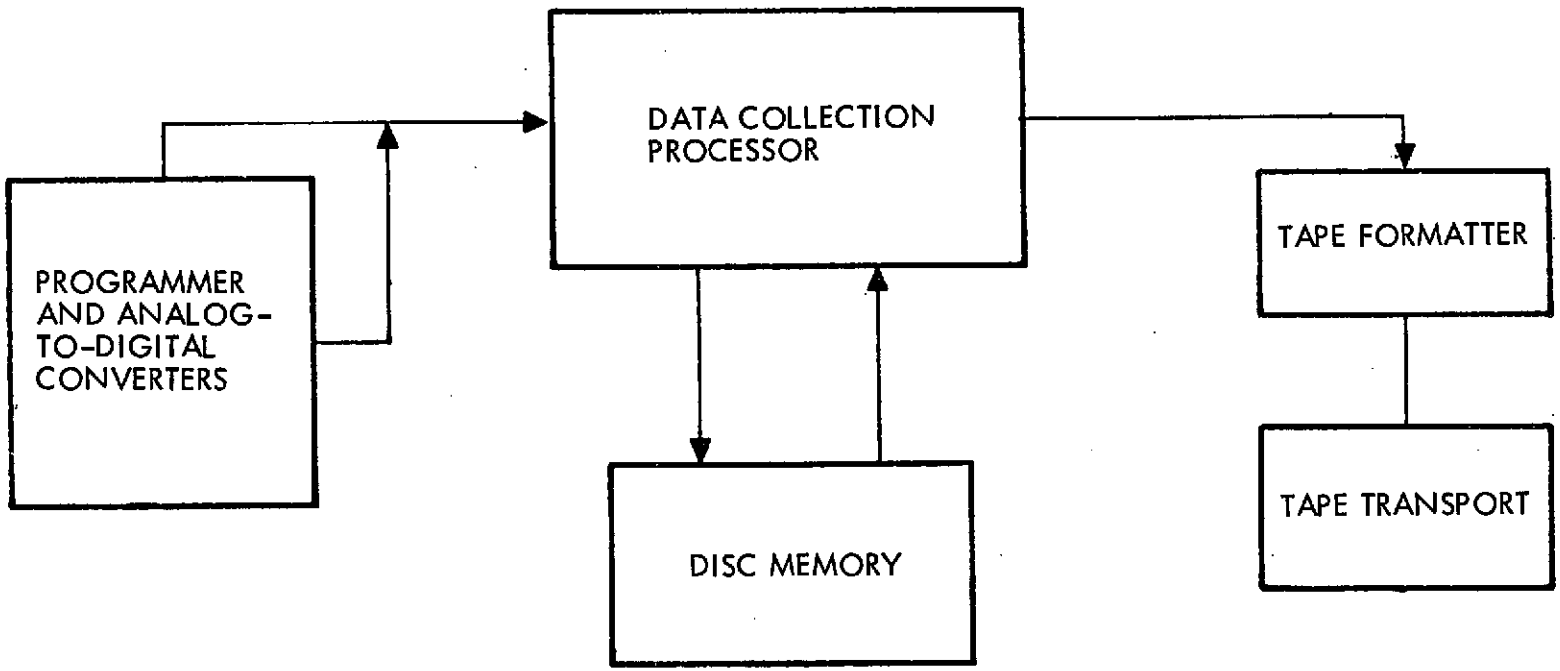

FIGURE 31. – DATA COLLECTION FACILITY

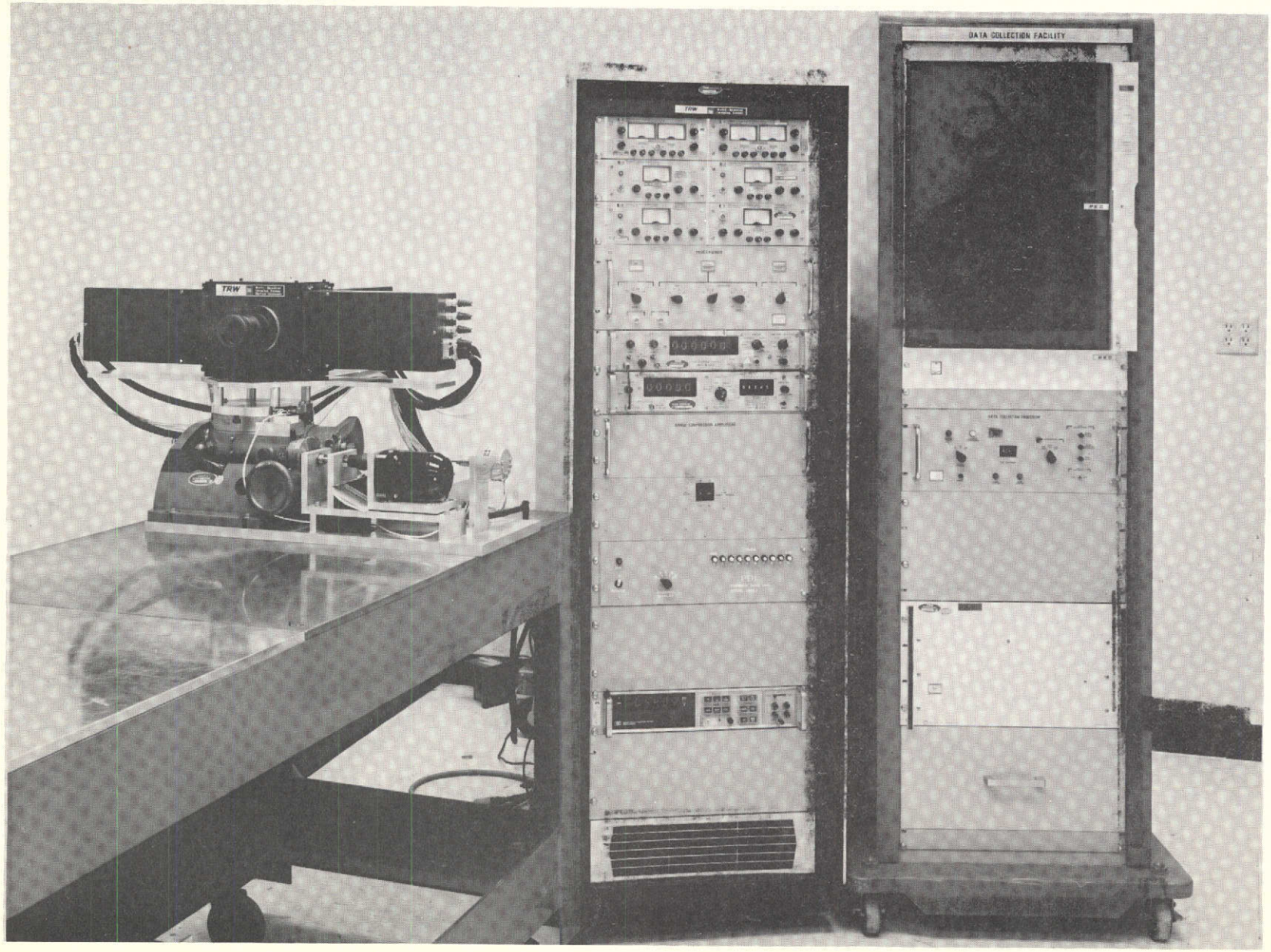

FIGURE 32. – EXPERIMENTAL PHOTO-IMAGING SYSTEM AND DATA COLLECTION FACILITY

calibrating the detector arrays. To eliminate the effect of nonuniform responsivity and dark current of the detector elements of the phototransistor array, the output of each element is sampled 160 times at each level of an 8-step gray scale (one dark level plus eight shades of gray). Linear interpolation of the detector current levels between gray scale calibration is employed. A 16-step gray scale is also printed on film by the laser beam film-writer, in conjunction with the record of the imagery obtained in the laboratory.

Test Pattern Illuminator

The test pattern illuminator consists of ten General Electric 75-W tubular showcase lamps, type 75T10/45, approximately 25 centimeters (ten inches) long in a planar array with approximately 2.5 centimeter (one-inch) spacing between filaments. The array is mounted in an enclosure with a matte aluminum reflector on the back and an opal glass diffuser on the front. The clear area of the illuminated section is 6 x 6 cm. The nominal operating voltage of the lamps is 120 Vdc. The spectral irradiance of the illuminator has been measured by comparing it with a Gamma Scientific standard irradiance source using a silicon solar cell with narrow-band optical filters. Values are listed in Table XI and plotted in Figure 33. The lamps in the illumination source are operated at a radiation temperature of approximately 2650°K.

From the data specified in the table, the equivalent spectral irradiance of the illuminator in terms of equivalent solar irradiance at a radiation temperature of 6000°K has been computed at 25.7% of one solar constant. This is equivalent to a value of solar irradiance of 92.1 W/m^2-0.1 μm from 0.5 to 0.6 μm. The corresponding value of radiance is $92.1/\pi = 29.3$ W/m^2-sr-0.1 μm.

Details of the calibration of the test pattern illuminator are contained in Appendix A. In the following sections, detailed information pertinent to the feasibility test demonstration is presented on the configuration of the various components.

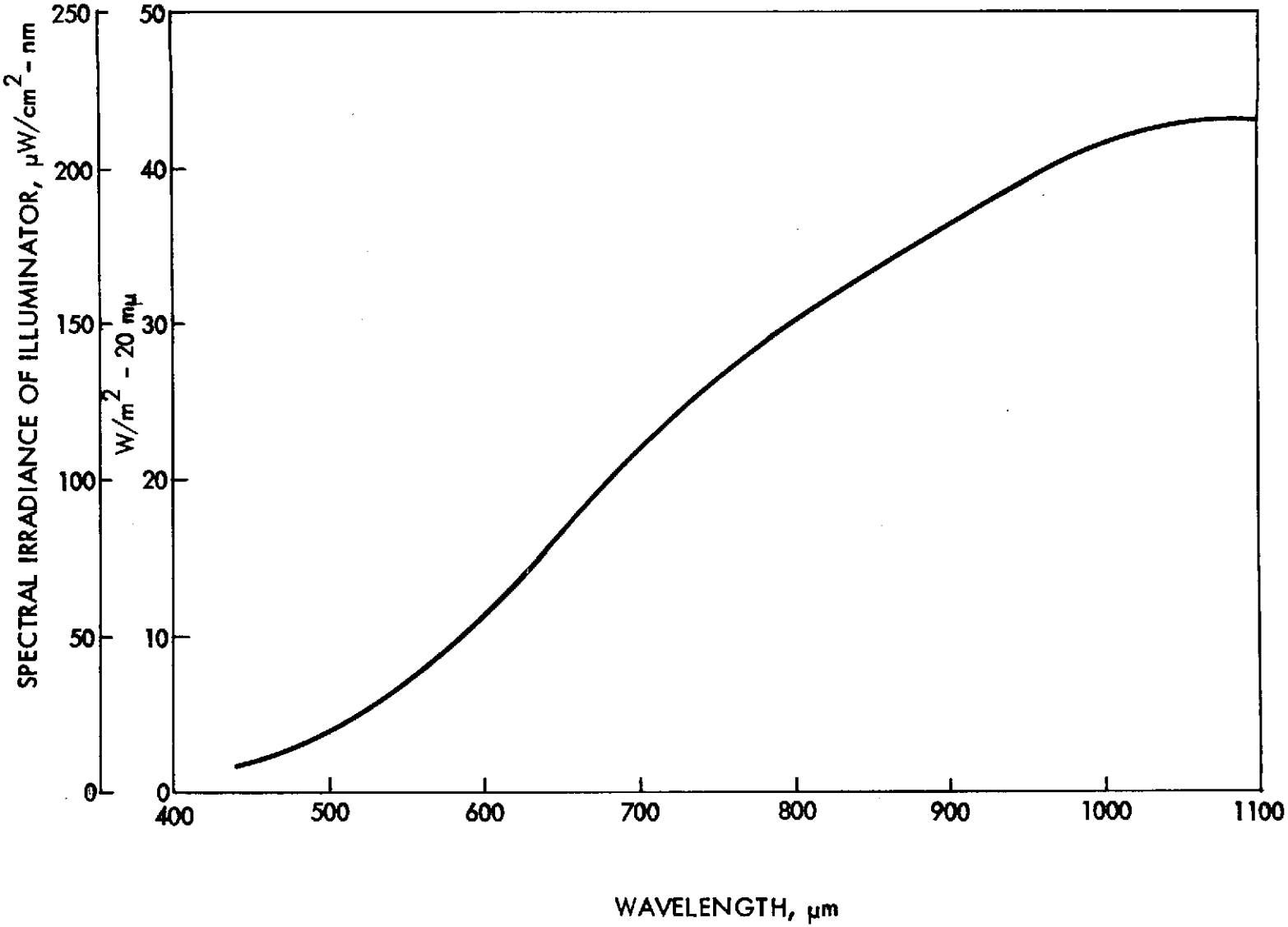

FIGURE 33. – SPECTRAL IRRADIANCE OF TEST PATTERN ILLUMINATOR

TABLE XI. – SPECTRAL IRRADIANCE OF TEST PATTERN ILLUMINATOR

Wavelength, nm	Spectral Irradiance of Illuminator, $\mu W/cm^2$-nm	Solar Spectral Irradiance, $\mu W/cm^2$-nm	Equivalent Spectral Irradiance of Illuminator of One Solar Constant, %
443	8.81	190	4.6
474	12.81	204	6.2
506	20.90	192	11.0
538	31.36	180	17.4
553	38.84	172	22.6
605	58.20	165	35.2
673	99.29	144	69.0
705	115.79	135	86.0
790	145.50	114	127.0
885	167.02	92	181.0
995	205.96	75	273.0
1095	213.13	59	360.0

7.1
Detailed Description of Equipment

Experimental Photo-Imaging System

Optical System Characteristics

The configuration of the optical system is illustrated in Figure 34. Developed by the Perkin-Elmer Corporation under subcontract to TRW Systems, the system uses a common objective lens in conjunction with internal reflecting prisms (beam splitters) and dichroic filters to separate the incoming radiation into four spectral bands. Capability of operation with object distances of either infinity or 100 cm (40 in.) is provided. In the 100-cm distance, a shim is used to increase the effective focal length. The characteristics of the system, as measured in acceptance testing, are defined in Table XII.

The system has four spectral bands: green, red, near-infrared, and infrared. The spectral transmission of each band is illustrated in Figure 35.

The measured chromatic separation is specified in Table XII. The chromatic cross-talk requirement of 15% was exceeded in the green and red bands. Resolution exceeded the requirement of 70 lpm in all bands, and the measured MTF values did not degrade significantly when the lens-object plane distance of 100 cm was used. Registration in all four bands was better than the requirement of ±5 arc-s.

Electronic Configuration

Phototransistor arrays. – The three phototransistor arrays consist of two to six large-scale arrays (LSAs) mounted and aligned on a BeCu block (subcarrier). A LSA is composed of a large-scale integrated (LSI) chip having 195 detectors with multiplexing circuitry, and a smaller preamplifier chip bonded to a ceramic substrate which in turn is epoxy-bonded to the LSA substructure. The photodetectors operate in the photon flux integration mode (charge storage mode) in which photogenerated current discharges the capacitance of a reverse-biased p-n junction from a preset charge level. The current required to recharge the capacitance during readout is amplified and is

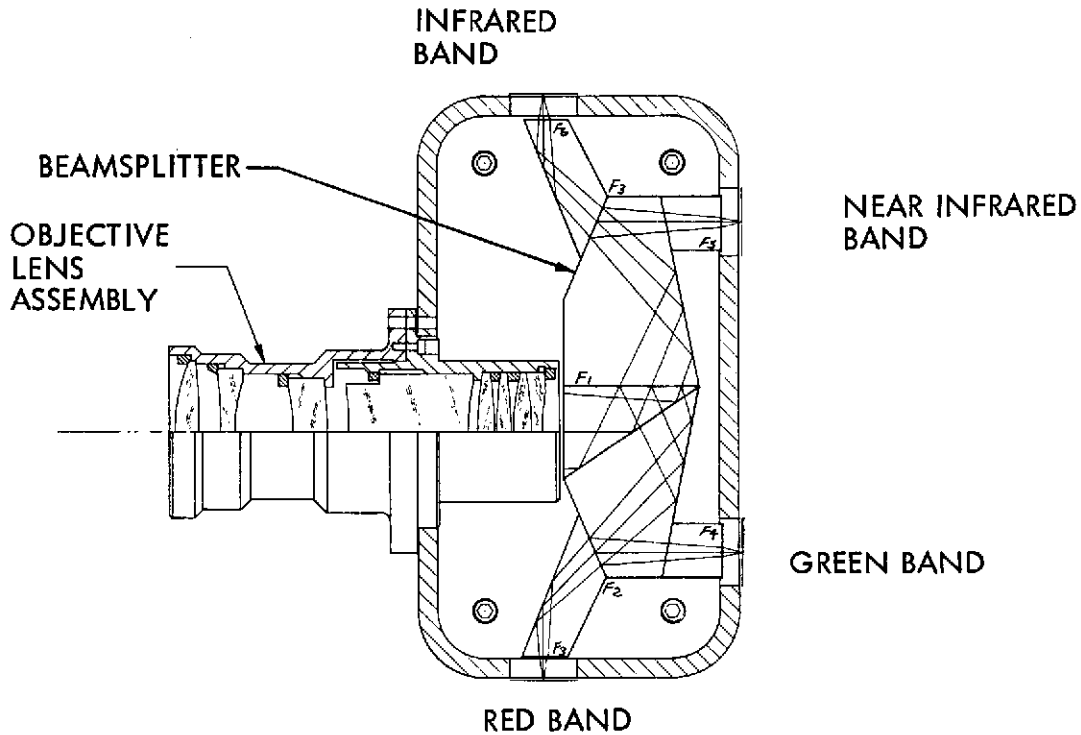

FIGURE 34. – OPTICAL SYSTEM CONFIGURATION

TABLE XII. – OPTICAL SYSTEM CHARACTERISTICS

Spectral Band	Spectral Separation Å (50% Crossover Points)	Chromatic Crosstalk, %		Resolution, MTF				Registration, arc-s
		At Short Wavelengths	At Long Wavelengths	On Axis		Full Field		
				Tan.	Rad.	Tan.	Rad.	
Green	5000 - 6020	1	30.3	92	91	90	83	-0.5
Red	6020 - 7180	8	19	87	92	90	88	+2.5
Near IR	7180 - 8200	11	9	84	86	89	86	+0.5
IR	8200 - 11 000	6.5	Not measurable	81	85	81	84	-2.5

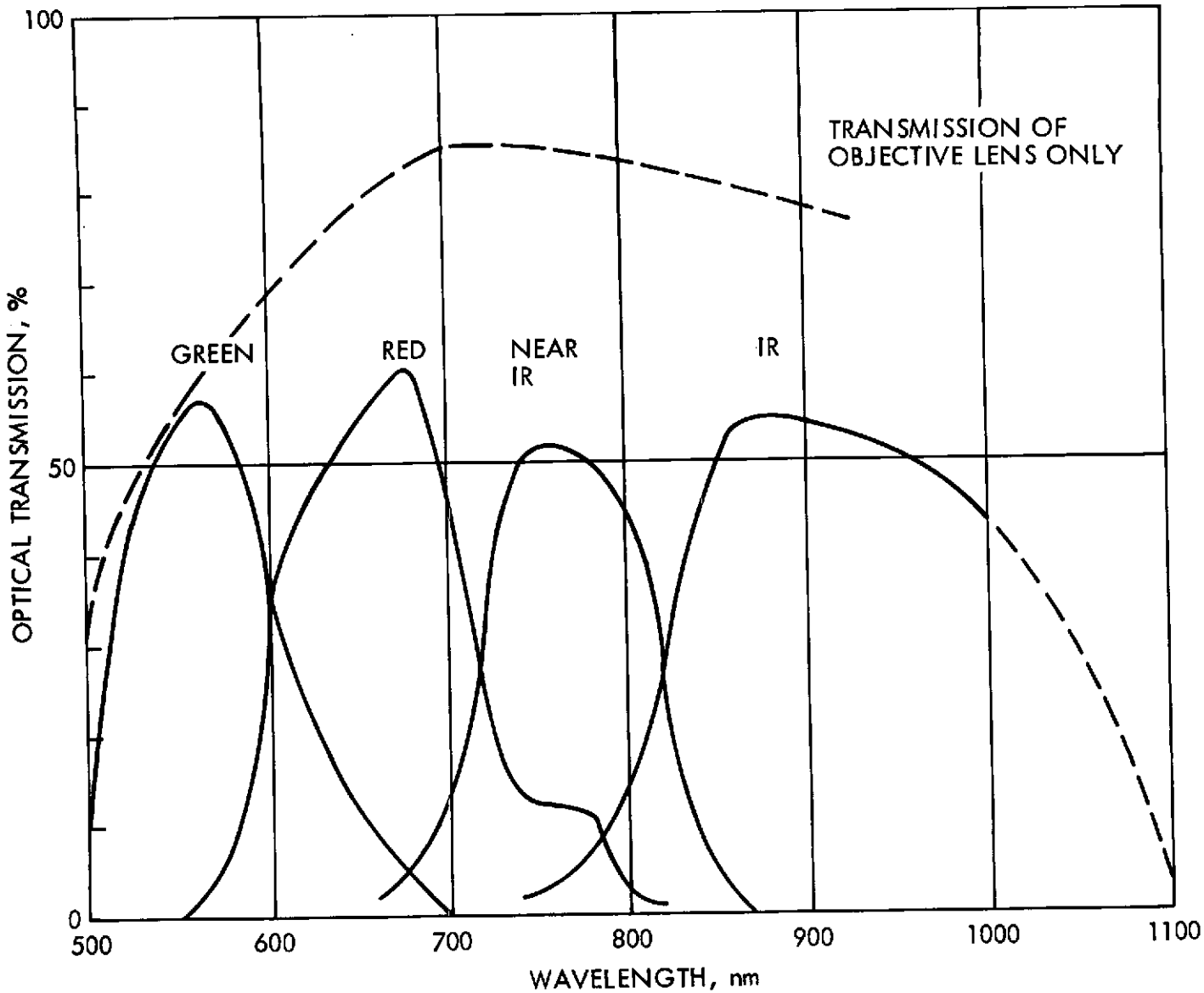

FIGURE 35. – TRANSMISSION OF MULTISPECTRAL OPTICAL SYSTEM

proportional to the incident illumination. The output signals from the 195 detectors are multiplexed into five video channels on the LSI chip. A second level of multiplexing is accomplished by connecting the five preamplifier outputs of each LSA to five common buses and then sequentially interrogating each LSA. LSAs selected for the arrays have a mean noise equivalent signal (NES) less than 1.2 $\mu J/m^2$. The minimum LSA response is 0.6 $\mu A/\mu J/m^2$. Maximum incident radiant energy on a detector is 540 $\mu J/m^2$. Detector interrogation cycle periods are 1.2, 2.4, or 4.8 ms. No active thermal control is provided for the LSAs.

Input/output signal conditioning units. – Three I/O conditioning units provide the properly conditioned signals and dc voltage for operating the LSAs (Figure 36). These signals and the dc voltage are as follows:

S	Shift register set and preamp enable
R	Shift register reset
C1	Odd-stage shift clock and preamp clamp
C2	Even-stage shift clock and preamp clamp
C3	Readout clock and charge pulse
V1	Detector bias, normally at +3 V dropping to -2 V for 10 μs of each cycle period for detector saturation.
+3V	Switch power and preamp bias.

In addition, each I/O unit contains five signal current amplifiers for boosting the power level for driving a 95-ohm coaxial cable to the range compression amplifiers. The I/O units physically mount to the optical system. The balance of the electronics are mounted in relay racks.

Range compression amplifiers. – This unit accepts the 15 video signal lines from the three I/O units and a 4-bit code from the programmer.

Gain and offset compensation is automatically optimized for the LSA being interrogated, reducing the channel range expansion factor (REF) to essentially the REF of a single LSA channel, and thereby assuring that 8-bit video encoding is accomplished.

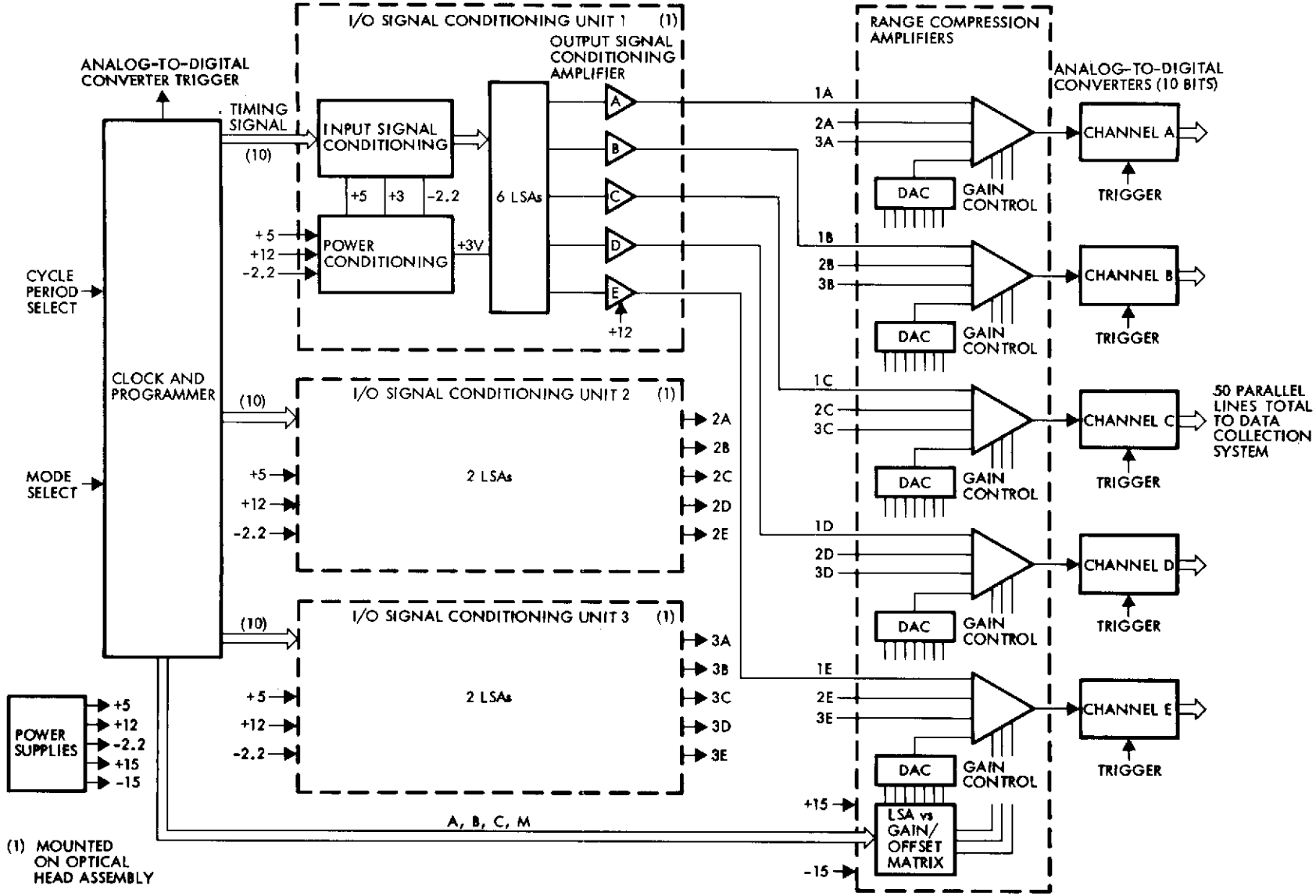

FIGURE 36. – ELECTRONIC CONFIGURATION - EXPERIMENTAL PHOTO-IMAGING SYSTEM

A/D converters. – Five 10-bit A/D converters with video signal sample-and-hold amplifiers capable of acquiring the pulsed video waveform are used for sampling and encoding the video signals.

Programmer unit. – A programmer unit provides timing signals to the I/O units for generating the LSA control signals. The programmer also provides trigger signals to the A/D converters. All timing is generated from a crystal controlled oscillator. The system cycle period is selected from the programmer panel as well as the operating mode.

Angular position measurement. – A precision rotary table is used to rotate the camera at the scan rate corresponding to the selected detector integration period. The table is driven by a Bodine synchronous gear motor through a gear train. Gears can be selected to provide angular rates of 0.0284, 0.0568, and 0.1136 rad/s. An optical shaft encoder with 1024 counts per revolution is used for indexing the table. Two counters are used for table indexing. One counter counts from the reference point while keeping track of the location at which data collection ceases, and another counter starts the data collection at that location for the next file of data.

Data Collection Facility

The data collection facility consists of a data collection processor, a disc memory, and a magnetic tape transport with formatter. Input data is received from five A/D converters operating in parallel and controlled by the data source programmer. A functional diagram of the system is shown in Figure 37.

The data collection facility records input data on magnetic tape in a format suitable for computer processing. Extensive data buffering in the form of an LSI-random access memory in the processor and the disc memory is required to attain data rate compatibility with the tape recorder.

Components of the data collection system are contained in a single cabinet. The processor is housed in a 7-in.-high drawer with the power supplies and RAMs mounted on the baseplate. A wirewrapped plane mounted above

the baseplate contains all the processor logic circuits and interface connections.

The processor/controller provides control of the facility and MOS RAM line-buffering. It receives parallel data from the five 10-bit A/D converters at 500 KHz peak sampling rates and multiplexes the data onto the disc memory. The disc stores 160 samples from each of the detectors. This data is then transferred to 9-track computer-compatible magnetic tapes at 45 in./s. Pertinent features of the data collection facility are summarized in Table XIII.

Image Generation Software

The software required to generate image data tapes compatible with the Convair/General Dynamics laser beam recorder film-writing facility is described in the following paragraphs. Input to this program is a magnetic

TABLE XIII. – DATA COLLECTION FACILITY CAPABILITIES

Data storage capacity[a]	1.9 million bits		
Input			
Data rates	25 million bits/s (peak) (500K words/channel/s x 5 channel x 10 bits/word) ~10 million bits/s (av) (1170 det x 10 bits/sample x 833 samples/s)		
Data format	50 parallel lines (Five 10-bit channels)		
Output	Nine-track computer Compatible tape		
[a]Equivalent image raster	B&W	1170 x 160	TV lines
		390 x 180	TV lines
	Three-Color	390 x 160	TV lines

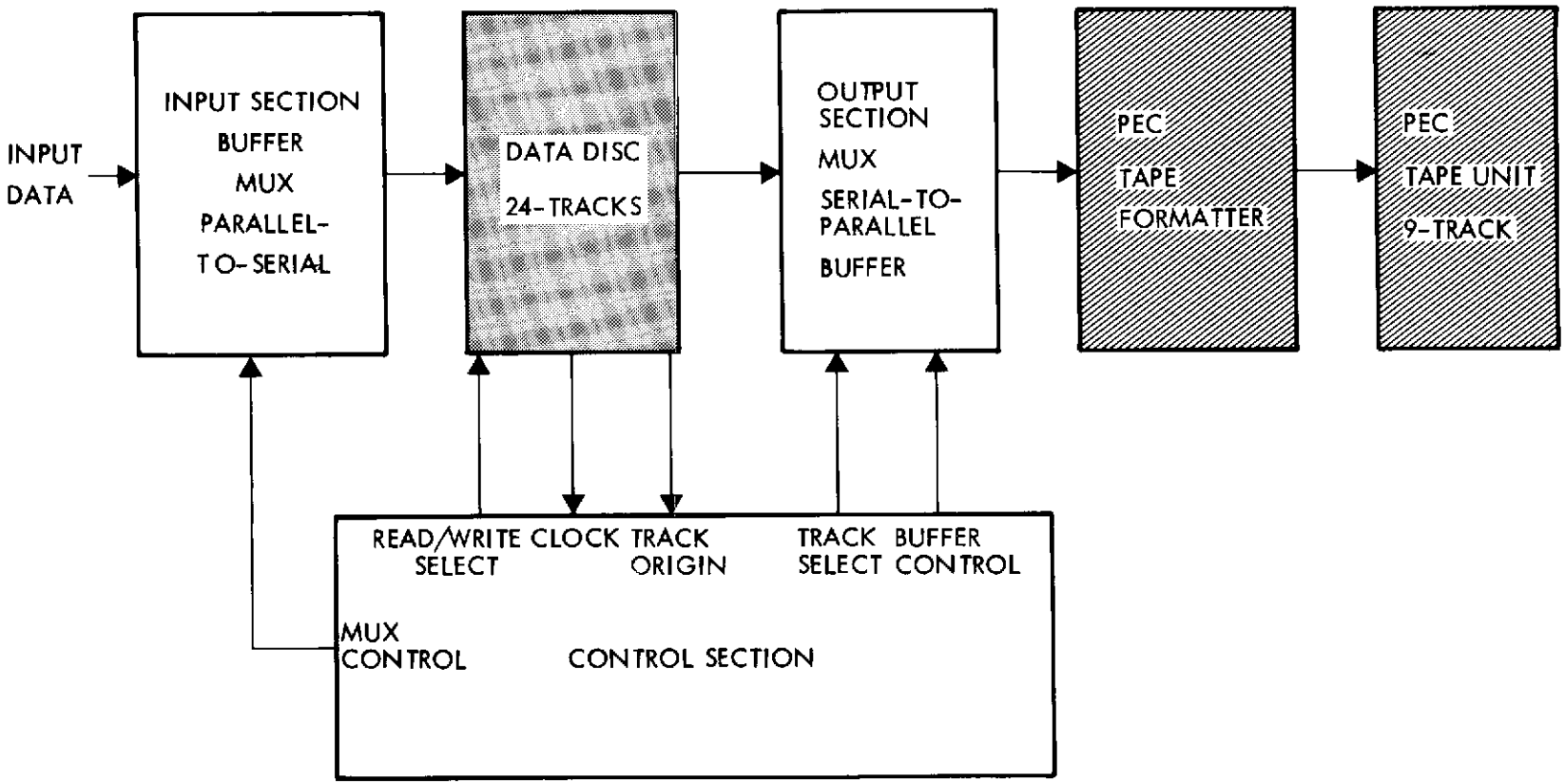

FIGURE 37. – FUNCTIONAL DIAGRAM DATA COLLECTION FACILITY

tape generated by the TRW Data Collection Facility, with associated data processing IBM cards.

The basic tasks involved in the processing are these:

a. Reorder and reformat data

b. Correct for time delay between the two rows of detector elements

c. Correct for detector-to-detector variations in gain and dark level according to supplied calibration information

d. Calculate the NES for each detector at dark level.

The steps followed to execute these tasks are as follows:

a. Read raw data from magnetic tape

b. Store detector calibration data - mean of 160 samples from each detector for 5 to 10 irradiance levels (including dark level)

c. Compute and print NES for zero input irradiance for each detector

d. Write gray level tape for driving a laser beam film writer.

A brief discussion of the software program follows.

Raw Data Tape Format

The raw data samples are 12-bit words recorded on 9-track NRZI, 800 characters per inch of magnetic tape. A tape record is one line-scan of six LSAs, each having 195 detectors. The 12-bit data samples (10 significant bits, two LSBs are 0's) are written as a continuous-bit stream; MSB first for LSA #1, detectors 1 through 195; then LSA #2, detectors 1 through 195, with LSAs 3, 4, 5, and 6 following. A file consists of 160 records or samples from each of 1170 detectors. One irradiance level or test condition or scanned test pattern makes up a file. Each record contains an identification header consisting of the line or record number, and the file number.

Sensor Calibration

Eight input irradiance levels are provided as inputs to the sensor. Corresponding measured irradiance levels are input to the computer with punched

cards. The average count for 160 samples from each detector at each input level is computed and printed. These values are also retained to determine the calibrated response of each detector.

Noise Equivalent Signal

The standard deviation for the 160 samples taken for zero input irradiance is computed for each detector and divided by the gain (slope of the first line segment of a piecewise linear curve fit). This value is printed as the NES for each detector.

Film Writer Tape

A seven-track tape is formatted for laser beam film writing at General Dynamics. Using the calibration points for a piecewise linear calibration, the irradiance value is computed for each picture element. The response (I_X) is normalized for each detector sample with respect to the maximum irradiance (I_{max}) on any detector in any spectral band for a particular scene. The gray level number is computed according to the following equation, assuming the film writer dynamic range to be a density of 1.82 above a base of 0.08.

$$\text{Gray level} = 255 \left(1 - \frac{1}{1.82} \log \frac{I_{max}}{I_X}\right)$$

The data is arranged in such a way that the laser beam scans the film in a direction corresponding to the detector array orientation. The spatial formats of the detector arrays are shown in Figure 38. The system operates in two modes: a high resolution mode and a multispectral mode. In either mode, six LSAs are interrogated. The data sequence for the high resolution mode is LSAs 1 to 6 sequentially. One file of raw data contains 160 lines. Rasters of 960 lines (six raw data files) on the film writer drive tape are desirable. In the multispectral mode, the data sequence is LSAs 7, 8, 3, 4, 9, and 10. Two files of raw data are recorded for each test pattern in this mode to generate 320 line rasters. A 320 line x 390 element spectral negative can be written for each of

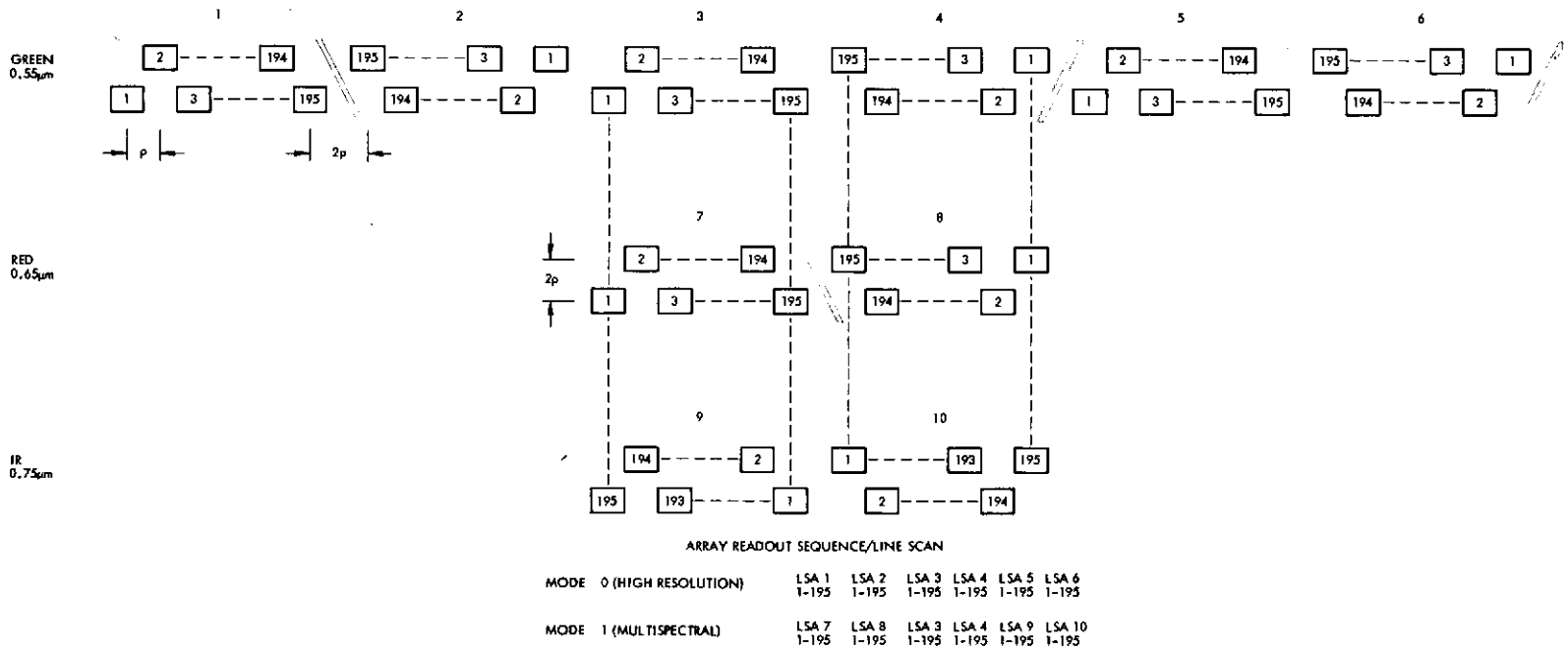

FIGURE 38. – ARRAY READOUT FORMATS

the three spectral bands for red, green, and blue false-color reconstitution with no changes in procedures or processing. A 16-step density wedge also appears on each negative, corresponding to an electronically generated input scale.

Image Reconstruction Facility

A brief description of the operation and performance of the General Dynamics laser beam recorder image reconstruction facility follows.

The L-70 laser printer utilizes a 1 milliwatt helium-neon laser. Figure 39 shows this laser in the upper left corner with its light beam directed to the right through the modulator and optics train. Just to the right of the laser is an acousto-optic modulator which is driven with a constant-frequency, amplitude-modulated signal to control the intensity of the laser beam. The circular disc is a continuously variable, neutral density filter for reducing laser intensity, depending on the film being used. To the right of this filter is a beam expander and to the right of the expander is an aperture to delete the so-called Io beam – the beam portion not deflected by the modulator.

The right parallelepiped above the black table-like surface houses the one-facet spinner which is driven by a hysteresis synchronous motor; motor speed is controlled, open loop, by a precision oscillator. The laser beam is deflected radially by the spinner to the film focal surface which is a right circular cylinder. Chip film, 4 x 5 in., is held in this cylinder which is advanced by a precision lead screw driven by another hysteresis synchronous motor.

The L-70 is capable of producing images having a format of 4000 x 4000 image elements at a rate of 150 kilowords (elements) per second. Since this is compatible with computer and tape speeds, the device is convenient for laboratory use where the source data is likely to be on tape. A 10-bit D/A converter is used and a film density range of 2.2 can be achieved. Performance details of this laser printer are summarized in Table XIV. Although a 10-bit digital-to-analog converter is used, laser noise currently limits performance to just under 7 bits (128 intensity levels).

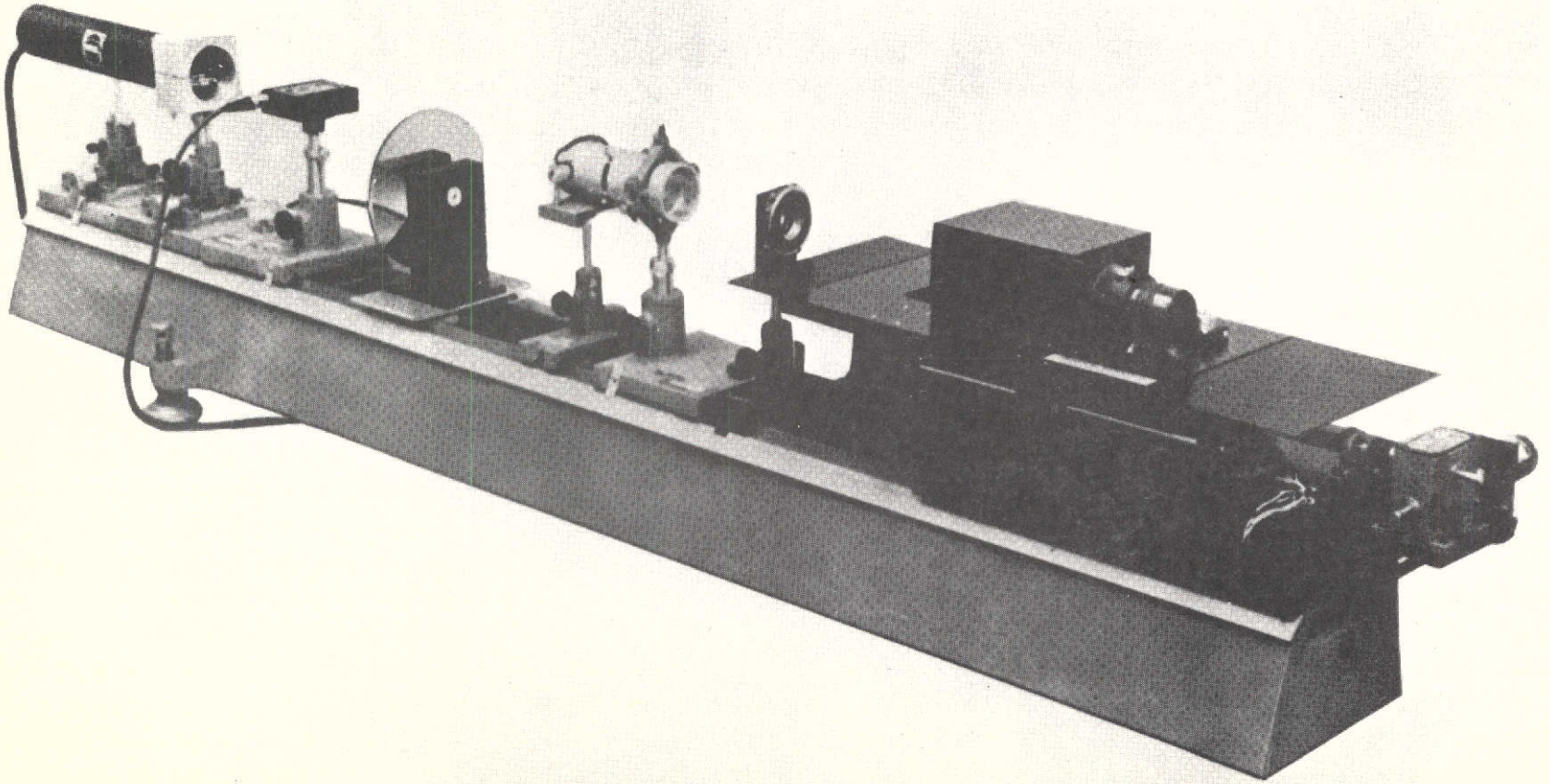

FIGURE 39. – GENERAL DYNAMICS LASER BEAM FILM RECORDER

TABLE XIV. – LASER BEAM FILM RECORDER: SUMMARY OF CHARACTERISTICS

Characteristic	Value
Laser type	He-Ne
Laser power	1 mW
Writing rate	150 kilowords per second
Line rate (max)	20 lines per second
Writing rate control	±10%
Line start position control	±10%
Line pitch control	None
Spinner speed	20 revolutions per second
Number of facets	1
Maximum capacity	1000 words per inch
Spot size	24μ
Output intensity levels	256 (8 bits)
Dynamic range	200 to 1
Film size	4 in. x 5 in. cut
Film type	3414
Film density range	> 2.0

The radiometric control process is extended through the reconstruction of images with the L-70 laser printer. The first step in the laser printing radiometric control is to convert the image tape containing reflectance or luminance data to a tape containing 8-bit digital values representing the density range of the film to be exposed on the printer. This conversion is given by

$$SOG(L) = \frac{255}{D1 - DO} (-\log_{10} T(L) - DO)$$

where

SOG(L) is directly proportional to density

DO is minimum density on film

D1 is maximum density on film

$$T(L) = mL + b$$

L input reflectance or luminance

$$m = \begin{cases} (T1 - TO)/(L1 - LO) \text{ for positive} \\ (TO - T1)/(L1 - LO) \text{ for negative} \end{cases}$$

$$b = \begin{cases} TO - mLO \text{ for positive} \\ T1 - mLO \text{ for negative} \end{cases}$$

LO, $L1$ are minimum and maximum luminance

$$TO = 1.0/10^{D1}$$

$$T1 = 1.0/10^{DO}$$

This conversion provides a linear relationship between the reflectance or luminance values and transmittance values on the film.

The second step in the radiometric control of the reconstructed images is to precompensate digitally for the nonlinear transfer functions of the laser modulator and the film. The precompensation is performed by altering the 8-bit digital values, which are proportional to density, with a nonlinear transfer curve before they are converted to an analog signal driving the modulator. The shape of the nonlinear transfer curve is obtained by a calibration procedure in which 17 distinct digital values (over the entire dynamic range) are used to drive the modulator while film is being exposed. The film is developed using the standard procedures, and the densities for each of the 17 levels are measured. The density/digital value points resulting from this process are used to generate the precompensation function that provides radiometric control to the final digitally reconstructed product. The precompensation function is very nearly linear for a wide range of density in the final product.

7.2 Simulation of Flight Model Performance in Laboratory Demonstration

In the laboratory feasibility demonstration, the conditions of testing with the experimental photo-imaging system must correspond to those conditions to be encountered with the flight model. Specifically, the illumination levels used

for the photographic test patterns which simulate planetary imagery must give an equivalent exposure (in watt-seconds) on the phototransistor array in order to give equivalent S/N ratios and resolution that will result in image quality nearly identical to that which would be obtained in space flight.

The method that will be used to obtain the proper test conditions in the laboratory has been briefly discussed in the introductory paragraphs of this section. For a more complete understanding of this method, a more detailed discussion follows.

In the flight model (Figure 40(a)), the system will observe planets illuminated by solar radiation of 6000°K radiation temperature (the spectral radiance of the planets will be modified by the spectral characteristics of the planet albedo, and this is considered in the analysis). An optical transmission value of 50% is assumed, uniform over the range of spectral response of the photoimaging system from 0.4 to 1.1 μm. An f-number of 1.23 is assumed. The first step in the analysis is to determine the performance of the flight model under these conditions.

In Figure 40(b), a simplified model is used for the experimental laboratory system. The simplification consists of assuming that the spectral response is uniform over the spectral range of 0.5 to 0.6 μm, with a sharp cutoff at these two wavelengths, and with a 35% optical transmission within this range. This equivalent "square" spectral passband has been calculated as equivalent to the true response of the experimental within one percent, by computing the number of photoelectrons generated by the phototransistor array using either of the two spectral response curves. The f-number of the experimental optical system is 4.4 in the laboratory tests, with the object plane (test pattern) being only 100 cm (40 in.) from the objective lens.

As indicated in the Figure 40, levels of planetary radiance higher than the true values will be required to obtain the same performance (S/N ratios) as in the flight model because of the narrower spectral bandwidth. The second step in the analysis is to compute the factors by which the radiance levels must be increased, assuming that the spectral characteristics of the planetary radiation are unchanged (planets illuminated by solar radiation).

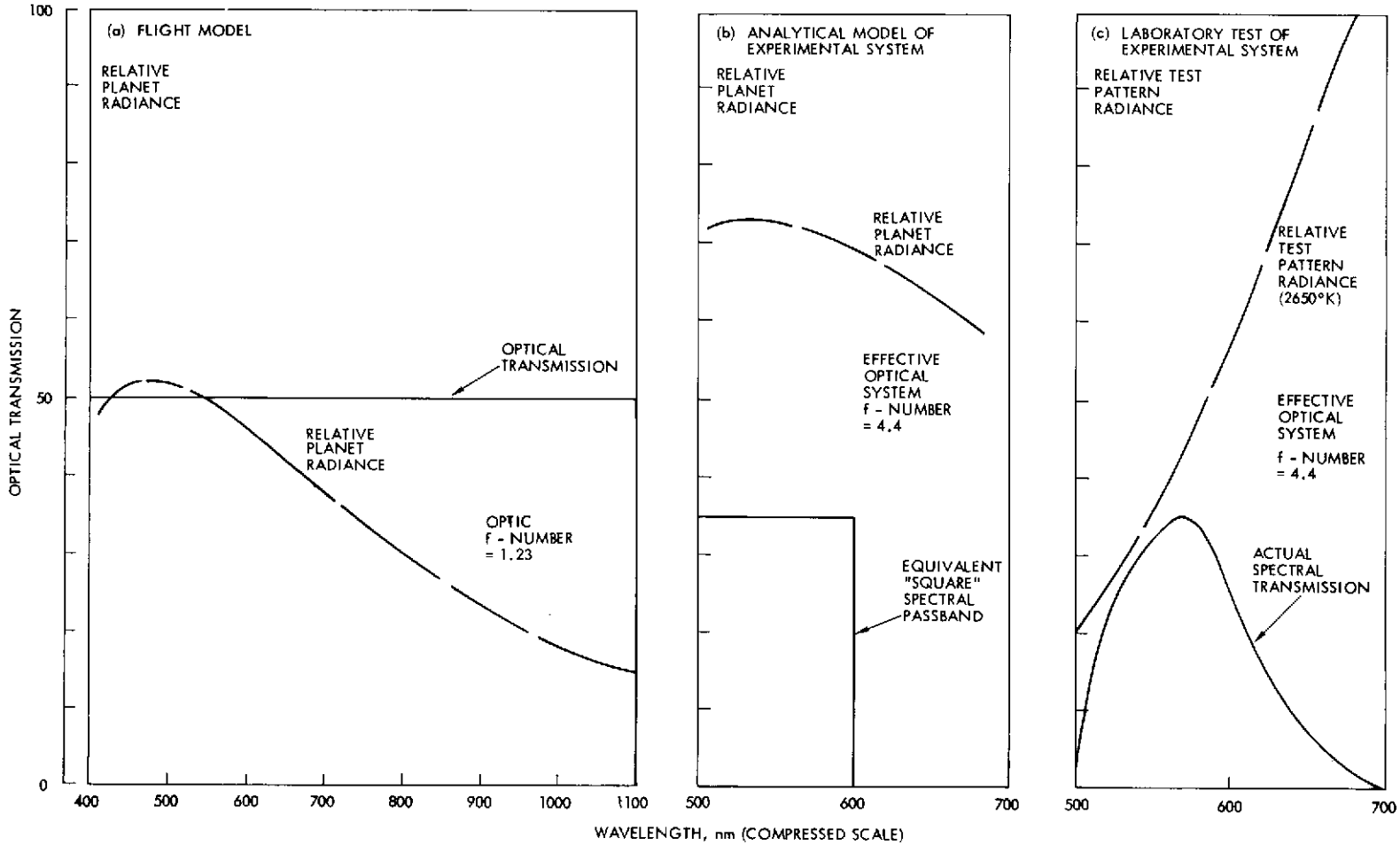

FIGURE 40. – COMPARISON OF TARGET AND SENSOR SPECTRAL CHARACTERISTICS

The true conditions of testing in the laboratory are illustrated in Figure 40(c). Incandescent lamps of 2650°K radiation temperature are used in the test pattern illuminator. In addition, the true spectral transmission of the optical transmission is not uniform, but varies with wavelength as shown in the figure. Thus, the third step in establishing test pattern illumination levels in the laboratory is that of correcting the values for (a) incandescent illumination, and (b) the true spectral response of the experimental system.

7.2.1
Parametric Model for Performance Analysis

A parametric model has been developed by TRW Systems for determining the performance of the flight model of the photo-imaging system (Reference 1). This model can also be used for analyzing the performance of the experimental photo-imaging system in the laboratory.

The method of analyzing the performance is based upon the theory developed by O. H. Shade, Sr. (Reference 6) to determine the resolving power of television camera systems, and the method defined by E. V. Soule (Reference 7) to estimate the performance of low-light-level imaging systems.

When Figure 41 is referred to, the target and background model is assumed to be in the form of a square-wave bar pattern of increasing spatial frequency with an average reflectance of $\bar{\rho}$ and a difference between target and background reflectance of $\Delta\rho$. The determination from Figure 42, of the S/N ratio at very low spatial frequencies, is based upon the apparent radiance and contrast of the target and background, the characteristics of the optical system, and the radiometric sensitivity and size of the individual elements of the photodiode array. Modulation transfer functions are then defined to determine the attenuating effects of image motion, the optical system resolution, and the detector size on the S/N ratio at high spatial frequencies. The high frequencies are then combined to obtain a modulation transfer function (MTF) defining the square-wave response of the imaging system. The S/N ratio at very low spatial frequencies, in combination with the square-wave MTF, then defines the S/N ratio at all spatial frequencies from zero to the resolution limit of the sensor.

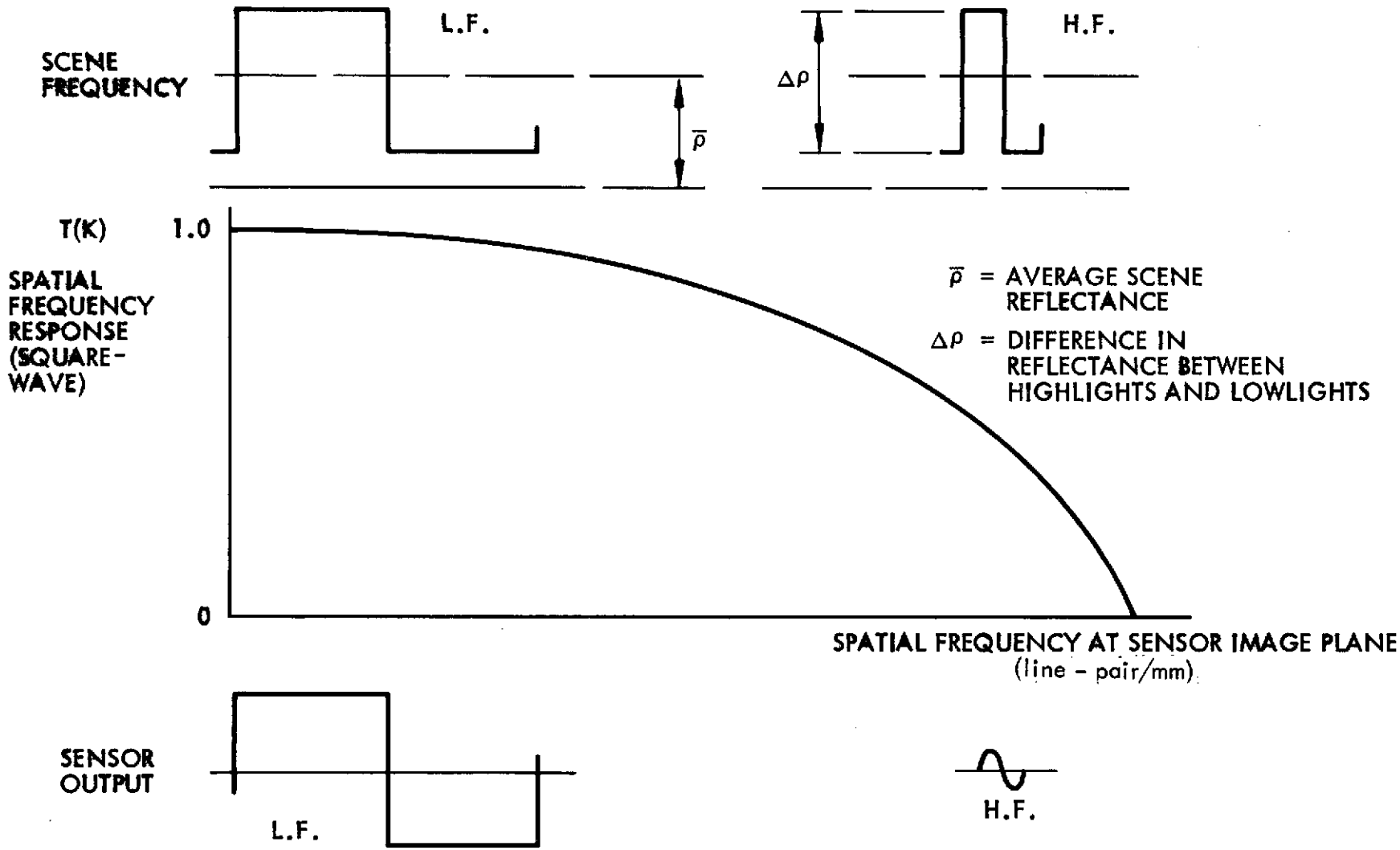

FIGURE 41. – SENSOR ANALYSIS USING MODULATION TRANSFER FUNCTIONS

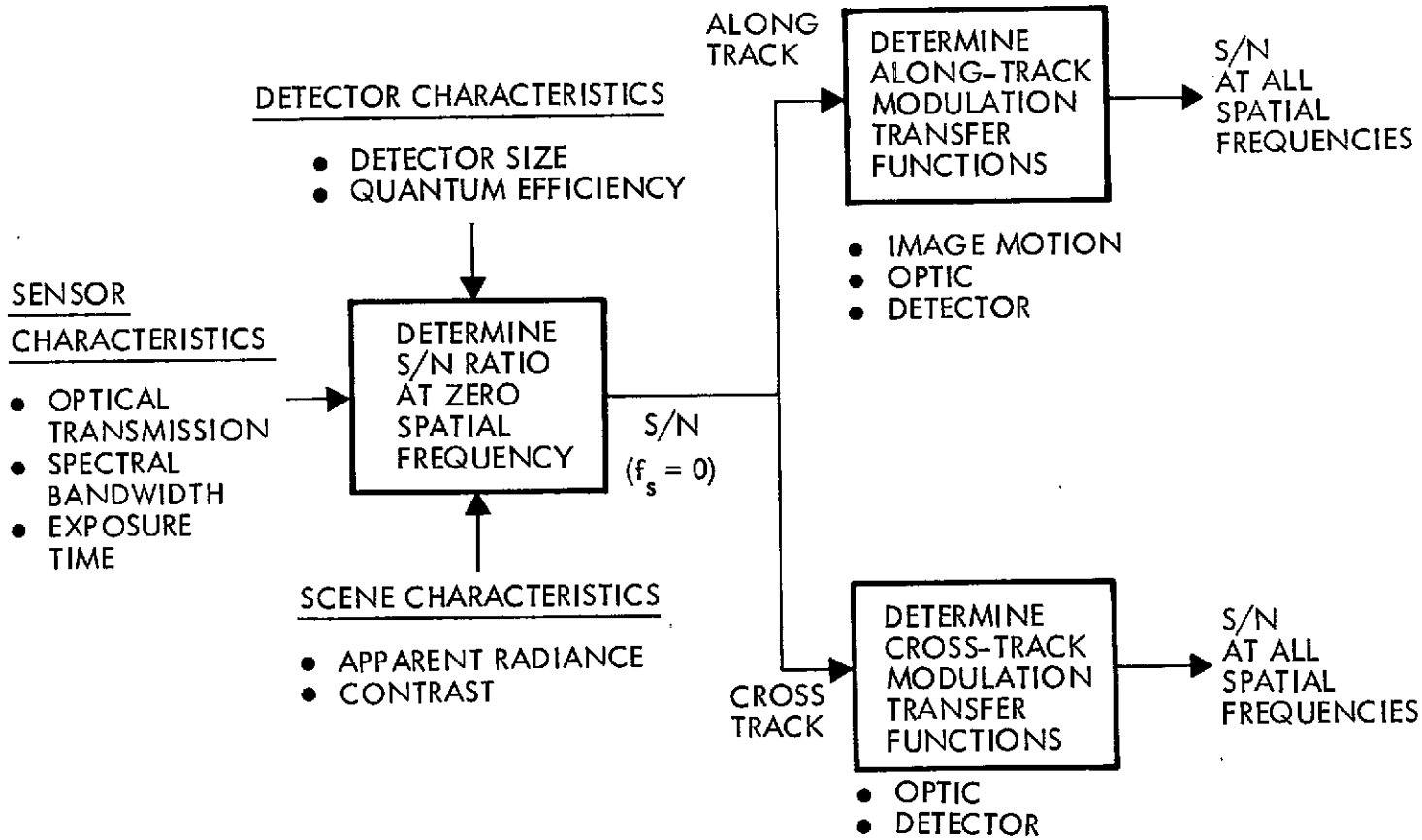

FIGURE 42. – METHOD OF ANALYSIS OF SENSOR PERFORMANCE

The phototransistor array operates in a four-step charge-discharge cycle as illustrated in Figure 43. Having been initially saturated after readout during the previous cycle, the photojunction is discharged. It is then recharged to a predetermined value prior to the light exposure interval. During the exposure interval, dark noise is induced primarily because of current leakage in the photojunction. Secondary components of dark noise are preamplifier thermal and shot noise, as well as capacitance sampling noise. Exposure to light causes a discharge of the junction, with additional noise being induced by the conversion of photons to photoelectrons. The last event in the cycle is that of restoring the charge on the photojunction to the initial value, with the amount of current required to accomplish restoration of charge comprising the signal.

The equations used to compute performance are defined in Table XV, with the variables and constants being defined in Table XVI.

The first equation is used to compute the number of photoelectrons generated during the exposure interval of the array, when a planet of known albedo irradiated by the sun at a specified solar distance and phase angle is observed with an optical system of specified f-number and optical transmission. The value computed corresponds to a dc level that, in turn, corresponds to the average value of solar irradiance and planet albedo.

The second equation is used to determine the amplitude of the ac signal by using a specified value of modulation contrast that corresponds to the modulation contained in the observed scene. Modulation contrast is defined as the difference between the maximum and minimum values of scene radiance divided by the sum of the two values.

The third equation is used to compute the equivalent number of photoelectrons corresponding to the dark noise level of the array that are converted to noise current during the readout interval. The symbol NES in the numerator of the first term corresponds to the noise equivalent signal (dark noise level) of the array, expressed in joules/meter^2 of solar radiation, within the wavelength range of 0.4 to 0.8 μm, an empirical test parameter defining the array noise level. When the value of NES is divided by the integration time of the array, the value is converted to watts/meter^2 (0.4 to 0.8 μm). The denominator of the first term corresponds to the number of watts in one solar constant within the 0.4 to 0.8 μm wavelength range. The second term is used to compute the

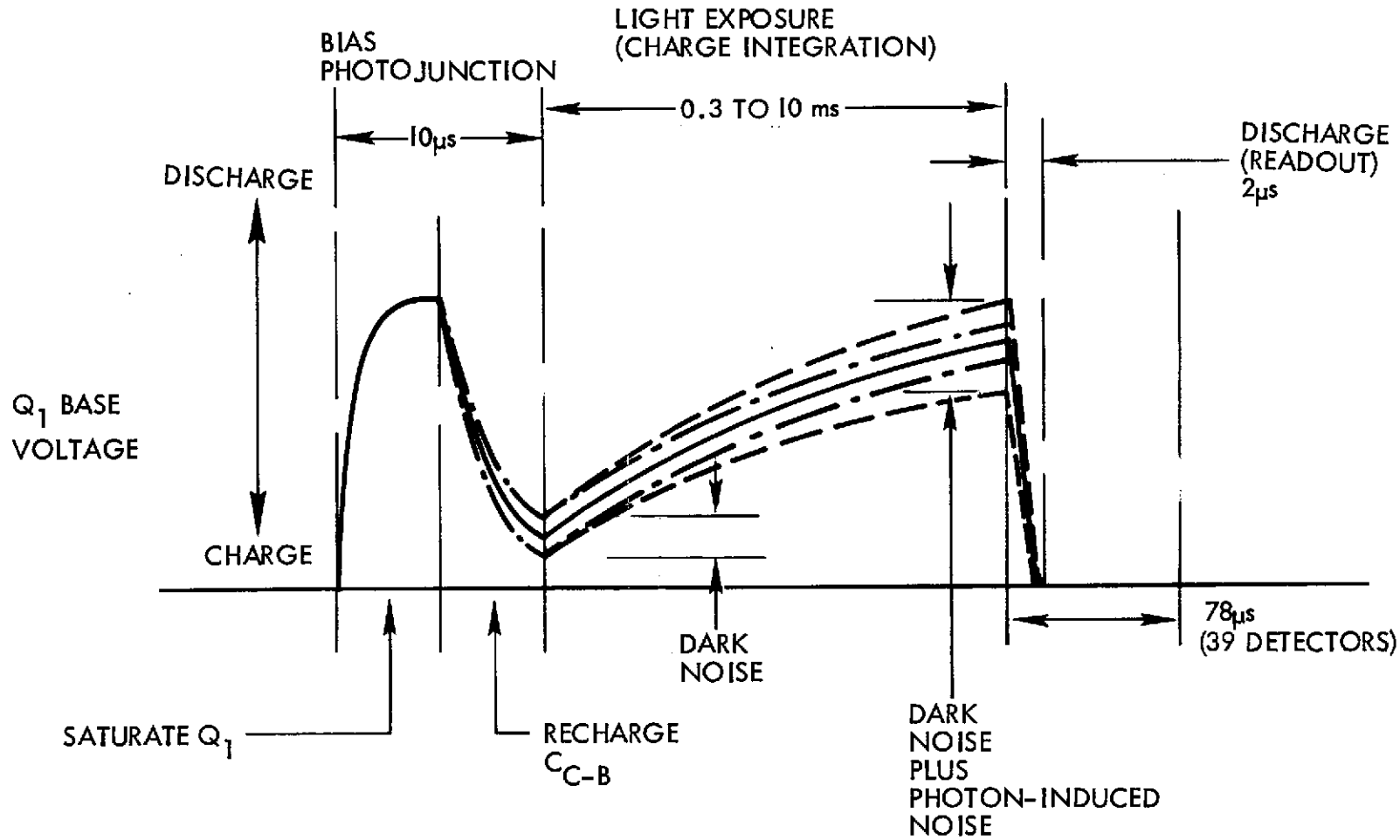

FIGURE 43. – PHOTOTRANSISTOR ARRAY CHARGE AND DISCHARGE CYCLE

TABLE XV. – PARAMETRIC EQUATIONS FOR CALCULATING PHOTO-IMAGING SYSTEM PERFORMANCE

PHOTOELECTRONS GENERATED DURING EXPOSURE INTERVAL

$$n_4 = \frac{a\, t_1\, t_2 \cos\beta}{4\, D_p^{\,2}\, f^2\, h\, c} \int_{0.4\mu m}^{1.1\mu m} H_\lambda\, \rho_\lambda\, \lambda\, \epsilon_\lambda\, d\lambda \qquad (1)$$

(photoelectrons, dc)

SIGNAL AMPLITUDE (PK-PK SQUARE WAVE)

$$S_4 = 2\, m_0\, n_4 \qquad (2)$$

(photoelectrons, ac)

PHOTOELECTRON EQUIVALENT OF NOISE EQUIVALENT SIGNAL (DARK NOISE)

$$n_2 = \frac{NES/t_1}{\int_{0.4\mu m}^{0.8\mu m} H_\lambda\, d\lambda} \times \frac{a\, t_1}{h\, c} \int_{0.4\mu m}^{0.8\mu m} H_\lambda\, \epsilon_\lambda\, \lambda\, d\lambda \qquad (3)$$

(photoelectrons, rms)

SIGNAL PROCESSING ELECTRONICS NOISE

$$n_5 = 0.5\, n_2 \qquad (4)$$

(electrons, rms)

QUANTIZATION NOISE

$$n_6 = \frac{n_2\, D}{E\, \sqrt{12}} \qquad (5)$$

(electrons, rms)

RSS VALUE, RANDOM NOISE COMPONENTS

$$n_7 = \left[n_4 + n_2^{\,2} + n_5^{\,2} \right]^{1/2} \qquad (6)$$

(electrons, rss)

RSS VALUE, RANDOM AND QUANTIZATION NOISE

$$n_8 = \left[n_6^{\,2} + 2.13 \frac{n_7^{\,3}}{n_6\, \sqrt{12}} \right]^{1/2} \quad \text{For } n_7 < 1.67\, n_6$$

$$n_8 = \left[n_6^{\,2} + n_7^{\,2} \right]^{1/2} \quad \text{For } n_7 > 1.67\, n_6 \qquad (7)$$

(electrons, rss)

SIGNAL-TO-NOISE RATIO DURING READOUT INTERVAL (AT ALL SPATIAL FREQUENCIES)

$$S_9 = \frac{S_4}{n_8}\, T(k) \qquad (8)$$

(pk-pk square wave/rss noise)

TABLE XVI. – DEFINITION AND VALUE OF VARIABLES AND CONSTANTS

Symbol	Description	Unit	Symbol for Unit	Value
n_4	Photoelectrons generated during exposure interval	photoelectrons dc	–	Variable
a	Area of detector element	square meter	m^2	4.12×10^{-10}
t_1	Exposure time	second	s	$0.405, 0.580, 1.101 \times 10^{-3}$
t_2	Optical transmission	percent	%	0.54
ϕ	Solar phase angle	radian	rad	$\pi/4$ (for analysis)
D_p	Solar distance	astronomical unit	AU	5.2, 9.5, 19.2
f	f-Number of optical system	–	–	1.23
h	Planck's constant	joule-second	J-s	6.624×10^{-34}
c	Velocity of light	micrometer per second	μm/s	3.0×10^{14}
H_λ	Spectral solar irradiance	watts per square meter-micrometer	W/m^2-μm	Variable
ρ_λ	Spectral albedo of planet or satellite	percent	%	Variable
λ	Wavelength	micrometer	μm	0.4 to 1.1
η_λ	Spectral quantum efficiency of photodetectors	photoelectrons per photon	–	See Text
S_4	Signal amplitude	photoelectrons, pk-pk square wave		Variable
m_0	Modulation contrast of planetary object	percent	%	1.0, 0.50, 0.25, 0.10, 0.05
n_2	Noise on collector-base junction at end of charge cycle	electrons, root-mean-square	electrons rms	Variable
NES	Dark noise level, noise equivalent energy density-6000°K radiation temperature (0.4 – 8μm)	joule per square meter	J/m^2	1.2×10^{-6}
D	Dynamic range of video signal above dark noise	–	–	10^3
n_5	Noise in signal processing electronics	electrons, root-mean-square	electrons rms	396
n_6	Quantization noise	electrons, root-mean-square	electrons rms	Variable
n_7	rss Value of random noise components	electrons, root-sum-square	electrons rss	Variable
n_8	rss Value of quantization noise and random noise	electrons, root-sum-square	electrons rss	Variable
S_9	Signal-to-noise ratio	current ratio	pk-pk square wave/ rss noise	Variable
T(k)	Response of sensor to square wave of increasing spatial frequency	percent	%	See Text

number of photoelectrons generated within an element of the array when irradiated by one solar constant within the 0.4 to 0.8 μm wavelength range. With a noise equivalent signal (NES) value of 1.2×10^{-6} J/m^2, the dark noise level is computed as 792 photoelectrons, rms, using an exposure time of 1 ms.

The additional noise generated by the signal processing electronics associated with the phototransistor array has been empirically determined as approximately one-half the value of the NES of the array. The electron equivalent for this term is computed in equation (4).

In the fifth equation, the standard deviation of noise due to signal encoding is determined from a dynamic range of D above the dark noise level, n_2, and an assumed value of E corresponding to the number of levels of video encoding (E has a value of 256 for 8-bit video encoding).

The sixth equation is used to obtain an rss value for all random noise components.

In the seventh equation, the rss value of the random noise components and the quantization noise is determined. This relationship gives a more precise value of the combined effect of these two noise sources than the more conventional method of obtaining the rss value of the two terms, and is based on a discussion of quantization of signals containing a relatively high level of noise presented in Reference 8.

The S/N ratio of the sensor is then calculated by using the last equation, in which the signal amplitude is divided by the rss value of all noise components, and is multiplied by the square-wave MTF, thus defining the S/N ratio at all spatial frequencies.

The MTFs associated with the photo-imaging system are defined in Table XVII. In the direction of spacecraft rotation, normal to the phototransistor array, three MTFs are of importance: those defining the effects of the optical system, the width of the array elements, and the image motion upon the spatial frequency response of the system.

For analysis, the use of a catadioptric optical system, similar to the Farrard catadioptric lens system No. 1, is assumed. This optic has a geometric speed of f/1.23, an effective speed of t/1.68, and a radial obscuration ratio of 50%. The MTF for an obscured optical system is defined by the functions

TABLE XVII. – SUMMARY OF MODULATION TRANSFER FUNCTIONS

MTF	Equation	Definition of Symbols	Value of MTF at 82.8, line-pair/mm	Spatial Frequency at which MTF = 0 line-pair/mm
1. MTFs Normal to Array				
a. Optical System (With 50% radial obscuration by secondary mirror)	$T(k) = (1-\eta^2)^{-1}[A + B + C]$ $A = f(k, k_\ell)$ $B = f(\eta, k, k_\ell)$ $C = f(\eta, k, k_\ell)$	η = radial obscuration ratio k = spatial frequency k_ℓ = limiting spatial frequency See Reference 8 for details of equations	0.85	500
b. Width of detector element	Empirical data from Figure 6	N/A	0.31	58
c. Image motion during exposure interval	$T(k) = \frac{\sin \pi a k}{\pi a k}$	a = 0.015 mm (0.15 mrad) k = spatial frequency, lpm	0.64	66
d. System sine-wave MTF	a x b x c	–	0.17	55
e. System square-wave MTF	1a x 1b x 1c	–	0.22	55
2. MTFs Parallel to Array				
a. Optical system	Same as Item 1a	Same as Item 1a	0.85	500
b. Length of detector element	Empirical data from Figure 6	N/A	0.34	50
c. System sine-wave MTF	2a x 2b	–	0.29	50
d. System square-wave MTF	–	–	0.37	50

pecified in the table from Reference 9. The theoretical value of limiting patial frequency, at which the MTF is zero, assuming a diffraction-limited ptic at a wavelength of 0.6 μm is 1355 line-pair/mm (lpm). Manufacturer's ata defines a limiting spatial frequency of 700 to 800 lpm at the center of the eld of view and 100 lpm at the edge of the field of view. The field of view of iis optic is 9 deg; in this application, only 3.35 deg of this field is used. For nalysis, a limiting spatial frequency of 500 lpm is assumed.

The MTF of the phototransistor array, in the direction normal to the rray, is obtained from Figure 27.

The effect of image motion during the exposure interval is defined by an ITF of the form (sin x)/x and, assuming that the motion is equivalent to .15 mrad (0.15 mm at the image plane) during an exposure interval, the miting spatial frequency will be 66 lpm.

The sinusoidal MTF of the photo-imaging system in the direction normal o the array is the product of the above three MTFs, and is illustrated by urve (4) of Figure 44.

In the direction parallel to the phototransistor array, the MTFs are efined in Table XVII, and consist of the MTF of the optical system and the ITF defining the effect of the linear size of the detector elements parallel to ie array. Values of the latter are obtained from Figure 27. The sinusoidal ITF of the photo-imaging system parallel to the array is defined by curve (3) i Figure 45.

The equivalent square-wave MTFs of the photo-imaging system are illus-rated in Figure 46, having values larger by a factor of 4/pi than the sinusoidal ITFs from spatial frequencies between 1/5 of the cutoff frequency to the cutoff requency (Reference 10).

Note that the MTF normal to the array is lower than that parallel to the rray because of the effect of image motion during the exposure interval. The ormer has a value of 0.22 at the Nyquist frequency of 32.8 lpm (where sampling ccurs at two samples per cycle), whereas the latter has a value of 0.37 at this requency.

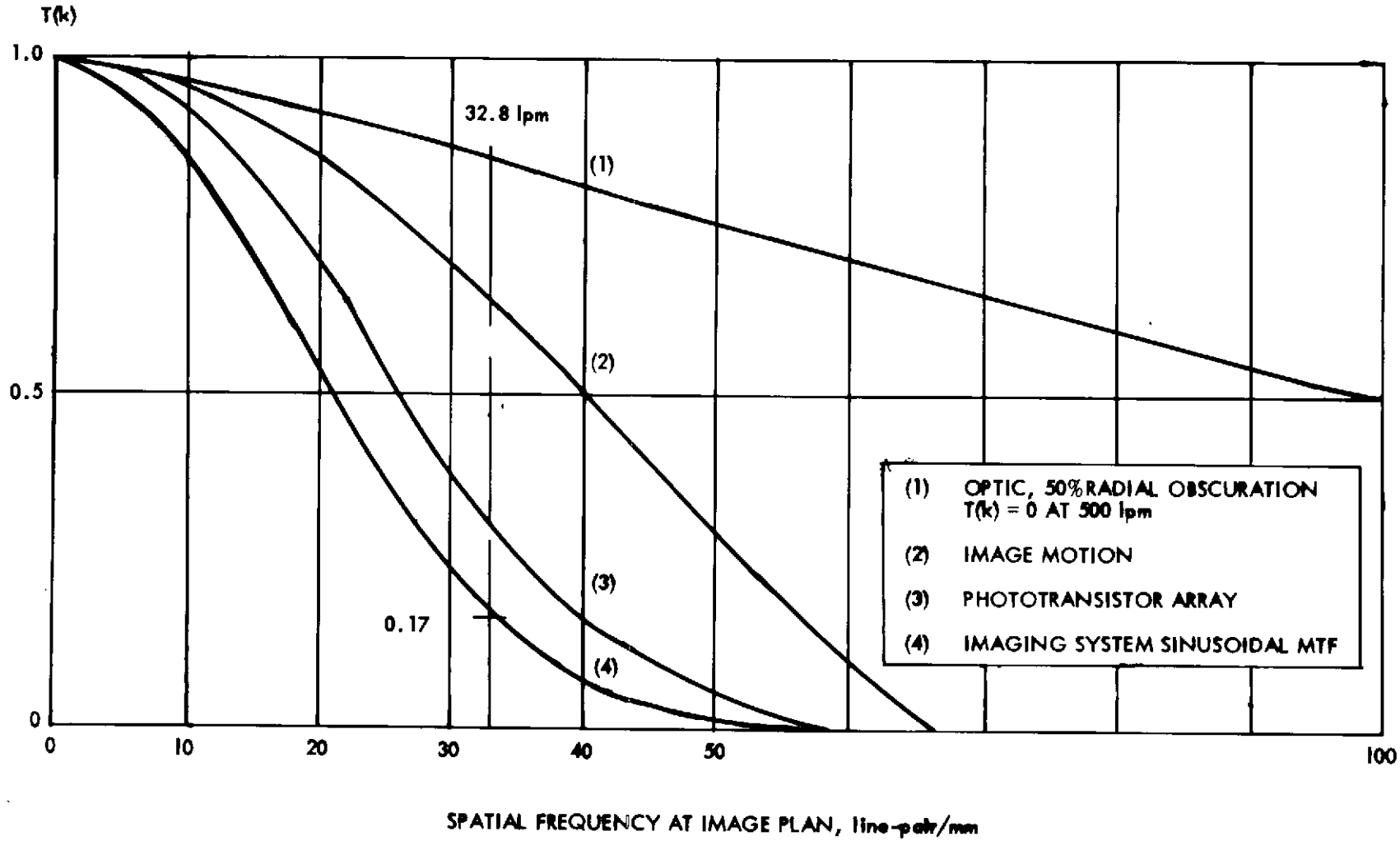

FIGURE 44. – MODULATION TRANSFER FUNCTIONS NORMAL TO ARRAY

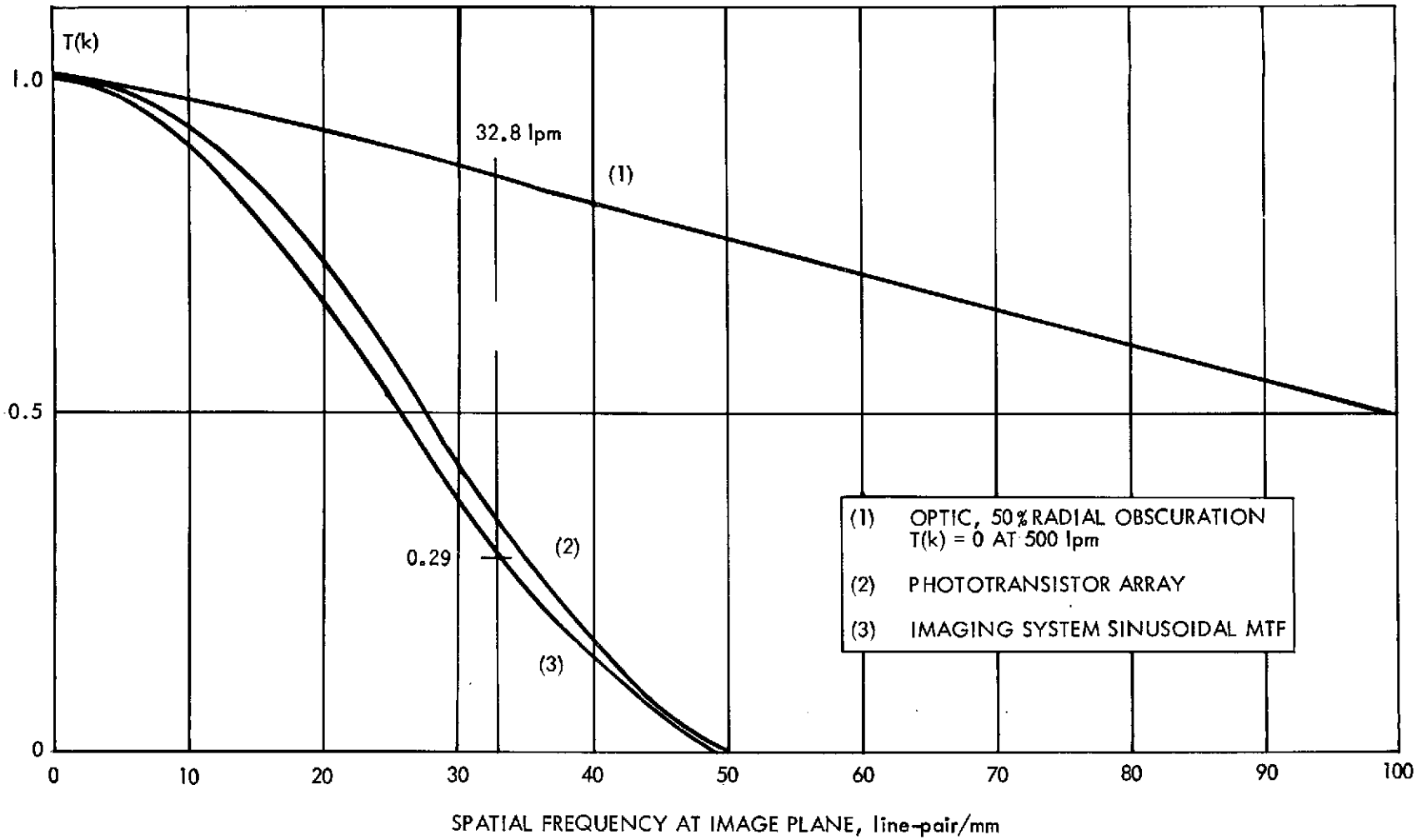

FIGURE 45. – MODULATION TRANSFER FUNCTIONS PARALLEL TO ARRAY

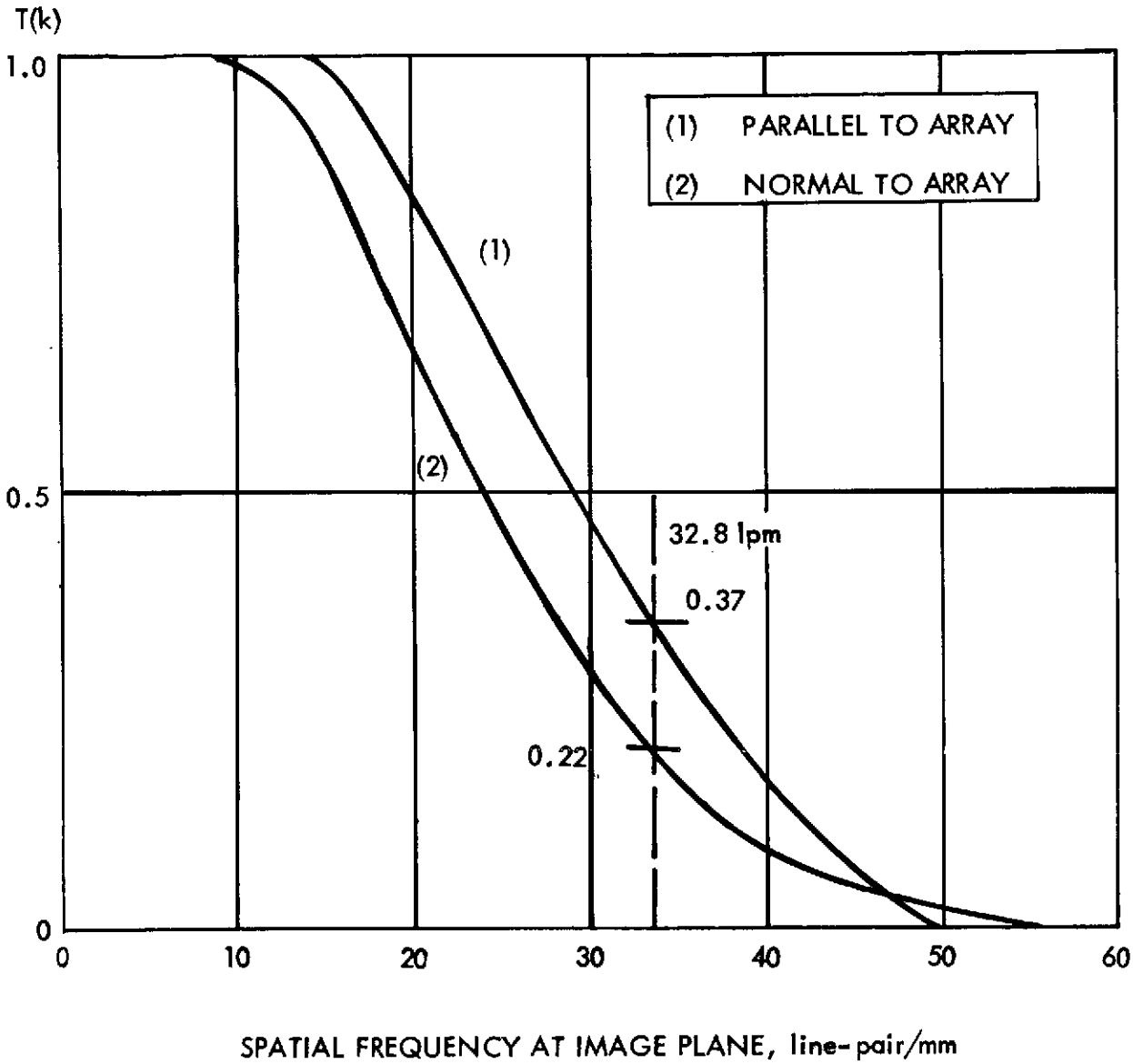

FIGURE 46. – IMAGING SYSTEM SQUARE-WAVE MODULATION TRANSFER FUNCTIONS

The previous discussion has been directed toward determination of the quare-wave MTFs of the flight model of the photo-imaging system, normal nd parallel to the phototransistor array. Although nearly identical with the light model, the square-wave MTFs of the experimental photo-imaging system n the laboratory will be slightly different because of a slight difference in the ine-wave response function of the optical system.

For the flight model, the sinusoidal response of the optic was assumed o be 0.85 at 32.8 lpm. The optic of the experimental laboratory system has measured MTF of 0.90 (tangential) and 0.83 (radial) at the edges of the -deg FOV.

In further analysis, the MTFs of the flight model and the experimental hoto-imaging systems are assumed to be equal.

7.2.2
Performance Analysis of Flight Model of Photo-Imaging System

With the use of the parametric equations developed in the previous section, he performance of the flight model of the photo-imaging system has been deter-nined. To perform these calculations, a computer program was developed hat computes values of the S/N ratio at two spatial frequencies, zero and 2.8 lpm. The latter corresponds to the Nyquist, or sampling frequency, and orresponds to the IFOV of one detector element (0.15 mrad). The S/N ratios re computed at these two spatial frequencies for five levels of scene modula-ion contrast – 100%, 50%, 25%, 10%, and 5% for the six planets and satellites onsidered in the study: Jupiter, Io, Europa, Saturn, Titan, and Uranus. By arying the exposure time, values of S/N ratio at various spacecraft spin rates an be determined.

In Appendix B, a complete printout of the computations is presented for hree spacecraft spin rates: 5 rpm, 3.5 rpm, and 2 rpm, using sensor xposure times of 0.405 ms, 0.580 ms, and 1.01 ms, which correspond to an FOV of 0.15 mrad at a cone angle of 135 deg.

For the baseline configuration of the system, a spacecraft spin rate of rpm is proposed at Jupiter, Io, and Europa, and a spin rate of 2 rpm is pro-osed at Saturn, Titan, and Uranus. The performance at these planets with nese spin rates is presented in Tables XVIII and XIX (from Appendix B).

7.2.3
Performance Analysis of Experimental (Laboratory) Model of Photo-Imaging System

With the use of the parametric equations developed in Section 7.2.1, the erformance of the experimental model of the photo-imaging system has been letermined. As previously discussed, an approximation has been assumed in nodeling the spectral response by using a "square" spectral passband with 35% esponse over the wavelength range of 0.5 to 0.6 μm. An f-number of 4.4 is ssumed, corresponding to the effective value of the f-number of the experimental system in the laboratory tests.

The purpose of these computations is to determine the factors by which he radiance of the planets would have to be increased to obtain performance rom the experimental model that would be equivalent to that of the flight model. n computing these factors, it is assumed that the spectral characteristics of he planet radiance are unchanged. The spectral radiance will be that of solar rradiance modified by the spectral albedo of the planets. To perform the computations, a computer program was developed, similar to the program used in Section 7.2.2 for determining the performance of the flight model, with the ollowing modifications.

a. The exposure time is 4.8 ms rather than 0.40, 0.58, or 1.01 ms

b. The dynamic range of the electronics is 500, rather than 1000

c. The effective f-number of the optic is 4.4, rather than 1.23. This is the effective focal ratio of an f/4.0 optical system, with a 100-cm (4-in.) focal length, with the test pattern at a conjugate distance of 100 cm (4 in.).

d. The optical transmission is 35%, rather than 50%

e. The spectral bandwidth is 0.1μ, rather than 0.7μ

f. The radiance of the test pattern (planetary image) is computed in absolute units by computing the radiance of the planet under consideration, and by multiplying this value by a factor corresponding to the increase in radiance level desired in laboratory tests.

The results obtained with this program are presented in Appendix C. In Run 1 of this appendix, the S/N ratios of the experimental photo-imaging system observing test patterns simulating imagery of Jupiter, Io, Europa, Saturn, Titan,

TABLE XVIII. – PERFORMANCE OF FLIGHT MODEL OF PHOTO-IMAGING SYSTEM OBSERVING JUPITER, IO, AND EUROPA (SPACECRAFT SPIN RATE = 5 rpm)

THE OPTICS HAVE AN F/# OF 1.23 AND TRANS OF .54
AND THE INTEGRATION TIME IS .405 M-SEC

DARK NOISE, PHOTOELECTRONS RMS = 789.29411

THIS CASE CONSIDERS JUPITER WITH ALBEDO AT 0.525 U OF .51
WITH 5.2AU SOLAR DISTANCE AND .785RAD PHASE ANGLE

MODULATION CONTRAST	REFLECT DIFFERENCE	PK-PK SIGNAL PHOTOELECTRONS	RMS NOISE	S/N RATIO (PK-PK/RSS) AT 0 LPM	AT 32.8 LPM
1.000	1.020	441774	1218	363	80
.500	.510	220887	1218	181	40
.250	.255	110443	1218	91	20
.100	.102	44177	1218	36	8
.050	.051	22089	1218	18	4

QUANTIZATION NOISE,PHOTOELECTRONS RMS= 890.03743

THIS CASE CONSIDERS IO WITH ALBEDO AT 0.525 U OF .92
WITH 5.2AU SOLAR DISTANCE AND .785RAD PHASE ANGLE

MODULATION CONTRAST	REFLECT DIFFERENCE	PK-PK SIGNAL PHOTOELECTRONS	RMS NOISE	S/N RATIO (PK-PK/RSS) AT 0 LPM	AT 32.8 LPM
1.000	1.840	859312	1308	657	145
.500	.920	429656	1308	329	72
.250	.460	214828	1308	164	36
.100	.184	85931	1308	66	14
.050	.092	42966	1308	33	7

QUANTIZATION NOISE,PHOTOELECTRONS RMS= 890.03743

THIS CASE CONSIDERS EUROPA WITH ALBEDO AT 0.525 U OF .85
WITH 5.2AU SOLAR DISTANCE AND .785RAD PHASE ANGLE

MODULATION CONTRAST	REFLECT DIFFERENCE	PK-PK SIGNAL PHOTOELECTRONS	RMS NOISE	S/N RATIO (PK-PK/RSS) AT 0 LPM	AT 32.8 LPM
1.000	1.700	793929	1293	614	135
.500	.850	396965	1293	307	68
.250	.425	198482	1293	153	34
.100	.170	79393	1293	61	14
.050	.085	39696	1293	31	7

QUANTIZATION NOISE,PHOTOELECTRONS RMS= 890.03743

TABLE XIX. — PERFORMANCE OF FLIGHT MODEL OF PHOTO-IMAGING SYSTEM OBSERVING SATURN, TITAN, AND URANUS
(SPACECRAFT SPIN RATE = 2 rpm)

THE OPTICS HAVE AN F/# OF 1.23 AND TRANS OF .54
AND THE INTEGRATION TIME IS 1.010 M-SEC

DARK NOISE, PHOTOELECTRONS RMS = 789.29411

THIS CASE CONSIDERS SATURN WITH ALBEDO AT 0.525 U OF .44
WITH 9.5AU SOLAR DISTANCE AND .785RAD PHASE ANGLE

MODULATION CONTRAST	REFLECT DIFFERENCE	PK-PK SIGNAL PHOTOELECTRONS	RMS NOISE	S/N RATIO (PK-PK/RSS) AT 0 LPM	AT 32.8 LPM
1.000	.880	277507	1183	235	52
.500	.440	138753	1183	117	26
.250	.220	69377	1183	59	13
.100	.088	27751	1183	23	5
.050	.044	13875	1183	12	3

QUANTIZATION NOISE,PHOTOELECTRONS RMS= 890.03743

THIS CASE CONSIDERS TITAN WITH ALBEDO AT 0.525 U OF .34
WITH 9.5AU SOLAR DISTANCE AND .785RAD PHASE ANGLE

MODULATION CONTRAST	REFLECT DIFFERENCE	PK-PK SIGNAL PHOTOELECTRONS	RMS NOISE	S/N RATIO (PK-PK/RSS) AT 0 LPM	AT 32.8 LPM
1.000	.680	235298	1174	200	44
.500	.340	117649	1174	100	22
.250	.170	58824	1174	50	11
.100	.068	23530	1174	20	4
.050	.034	11765	1174	10	2

QUANTIZATION NOISE,PHOTOELECTRONS RMS= 890.03743

THIS CASE CONSIDERS URANUS WITH ALBEDO AT 0.525 U OF .55
WITH19.2AU SOLAR DISTANCE AND .785RAD PHASE ANGLE

MODULATION CONTRAST	REFLECT DIFFERENCE	PK-PK SIGNAL PHOTOELECTRONS	RMS NOISE	S/N RATIO (PK-PK/RSS) AT 0 LPM	AT 32.8 LPM
1.000	1.100	60926	1138	54	12
.500	.550	30463	1138	27	6
.250	.275	15231	1138	13	3
.100	.110	6093	1138	5	1
.050	.055	3046	1138	3	1

QUANTIZATION NOISE,PHOTOELECTRONS RMS= 890.03743

nd Uranus are presented, using values of test pattern radiance equivalent to hose of the planets and satellites. Comparing these results with those in ppendix B, which define the performance of the space-borne system, the S/N atios are considerably lower than those of the space-borne system, indicating hat higher levels of test pattern radiance will be required to obtain equivalent erformance.

In Run 2 of the appendix, the radiance levels of the test patterns are ncreased by a factor of 4.5 above the true radiance levels of Jupiter, Io, and Europa.

In Run 3, the radiance levels of the test patterns are increased by a ictor of 11 above the true radiance levels of Saturn, Titan, and Uranus.

The results of runs 2 and 3, presented in Tables XX and XXI correspond losely to the performance of the flight model of the photo-imaging system at pacecraft spin rates of 5 and 2 rpm, respectively. These results will be ompared in detail in the following paragraphs.

Summary of Results of Computations

Summarizing the results of the previous computation, Table XVIII, from ata computed in Appendix B, defines the performance of the flight model of he photo-imaging system when the system observes Jupiter, Io, and Europa ith a spacecraft spin rate of 5 rpm, an exposure time of 0.405 ms, and a cone ngle of 135 deg. Table XX, from data computed in Appendix C, defines the erformance of the experimental photo-imaging system when observing test atterns simulating the same planets and satellites, and using an exposure ime of 4.8 ms, with test pattern radiance higher than the true radiance of the lanets by a factor of 4.5. Comparing data from the two tables, the S/N ratios re equivalent within 3% for Jupiter and 11% for Io and Europa.

Similarly, Table XIX, from data computed in Appendix B, defines the erformance of the flight model when Saturn, Titan, and Uranus are observed ith a spacecraft spin rate of 2 rpm, an exposure time of 1.01 ms, and a cone ngle of 135 deg. Table XXI, from data computed in Appendix C, defines the erformance of the experimental system when observing test patterns simulating

TABLE XX. – PERFORMANCE OF EXPERIMENTAL PHOTO-IMAGING SYSTEM OBSERVING JUPITER, IO, AND EUROPA WITH APPARENT PLANET RADIANCE INCREASED BY A FACTOR OF 4.5

THE OPTICS HAVE AN F/# OF 4.40 AND TRANS OF .35
AND THE INTEGRATION TIME IS 4.800 M-SEC

DARK NOISE, PHOTOELECTRONS RMS = 789.29411

THIS CASE CONSIDERS JUPITER WITH ALBEDO AT 0.525U OF .51
WITH 5.2AU SOLAR DISTANCE AND .785RAD PHASE ANGLE

MODULATION CONTRAST	REFLECT DIFFERENCE	PK-PK SIGNAL PHOTOELECTRONS	RMS NOISE	S/N RATIO (PK-PK/RSS) AT 0 LPM	AT 32.8 LPM
1.000	1.020	383119	1081	354	78
.500	.510	191560	1081	177	39
.250	.255	95780	1081	89	19
.100	.102	38312	1081	35	8
.050	.051	19156	1081	18	4

QUANTIZATION NOISE,PHOTOELECTRONS RMS= 445.01872
PLANET IRRADIANCE INCREASED BY FACTOR OF 4.5
OBJECT RADIANCE, W/SQ.METER-STER(0.5-0.6U)= 3.834

THIS CASE CONSIDERS IO WITH ALBEDO AT 0.525U OF .92
WITH 5.2AU SOLAR DISTANCE AND .785RAD PHASE ANGLE

MODULATION CONTRAST	REFLECT DIFFERENCE	PK-PK SIGNAL PHOTOELECTRONS	RMS NOISE	S/N RATIO (PK-PK/RSS) AT 0 LPM	AT 32.8 LPM
1.000	1.840	665558	1144	582	128
.500	.920	332779	1144	291	64
.250	.460	166390	1144	145	32
.100	.184	66556	1144	58	13
.050	.092	33278	1144	29	6

QUANTIZATION NOISE,PHOTOELECTRONS RMS= 445.01872
PLANET IRRADIANCE INCREASED BY FACTOR OF 4.5
OBJECT RADIANCE, W/SQ.METER-STER(0.5-0.6U)= 6.654

THIS CASE CONSIDERS EUROPA WITH ALBEDO AT 0.525U OF .85
WITH 5.2AU SOLAR DISTANCE AND .785RAD PHASE ANGLE

MODULATION CONTRAST	REFLECT DIFFERENCE	PK-PK SIGNAL PHOTOELECTRONS	RMS NOISE	S/N RATIO (PK-PK/RSS) AT 0 LPM	AT 32.8 LPM
1.000	1.700	614918	1133	543	119
.500	.850	307459	1133	271	60
.250	.425	153729	1133	136	30
.100	.170	61492	1133	54	12
.050	.085	30746	1133	27	6

QUANTIZATION NOISE,PHOTOELECTRONS RMS= 445.01872
PLANET IRRADIANCE INCREASED BY FACTOR OF 4.5
OBJECT RADIANCE, W/SQ.METER-STER(0.5-0.6U)= 6.148

TABLE XXI. – PERFORMANCE OF EXPERIMENTAL PHOTO-IMAGING SYSTEM OBSERVING SATURN, TITAN, AND URANUS WITH APPARENT PLANET RADIANCE INCREASED BY A FACTOR OF 11

THE OPTICS HAVE AN F/# OF 4.40 AND TRANS OF .35
AND THE INTEGRATION TIME IS 4.800 M-SEC

DARK NOISE, PHOTOELECTRONS RMS = 789.29411

THIS CASE CONSIDERS SATURN WITH ALBEDO AT 0.525U OF .44
WITH 9.5AU SOLAR DISTANCE AND .785RAD PHASE ANGLE

MODULATION CONTRAST	REFLECT DIFFERENCE	PK-PK SIGNAL PHOTOELECTRONS	RMS NOISE	S/N RATIO (PK-PK/RSS) AT 0 LPM	AT 32.8 LPM
1.000	.880	241465	1048	230	51
.500	.440	120733	1048	115	25
.250	.220	60366	1048	58	13
.100	.088	24147	1048	23	5
.050	.044	12073	1048	12	3

QUANTIZATION NOISE,PHOTOELECTRONS RMS= 445.01872
PLANET IRRADIANCE INCREASED BY FACTOR OF 11
OBJECT RADIANCE, W/SQ.METER-STER(0.5-0.6U)= 2.416

THIS CASE CONSIDERS TITAN WITH ALBEDO AT 0.525U OF .34
WITH 9.5AU SOLAR DISTANCE AND .785RAD PHASE ANGLE

MODULATION CONTRAST	REFLECT DIFFERENCE	PK-PK SIGNAL PHOTOELECTRONS	RMS NOISE	S/N RATIO (PK-PK/RSS) AT 0 LPM	AT 32.8 LPM
1.000	.680	178635	1033	173	38
.500	.340	89318	1033	87	19
.250	.170	44659	1033	43	10
.100	.068	17864	1033	17	4
.050	.034	8932	1033	9	2

QUANTIZATION NOISE,PHOTOELECTRONS RMS= 445.01872
PLANET IRRADIANCE INCREASED BY FACTOR OF 11
OBJECT RADIANCE, W/SQ.METER-STER(0.5-0.6U)= 1.786

THIS CASE CONSIDERS URANUS WITH ALBEDO AT 0.525U OF .55
WITH19.2AU SOLAR DISTANCE AND .785RAD PHASE ANGLE

MODULATION CONTRAST	REFLECT DIFFERENCE	PK-PK SIGNAL PHOTOELECTRONS	RMS NOISE	S/N RATIO (PK-PK/RSS) AT 0 LPM	AT 32.8 LPM
1.000	1.100	60863	1004	61	13
.500	.550	30431	1004	30	7
.250	.275	15216	1004	15	3
.100	.110	6086	1004	6	1
.050	.055	3043	1004	3	1

QUANTIZATION NOISE,PHOTOELECTRONS RMS= 445.01872
PLANET IRRADIANCE INCREASED BY FACTOR OF 11
OBJECT RADIANCE, W/SQ.METER-STER(0.5-0.6U)= .606

hese planets and satellites, with an exposure time of 4.8 ms, and a test
attern radiance higher than the true radiance of the planets by a factor of 11.
Comparing data from the two tables, the S/N ratios are equivalent within 2%
or Saturn, 13% for Titan, and 11% for Uranus.

In summary, using the simplified model of the experimental photo-
maging system for simulating observations of Jupiter, Io, and Europa with a
pacecraft spin rate of 5 rpm, an increase in the test pattern radiance levels
n the laboratory by a factor of 4.5 above the true planetary radiance levels will
esult in performance equivalent to the flight model.

For simulating observations of Saturn, Titan, and Uranus with a space-
craft spin rate of 2 rpm, an increase in the test pattern radiance levels in the
aboratory by a factor of 11 above the true planetary radiance levels will result
n performance equivalent to the flight model.

A summary of the true radiance values of the planets and satellites, and
he increased values required to obtain performance equivalent to the flight
model with the experimental model of the photo-imaging system, is contained
n Table XXII.

The third step in establishing the test pattern radiance levels will be to
correct these computed values for (a) the use of incandescent illumination in
he test pattern illuminator, (b) the true spectral response of the experimental
system, and (c) the effective f-number of the optical system, using finite con-
ugate distances in the laboratory. Corrections for these factors will be
computed in the following section.

7.2.4
Correction of Test Pattern Radiance Levels for Incandescent Illumination and True Spectral Response of Experimental Photo-Imaging System

First, the performance of the flight model of the photo-imaging system has
een analyzed (Figure 40) with the system operating in a broad-band spectral
mode, with response from 0.4 to 1.1 μm, and observing planets with a radia-
ion temperature approximating 6000°K (solar irradiance modified by the
spectral albedo of the planets).

TABLE XXII. – INCREASE IN APPARENT RADIANCE OF PLANETS REQUIRED TO SIMULATE FLIGHT MODEL PERFORMANCE WITH EXPERIMENTAL PHOTO-IMAGING SYSTEM

	Jupiter	Io	Europa	Saturn	Titan	Uranus
True Planet Radiance W/m^2-sr (0.5-0.6μm) (~6000°K)	0.852	1.479	1.366	0.220	0.162	0.055
Spacecraft Spin Rate, rpm	5	5	5	2	2	2
Ratio, Test Pattern Radiance to True Planet Radiance	4.5	4.5	4.5	11	11	11
Test Pattern Radiance Required for Equivalent Performance in Laboratory W/m^2-sr (0.5-0.6μm) (~6000°K)	3.834	6.654	6.148	2.416	1.786	0.606

Second, a simplified analytical model was assumed for the experimental hoto-imaging system to be used in laboratory feasibility tests, with the spectral andpass being approximated by a uniform, or "square", response from 0.5 to 6 μm, and an effective f-number of 4.4. The increase in the apparent planetary radiance level was computed for this system to obtain S/N ratios equivalent o the flight model, assuming that the apparent planetary radiation temperature emained unchanged. These increased values of radiance were summarized in able XXII.

The third step in determining the radiance levels for use in laboratory ests is to correct the values for the use of incandescent illumination of 2650°K adiation temperature in the test pattern illuminator and for the true spectral esponse of the experimental system.

The spectral irradiance of the test pattern illuminator is shown in able XI and is illustrated in Figure 33. The measured spectral response of he optical system of the experimental photo-imaging system is presented in igure 35.

The equations for determining the values of incandescent radiance for the aboratory program are defined in Table XXIII. The symbols used in the equaons are specified in Section 3.0. Equation (1) of the Table XXIII is used to ompute the number of photoelectrons generated within one element of the hototransistor array per unit of planet irradiance, with the radiation temperare of the solar irradiance (6000°K), modified by the spectral albedo of the lanet. The numerator of this equation is used for computation of the number f photoelectrons generated within one element of the phototransistor array hen observing a planet illuminated by solar irradiance, H_λ, with the spectral lbedo of the planet being ρ_λ. The spectral response of the system is assumed o be that of the simplified analytical model defined in Section 7.2.3, 0.35 etween 0.5 and 0.6 μm. The denominator of the equation is used to compute he integrated solar irradiance on the planet, modified by the spectral albedo, $_\lambda$. Thus the quotient of these two terms determines the normalized, or per nit value, of the number of photoelectrons generated within one detector lement by one unit of planet irradiance, with the irradiance being modified by he spectral albedo corresponding to the individual planet.

TABLE XXIII. – COMPUTATION OF SCALE FACTOR TO ACCOUNT FOR SPECTRAL RESPONSE OF EXPERIMENTAL PHOTO-IMAGING SYSTEM AND USE OF INCANDESCENT ILLUMINATION

PHOTOELECTRONS GENERATED IN PHOTODETECTOR ELEMENT PER UNIT OF PLANET IRRADIANCE

$$n_1 = \frac{\frac{a\,t_1}{4\,f_1^2\,h\,c}\int_{0.5\mu m}^{0.6\mu m} H_\lambda\,\rho_\lambda\,t_2\,\epsilon_\lambda\,\lambda\,d\lambda}{\int_{0.5\mu m}^{0.6\mu m} H_\lambda\,\rho_\lambda\,d\lambda} \qquad (1)$$

PHOTOELECTRONS GENERATED IN PHOTODETECTOR ELEMENT PER UNIT OF ILLUMINATOR IRRADIANCE

$$n_9 = \frac{\frac{a\,t_1}{4\,f_1^2\,h\,c}\int_{0.5\mu m}^{0.7\mu m} S_\lambda\,t_\lambda\,\epsilon_\lambda\,\lambda\,d\lambda}{\int_{0.5\mu m}^{0.7\mu m} S_\lambda\,d\lambda} \qquad (2)$$

SCALE FACTOR – RATIO OF ILLUMINATOR RADIANCE TO PLANET RADIANCE TO GENERATE EQUIVALENT NUMBER OF PHOTOELECTRONS

$$R = \frac{n_1}{n_9} \qquad (3)$$

Equation (2) of the Table XXIII is used, in a similar manner, to compute the number of photoelectrons generated within one detector element of the array of the experimental photo-imaging system in the laboratory per unit of illuminator irradiance. The numerator is used to determine the number of photoelectrons generated when observing the test pattern illuminator, of 2650°K radiation temperature, with values of spectral radiance, S_λ, from Table XI. The spectral response, t_λ, is the true spectral response of the system, covering the wavelength range from 0.5 to 0.7 μm from Figure 35. The denominator is used to determine the integrated irradiance of the test pattern illuminator over the spectral range of 0.5 to 0.7 μm. The quotient of these two terms determines the normalized value, or value per unit, of the number of photoelectrons generated within one detector element by one unit of illuminator irradiance.

In equation (3) of the Table XXIII, the ratio R, or scale factor, is computed by taking the ratio of the values computed in equations (1) and (2). This scale factor represents the factor by which the illuminator irradiance (of 2650°K radiation temperature) must be increased to be equivalent to a specified value of planetary irradiance (of 6000°K radiation temperature, modified by the albedo of the individual planet. Values of the scale factor, R, were computed for the six planets and satellites considered in this study, using the computer program presented in Appendix D. These values are listed in row 2 of Table XXIV.

Note that these scale factors are identical for Jupiter and Saturn, but a slightly different value was obtained for the planet Uranus. This can be explained by referring to the plots of planetary albedo in Figure 1 and to the plot of the spectral quantum efficiency of the photodetectors in Figure 25. Over the narrow spectral range of 0.5 to 0.6 μm, the quantum efficiency of the detectors is relatively constant and the slope of the albedo plots results in a negligible difference in the scale factor R, as this scale factor is based upon the computation of photoelectrons generated per unit of planet irradiance, a normalized value. The identical values of the scale factors for the satellites Io, Europa, and Titan, can be explained because the values of spectral albedo are not available in the literature and uniform values over the spectral range were assumed.

TABLE XXIV. – VALUES OF INCANDESCENT TEST PATTERN RADIANCE FOR USE IN LABORATORY TESTS

Test Item	Planets and Satellites					
	Jupiter	Io	Europa	Saturn	Titan	Uranus
Test Pattern Radiance Radiance W/m^2-sr (0.5 - 0.6μm) (6000°K)	3.834	6.654	6.148	2.416	1.786	0.606
Scale Factor For Use Of Incandescent Illumination	2.363	2.363	2.363	2.363	2.363	2.365
Incandescent Test Pattern Radiance Required W/m^2-sr (0.5 - 0.7μm) (2650°K)	9.060	15.723	19.528	5.709	4.220	1.933

In row 1 of Table XXIV, the values of apparent planet radiance previously presented in Table XXII are listed. These are the radiance levels required to obtain performance of the simplified analytical model of the experimental photo-imaging system (Section 7.2.3) equivalent to that of the flight model (Section 7.2.2). Multiplying these values by the scale factors in row 2 results in obtaining the equivalent radiance values for use in the laboratory feasibility tests, using incandescent radiation of 2650°K radiation temperature. These values are listed in row 3 of the table.

Integrated irradiance of illuminator. – An additional computation is of value in establishing the laboratory test conditions. The total irradiance (and radiance) of the illuminator over the spectral range of the experimental photo-imaging system (0.5 to 0.7 μm) must be known, as neutral density filters will be used to adjust the radiance levels of the planetary test patterns to the levels just computed (row 3 of Table XXIV). The total irradiance of the illuminator over the above spectral range is

$$S_{\lambda_{(0.5\text{-}0.7\mu m)}} = \int_{0.5\mu m}^{0.7\mu m} S_\lambda \, d\lambda \qquad (7\text{-}1)$$

$$= 118.8 \text{ W/m}^2 \text{ (0.5-0.7μm) (from Appendix D)}$$

The corresponding value of radiance is

$$H_{\lambda_{(0.5\text{-}0.7\mu m)}} = \frac{118.8}{\pi} = 37.82 \text{ W/m}^2\text{-sr (0.5-0.7μm)}$$

Exposure on phototransistor array from illuminator. – The dark noise level of the phototransistor array, or noise equivalent signal (NES), is expressed in terms of energy density on the array during the exposure interval, using the units of Joules per square meter. The dark noise level is 1.2×10^{-6} J/m^2, and in Section 7.2.1 has been computed as equivalent to 792 photoelectrons. The preamplifier circuits in the experimental photo-imaging system are limited to a dynamic range of 540/1 above this level, where saturation occurs.

To ensure that test pattern radiance levels do not exceed the dynamic range of the sensor, the exposure on the array should be determined from the radiance level of the test pattern illuminator.

To determine this level, from the values just defined, it is clear that an exposure of 1.0×10^{-6} J/m^2 is equivalent to 660 photoelectrons. The exposure from the radiance level of the illuminator on the array, is then

$$E = \frac{\dfrac{a\,t_1}{4\,f_1^2\,h\,c} \displaystyle\int_{0.5\mu m}^{0.7\mu m} S_\lambda\, t_\lambda\, G_\lambda\, \lambda\, d\lambda}{660} \qquad (7\text{-}2)$$

$$E = 1210\ \mu J/m^2 \qquad \text{(from Appendix D)}$$

where the numerator of the equation is used to compute the number of photoelectrons generated within one element of the array by the unattenuated radiance of the illuminator.

7.3
Test Pattern Characteristics

Four photographic test patterns were selected for the laboratory test program. For the simulation of planetary imagery, two photographs of the earth were selected from the collection of Apollo photography at TRW Systems. Because the planets have a dense atmosphere and are covered with clouds, photographs of the earth were selected, in preference to photographs of the planets obtained from earth-based observatories. The latter, generally of low resolution, would not demonstrate the resolution capabilities of the photo-imaging system.

To simulate imagery of the entire planet obtained from a long range, a photograph of the full earth in gibbous phase was selected (Figure 47). The contrast of this photograph was deliberately reduced in photo-reproduction to obtain a more realistic simulation of a cloud-covered planet. To simulate

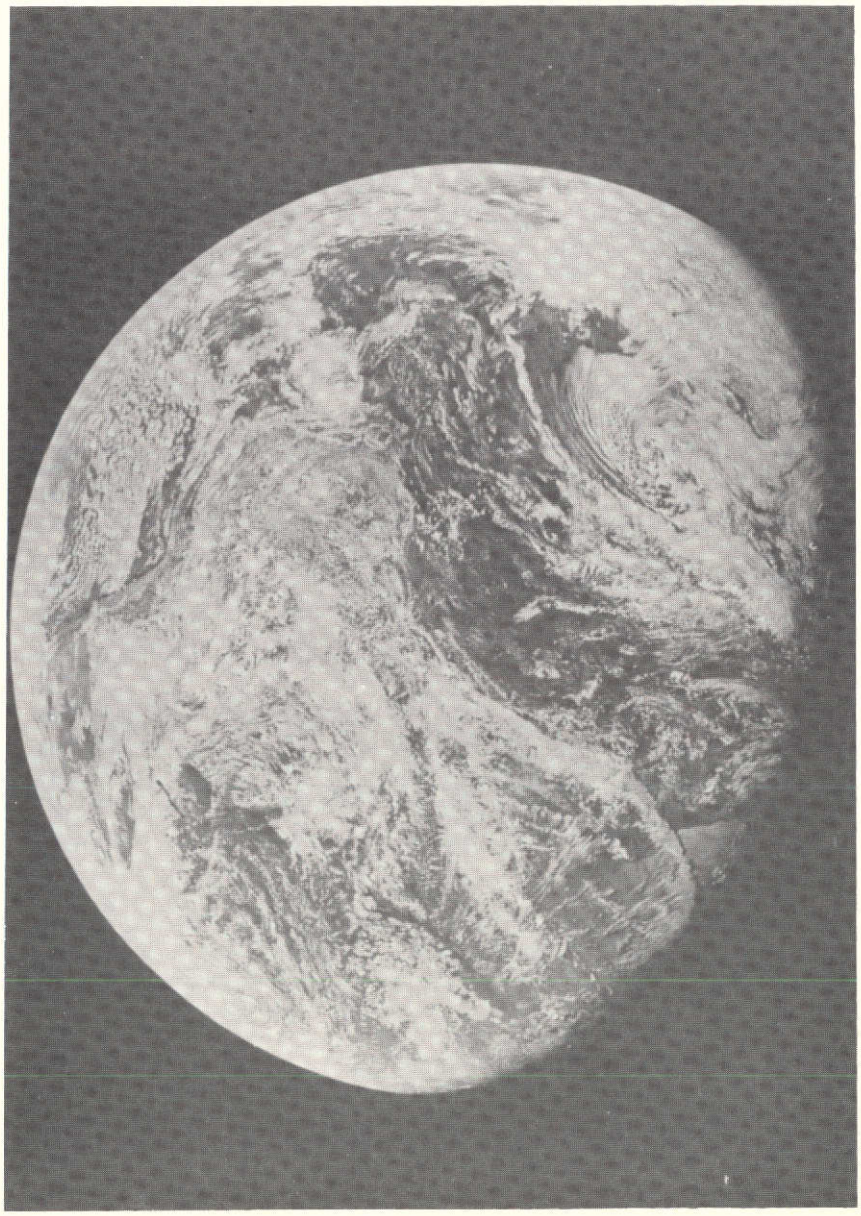

FIGURE 47. – EARTH IN GIBBOUS PHASE

imagery from close range, an Apollo 7 photograph of a hurricane formation obtained from earth orbit was selected (Figure 48).

To simulate imagery obtained from planetary satellites, which have either no atmosphere or tenuous atmosphere only (such as Titan), lunar photographs were selected from the Hale Observatory collection at the California Institute of Technology. The photograph of the full moon (Figure 49) simulates imagery obtained from a long range, and the photograph of a small area of the moon in the region of Clavius (Figure 50) was selected to simulate imagery at close range.

All of the photographic test patterns were produced on 4 x 5-in. glass photographic plates to prevent deformation during extended tests in the laboratory that might be caused by the heat load from the illumination source.

In addition to the test patterns previously described, a resolution chart was developed, consisting of two television-type bar burst patterns – one oriented horizontally and the other vertically – and a standard USAF three-bar resolution chart.

7.3.1 Optical Transmission and Density Characteristics of Test Patterns

The average optical transmission of each photographic transparency was measured to scale the radiance (brightness) levels for the laboratory tests. Using the laboratory illumination source, the average optical transmission was measured with a General Electric DW-68 light meter. The radiation sensor in this meter is a selenium cell. Care was taken to select images with a reasonable value of optical transmission in order to minimize the power requirements of the illumination source. The results are presented in Table XXV.

To estimate the highlight and lowlight levels for each image, traces were also made across regions of maximum contrast, using a Joyce Loebl Mk III microdensitomer. Low contrast imagery was used for scenes simulating cloud-covered planetary images, and high contrast images for scenes simulating satellites without atmospheres. Under these rules, the earth scenes would be

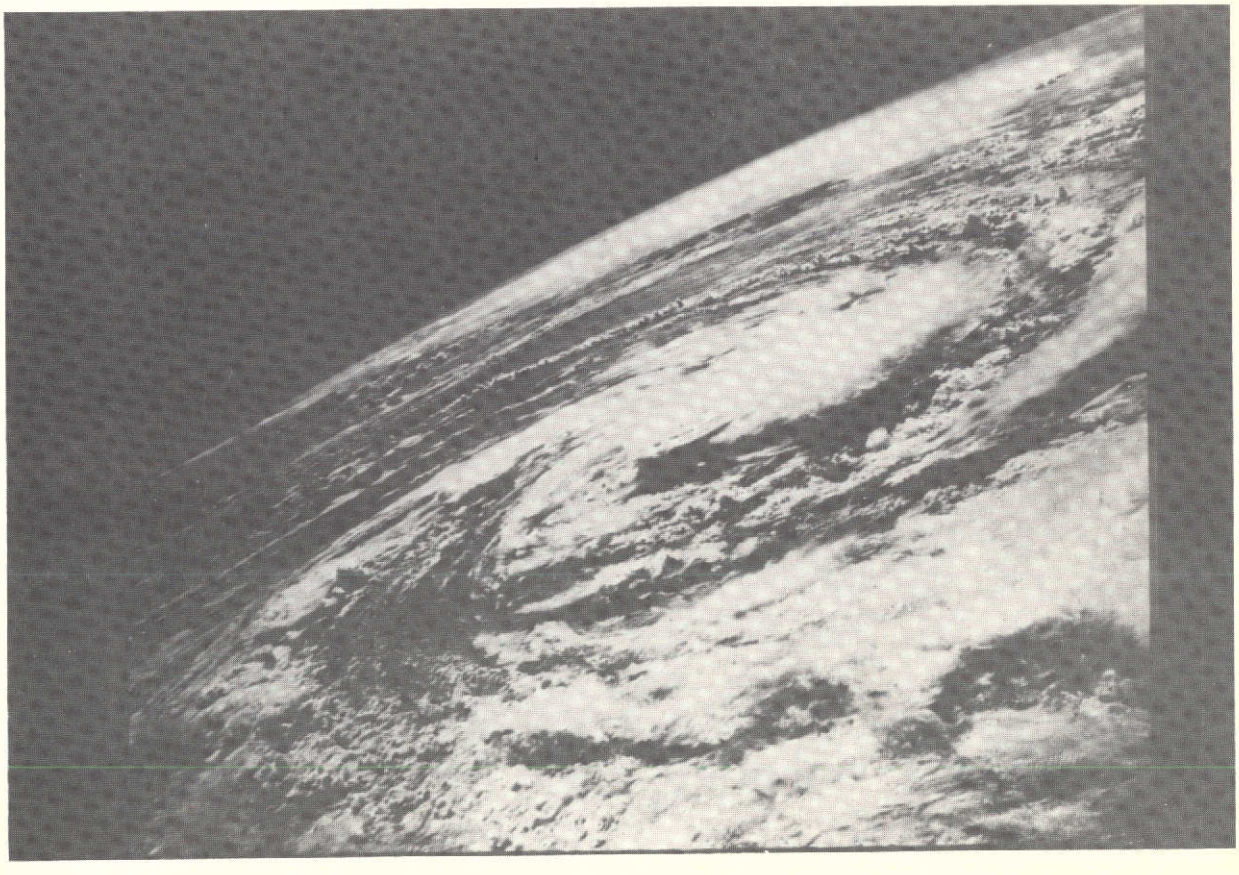

FIGURE 48. – HURRICANE FORMATION

FIGURE 49. – FULL MOON

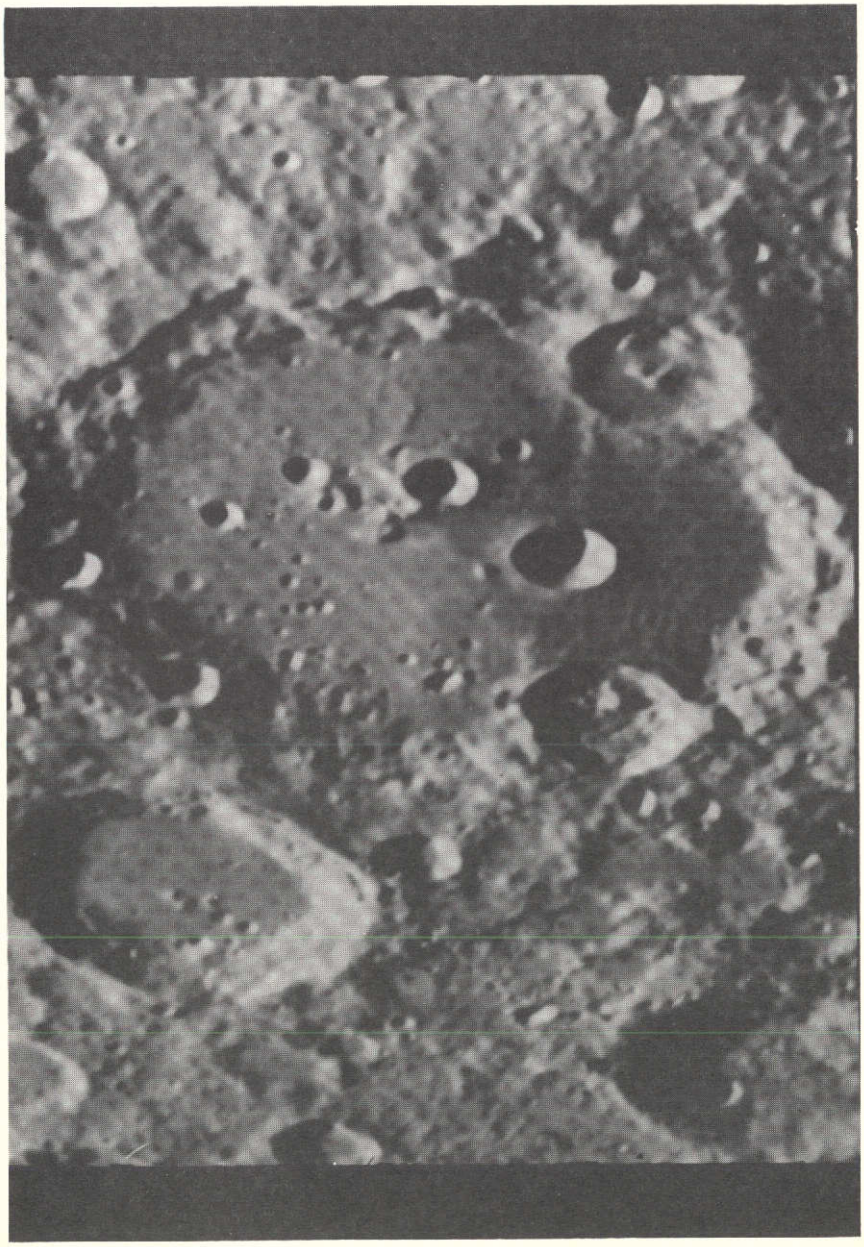

FIGURE 50. – MOON, REGION OF CLAVIUS

TABLE XXV. – AVERAGE OPTICAL TRANSMISSION OF TEST PATTERNS

Image	Average Transmission
Full Earth	0.36
Hurricane	0.27
Full Moon	0.36
Telephoto Moon	0.25

of low contrast, and the moon photos high contrast, but the hurricane scene is an exception and is of high contrast (see Table XXVI).

Microdensitometer measurements were made using a square scanning aperture with linear dimensions of 125 μm (5×10^{-3} in.) on a side. With a scene format of 5 x 5 cm (2 x 2 in.), the scanning aperture provided approximately 400 sampling elements, closely approximating the scan line density of the laboratory and the space-borne photo-imaging systems. The results of these densitometer plots are presented in Figures 51 through 54. On the photographic transparency of the full moon, densitometer measurements were also made, but with the scanning aperture reduced to simulate 1000 sampling elements; no appreciable change in density extremes was observed.

The resolution chart was also measured to determine maximum and minimum transmission values. Highlight transmission of the white bars on the patterns was 93.5%, and the transmission of the dark background (with a density in excess of 4.0) was less than 0.01 percent.

TABLE XXVI. – MEASURED CONTRAST OF TEST PATTERNS

Image	Density Extremes, Range	Transmission, Range
Full Earth	1.00 - 0.15 = 0.85	7.1:1
Hurricane	2.58 - 0.06 = 2.52	330:1
Full Moon	2.50 - 0.17 = 2.33	213:1
Telephoto Moon	1.90 - 0.13 = 1.77	59:1

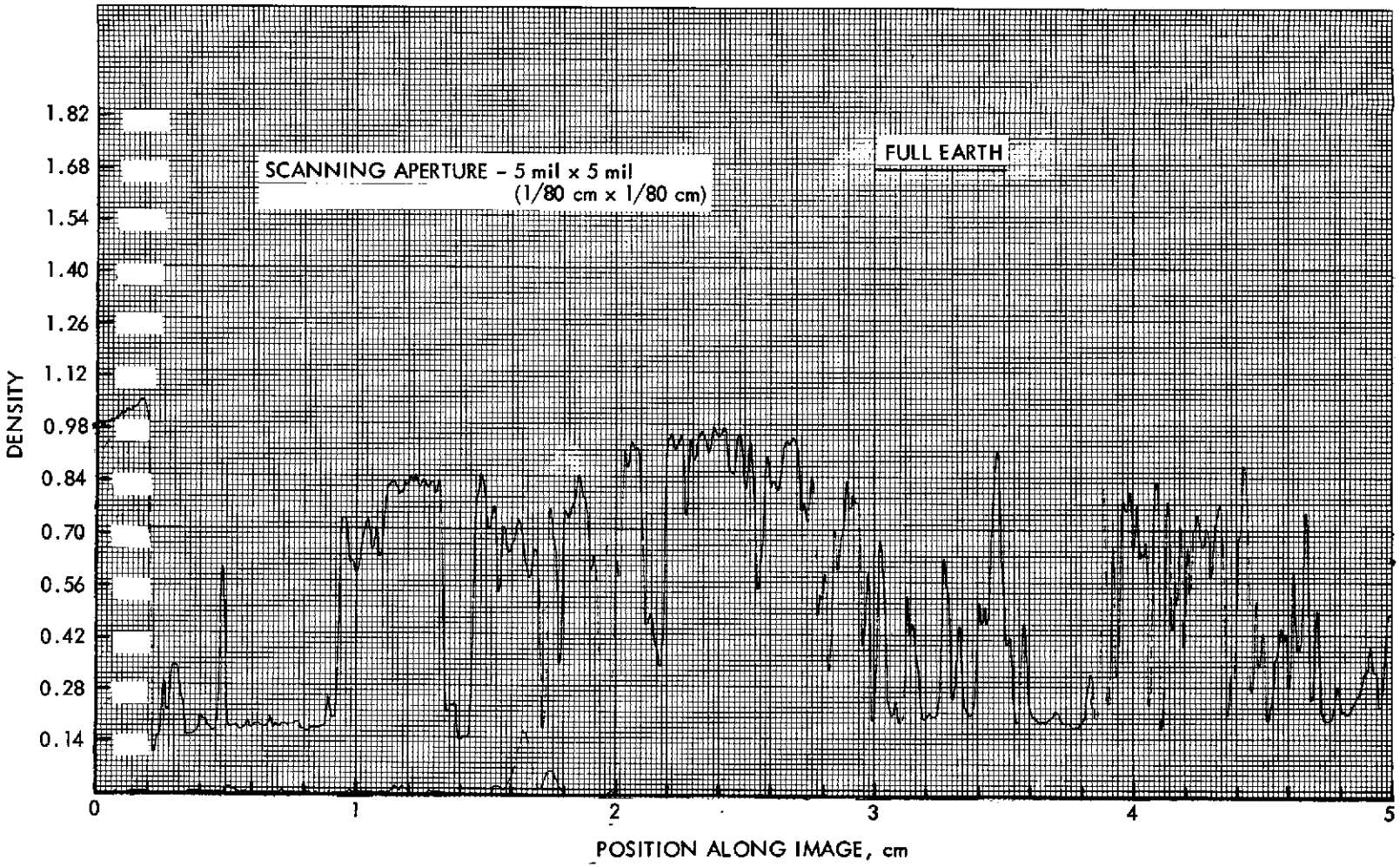

FIGURE 51. – DENSITOMETER PLOT OF FULL EARTH TRANSPARENCY

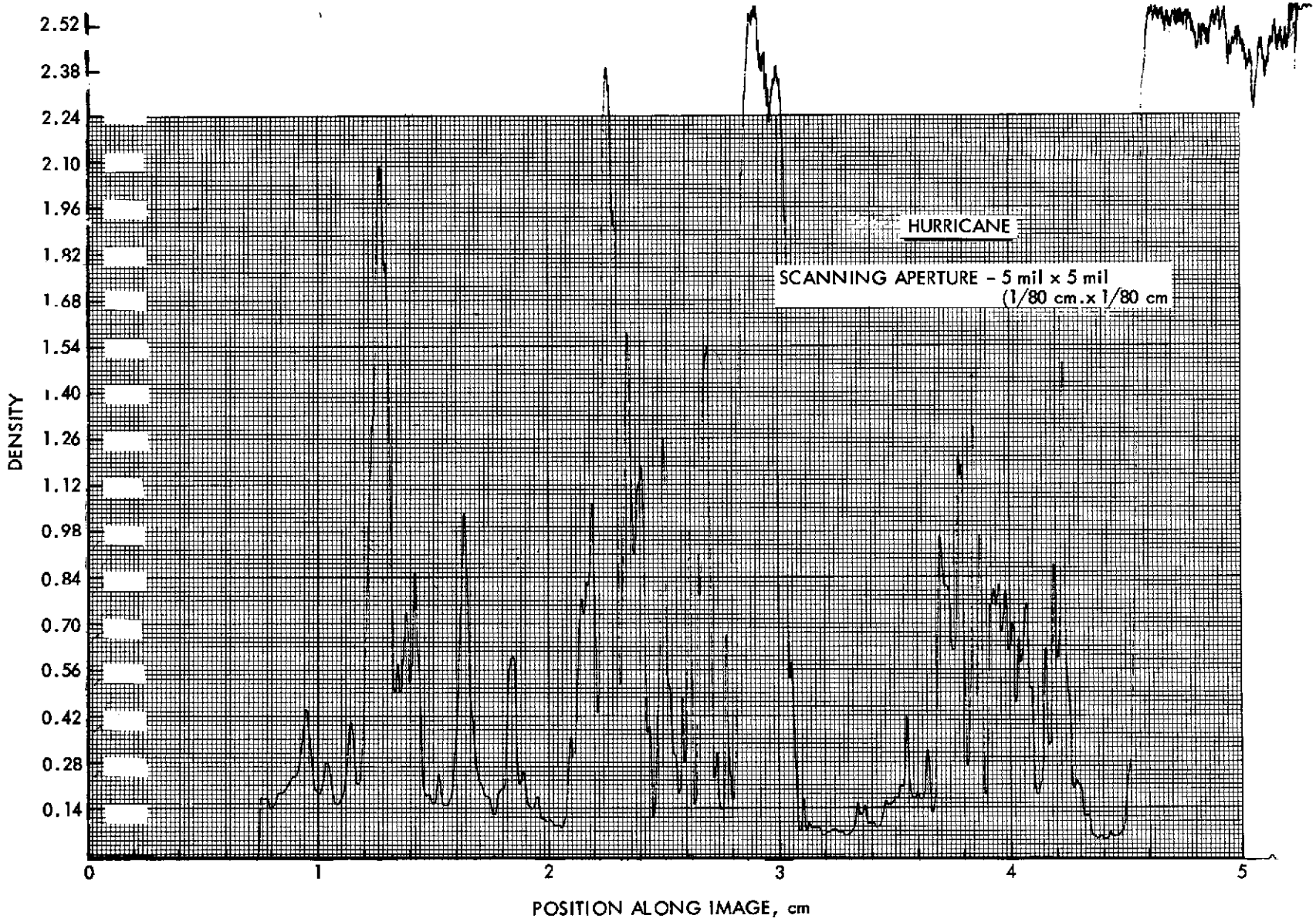

FIGURE 52. — DENSITOMETER PLOT OF HURRICANE TRANSPARENCY

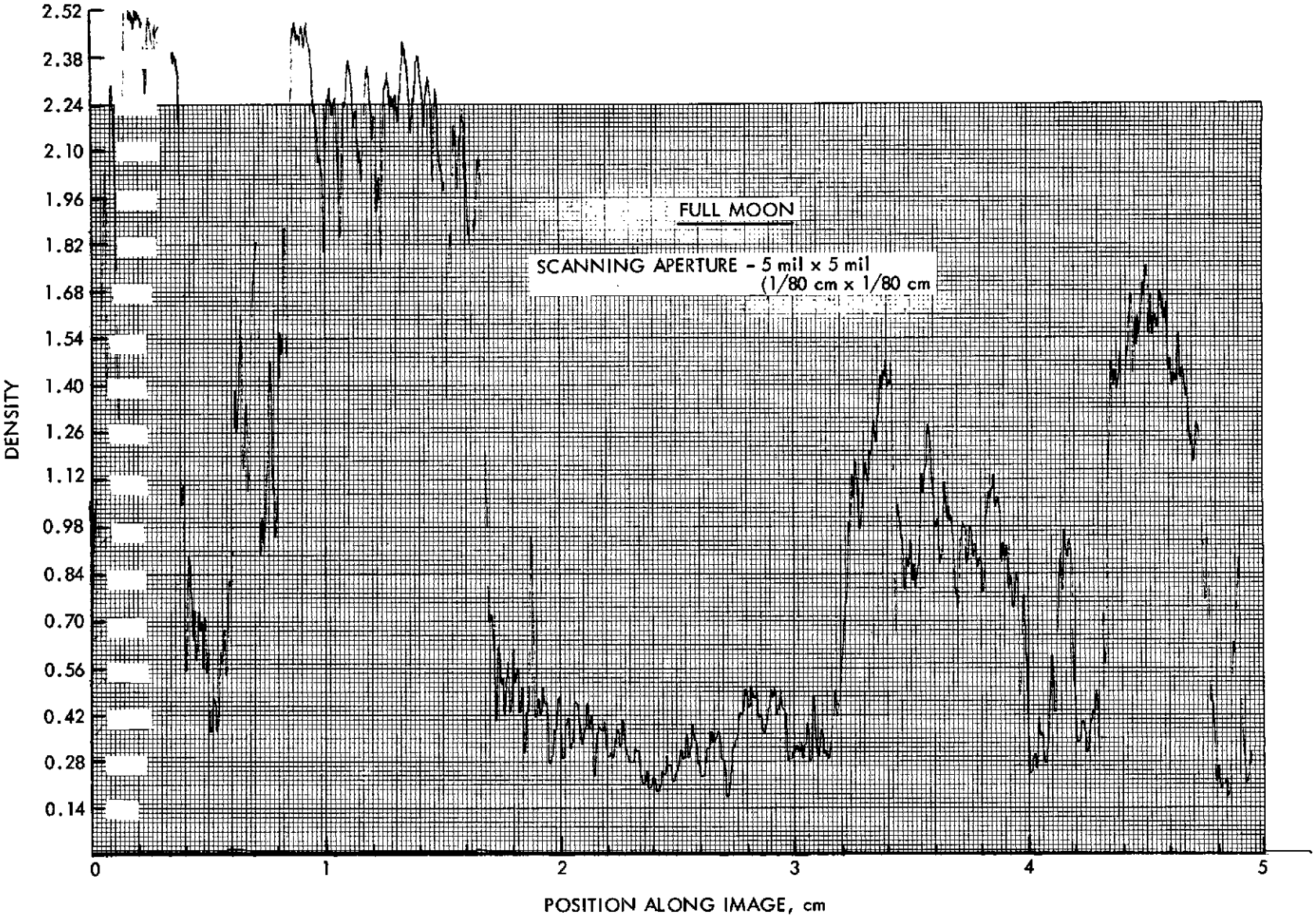

FIGURE 53. – DENSITOMETER PLOT OF FULL MOON TRANSPARENCY

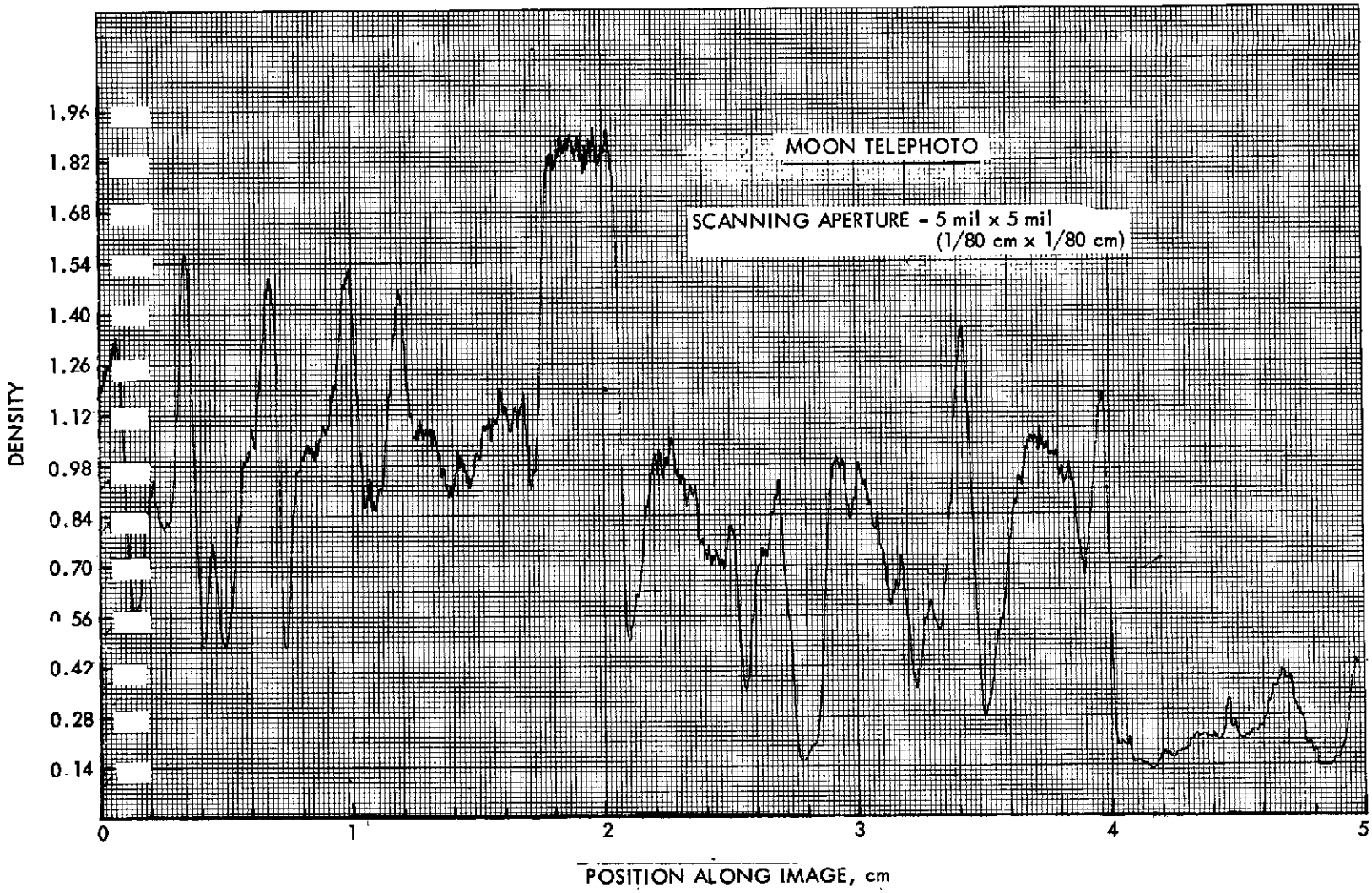

FIGURE 54. – DENSITOMETER PLOT OF MOON (REGION OF CLAVIUS) TRANSPARENCY

The average values of optical transmission were used as a basis for establishing the illumination levels in laboratory tests. In the case of the full earth transparency, a cross-check was made against the data obtained with the densitometer. The average value of transmission obtained with the DW-68 light meter was 0.36. The value of transmission by averaging 24 values from the densitometer trace was 0.37.

7.4
Summary of Laboratory Tests

A summary of the laboratory tests is presented in Table XXVII. Imagery of Jupiter, Io, Europa, Saturn, and Titan was simulated by using the photographic test patterns listed in row 2 of the table. Two test patterns were used to simulate Jupiter imagery, one simulating the complete planet and the other simulating a view from close range. Imagery of Saturn was not simulated, as it represented the use of an intermediate illumination level and would be similar to imagery of Titan. Two records of an illuminated resolution chart were also obtained, to evaluate performance of the photo-imaging system at both high and low light levels.

The radiance level of the incandescent illumination source is specified in row 4 of the table. The radiance levels of the test patterns to properly simulate the radiance of the planets (previously computed in Section 7.2.4) are listed in row 5. These data computations were based on the average albedo of the planets. However, when simulating the brighter planets and satellites (Jupiter, Io, and Europa), it was found that when these levels of radiance were used, saturation occurred within the photo-imaging system (preamplification electronics) because of the higher radiance in the highlights of the transparencies (see densitometer plots, Section 7.3). Neutral density filters were therefore selected to prevent saturation in the highlight areas.

The radiance levels used for Titan and Uranus were also lower than the nominal values, owing to the limited availability of filters with precisely the required values of optical transmission.

It is also of interest to express the radiance levels used in the tests in terms of the exposure on the phototransistor array of the photo-imaging system. The system has a dark noise level corresponding to an exposure level of

TABLE XXVII. – SUMMARY OF LABORATORY TESTS AND RADIANCE LEVELS

TABLE XXII. – SUMMARY OF LABORATORY TESTS AND RADIANCE LEVELS

Test Item	Summary of Data								
1. Test Number	73-7A	73-9A	73-8A	73-9B	None	73-8A	73-7B	73-10A	73-10B
2. Planet or Satellite	Jupiter	Jupiter	Io	Europa	Saturn	Titan	Uranus	Resolution Chart	Resolution Chart
3. Test Pattern	Earth (Gibbous Phase)	Hurricane Photo	Full Moon	Moon Region of Clavius	None	Full Moon	Earth (Gibbous Phase)	Burst and 3-bar Pattern	Burst and 3-bar Pattern
4. Radiance of Incandescent Illuminator W/m^2-sr (0.5 - 0.7μm) (2659°K)	37.82	37.82	37.82	37.82	—	37.82	37.82	37.82	37.82
5. Test Pattern Radiance Desired W/m^2-sr (0.5 - 0.7μm) (2650°K)	9.06	9.06	15.72	14.53	—	4.22	1.43	High Level	Low Level
6. Optical Transmission of Test Pattern	0.36 (av)	0.37 (av)	0.36 (av)	0.25 (av)	—	0.36 (av)	0.36 (av)	0.935 (max) $<10^{-4}$ (min)	0.935 (max) $<10^{-4}$ (min)
7. Transmisiion of Neutral Density Filter Used in Laboratory Tests	0.285	0.285	0.285	0.285	—	0.153	0.051	0.285	0.051
8. Test Pattern Radiance Value Used in Tests W/m^2-sr (0.5 - 0.7μm) (2650°K) (3 x 6 x 7)	3.88 (av)	3.98 (av)	3.88 (av)	2.70 (av)	—	2.08 (av)	0.70 (av)	10.1 (max) ~0 (min)	1.80 (max) ~0 (min)

1.2×10^{-6} J/m^2. With a dynamic range of 500/1, saturation begins to occur at an exposure of 600×10^{-6} J/m^2. From Section 7.2.4, the exposure on the array from the illumination source (without a test pattern or neutral density filter) was calculated to be 1210×10^{-6} J/m^2. Referring to Table XXVIII, highlight transmission values of the test patterns are specified in row 5, resulting in the highlight exposure values on the array specified in row 7.

In the case of Jupiter, Io, and Europa, approximately one-half the dynamic range of the sensor was used. The highlight exposure from Titan used approximately one-fourth of the dynamic range, and for Uranus only 10% of the dynamic range was used.

In the two resolution tests, the first test (at a high radiance level) resulted in 50% of the dynamic range being used, and the low level test used only 7% of this range.

The test patterns were located at a distance of 100 cm (40 in.) from the objective lens. Focusing occurred through a precise movement of the test pattern illuminator along the optical axis to maximize the electronic signal output of individual detectors, with the sensor viewing an illuminated pinhole in the plane of the test pattern. The electronic signal was observed on an A-scan presentation on an oscilloscope. Each test pattern was scanned with the linear phototransistor array of the photo-imaging system by rotating the rotary table at a rate of 0.0283 rad/s, which was computed as follows:

$$\omega = \frac{p}{t_1 f_1}$$

where

p = detector pitch, 0.0152 mm

t_1 = detector integration cycle period = 4.8 ms

f_1 = effective focal length = 112 mm

Owing to limited data storage capacity, 160 10-bit samples per detector or lines were recorded at one time and transferred to magnetic tape. The rotary table was then re-indexed, using an optical shaft encoder and two counters

TABLE XXVIII. – SUMMARY OF HIGHLIGHT EXPOSURE VALUES ON PHOTOTRANSISTOR ARRAY IN LABORATORY TESTS

TABLE XXVIII. – SUMMARY OF HIGHLIGHT EXPOSURE VALUES ON PHOTOTRANSISTOR ARRAY IN LABORATORY TESTS

Test Item	Summary of Values								
1. Test Number	73-7A	73-9A	73-8A	73-9B	None	73-8A	73-7B	73-10A	73-10B
2. Planet or Satellite	Jupiter	Jupiter	Io	Europa	Saturn	Titan	Uranus	Resolution Chart	Resolution Chart
3. Test Pattern	Earth (Gibbous Phase)	Hurricane Photo	Full Moon	Moon, Region of Clavius	None	Full Moon	Earth (Gibbous Phase)	Burst and 3-bar Pattern	Burst and 3-bar Pattern
4. Exposure on Phototransistor Array from Illuminator ($\mu J/m^2$)	1210	1210	1210	1210	1210	1210	1210	1210	1210
5. Optical Transmission of Test Pattern (max)	0.71	0.87	0.67	0.74	—	0.67	0.71	0.93	0.93
6. Optical Transmission of Neutral Density Filter	0.285	0.285	0.285	0.285	—	0.153	0.051	0.285	0.051
7. Highlight Exposure on Phototransistor Array from Test Pattern with Neutral Density Filter ($\mu J/m^2$)	245	300	231	255	—	124	44	321	57

for keeping track of starting and stopping the points of data gathering. This allowed three files of 160 lines to be used to form a 480-line raster.

After the collection of data from the test patterns, an end-to-end system calibration was performed. Neutral density filters with transmission percentage values of 1.0, 1.35, 1.95, 3.4, 5.1, 9.2, 15.3, and 28.5 were used to provide eight levels of illumination (in addition to a dark level) for a gray scale calibration.

The procedure used in calibrating the neutral density filters is defined in Appendix E.

At each of the levels, a file (160 scan lines) of data was collected in digital form on tape, from which the mean could be computed as a measure of the signal level. For image reconstruction, software is used to perform a linear interpolation between the calibration levels. At the dark level, the standard deviation of the data is computed as a measure of detector and system noise.

The voltage on the incandescent lamps of the test pattern illuminator was maintained at 120 Vdc for all tests.

In recording data, one file (160 scan lines) of data is recorded in the data disc memory at a high rate. It is then played back at a reduced rate onto a 9-track raw data tape, after which it is converted to 7-track tape for software processing in an IBM 370/145 computer, and finally recopied to CDC internal binary format on the CDC 6500/7418. This data was then forwarded to the General Dynamics Corporation for printing the imagery with a laser-beam film recorder.

7.5
Feasibility Test Results

Six simulated images of the selected planets and satellites were produced in the laboratory test program, in addition to two records of a resolution chart (one record at a high illumination level and the other at a low illumination level).

Referring to rows 5 and 8 of Table XXVII, the illumination levels used in the tests were between two and five times lower than the nominal values desired (based on the average radiance of the planets and satellites) in order to prevent saturation of the photo-imaging system preamplification electronics (in the case of the brighter planets) and owing to the limited selection of neutral density filters available (in the case of the dimmer planets). Thus the quality of the imagery obtained should be considered as conservative, rather than optimistic.

In the printing of the data on the laser-beam film recorder at General Dynamics Corporation, Eastman Kodak type 3414 high definition aerial film was used and was developed with low contrast in order to accommodate a wide dynamic range of exposure. The linear density of the film under these conditions ranged from 0.2 to 1.2, with a gamma of approximately 0.5.

First, the imagery of the planets and satellites will be discussed from a qualitative standpoint. Quantitative data can be derived from the imagery of the resolution charts. In addition, the electronic signals from the photo-imaging system recorded in tests when the resolution chart was scanned are analyzed quantitatively from data defining both the S/N ratios and the actual MTFs of the sensor derived from the magnetic data tapes.

7.5.1
Qualitative Analysis of Imagery Produced

Photographic prints from the negative records produced on film by the laser-beam film recorder are presented in Figures 55 through 62. The objective of the test in which imagery of Jupiter is simulated from long range was to reproduce imagery from a test pattern of low contrast, such as a cloud-covered planet. In comparing this image with the pattern in the tests (Figure 47), loss of resolution is apparent. However, the pattern on a 3 x 4-in. glass plate had a resolution of several thousand line-pair, whereas the scan pattern of the photo-imaging system was 390 scan lines, or 195 line-pair, with approximately 80 percent of the scan-line density of commercial television kinescopes. On a qualitative basis, this test result is considered acceptable.

FIGURE 55. – SIMULATED IMAGERY OF JUPITER FROM LONG RANGE, TEST NO. 73-7A (SPACECRAFT SPIN RATE = 5 rpm)

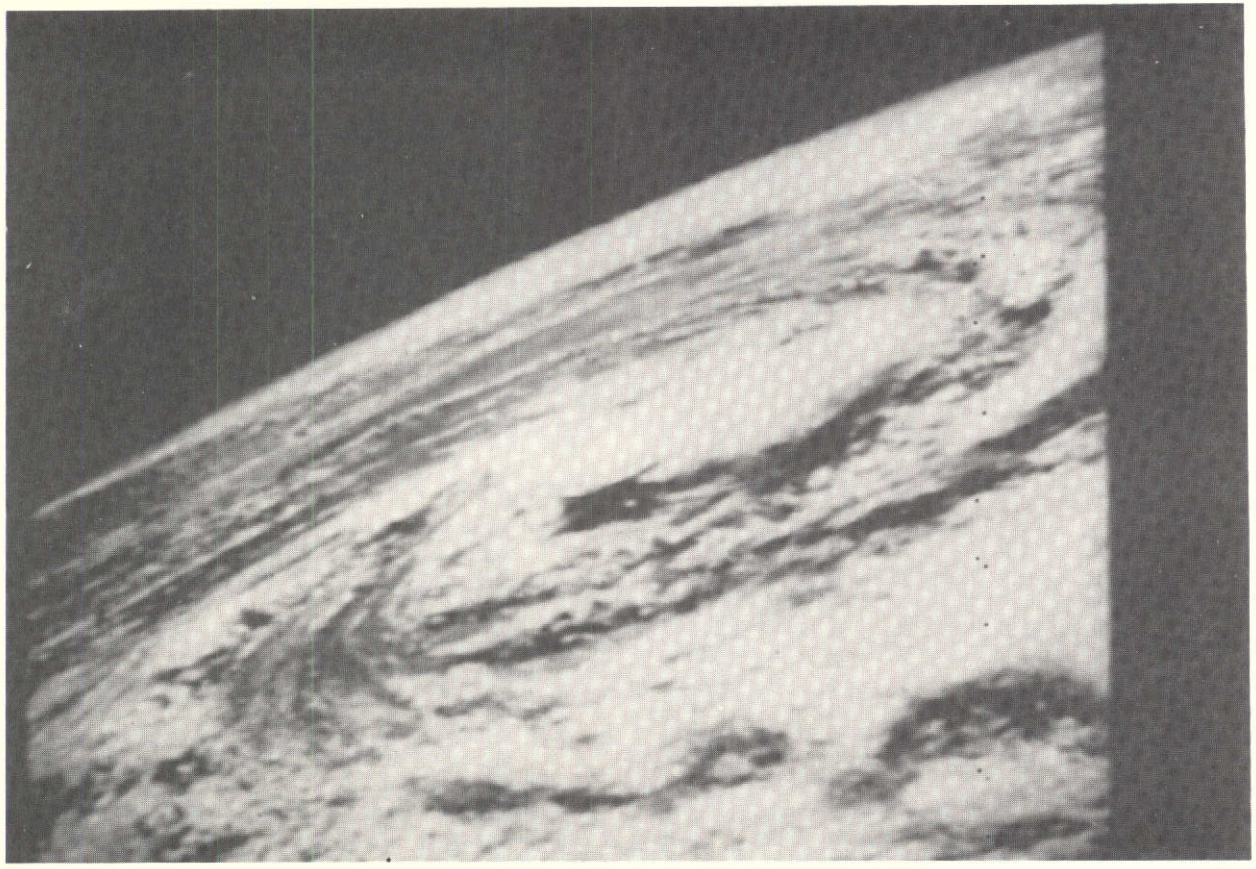

FIGURE 56. – SIMULATED IMAGERY OF JUPITER FROM CLOSE RANGE, TEST NO. 73-9A, (SPACECRAFT SPIN RATE = 5 rpm)

FIGURE 57. – SIMULATED IMAGERY OF IO FROM LONG RANGE,
TEST NO. 73-8A (SPACECRAFT SPIN RATE = 5 rpm)

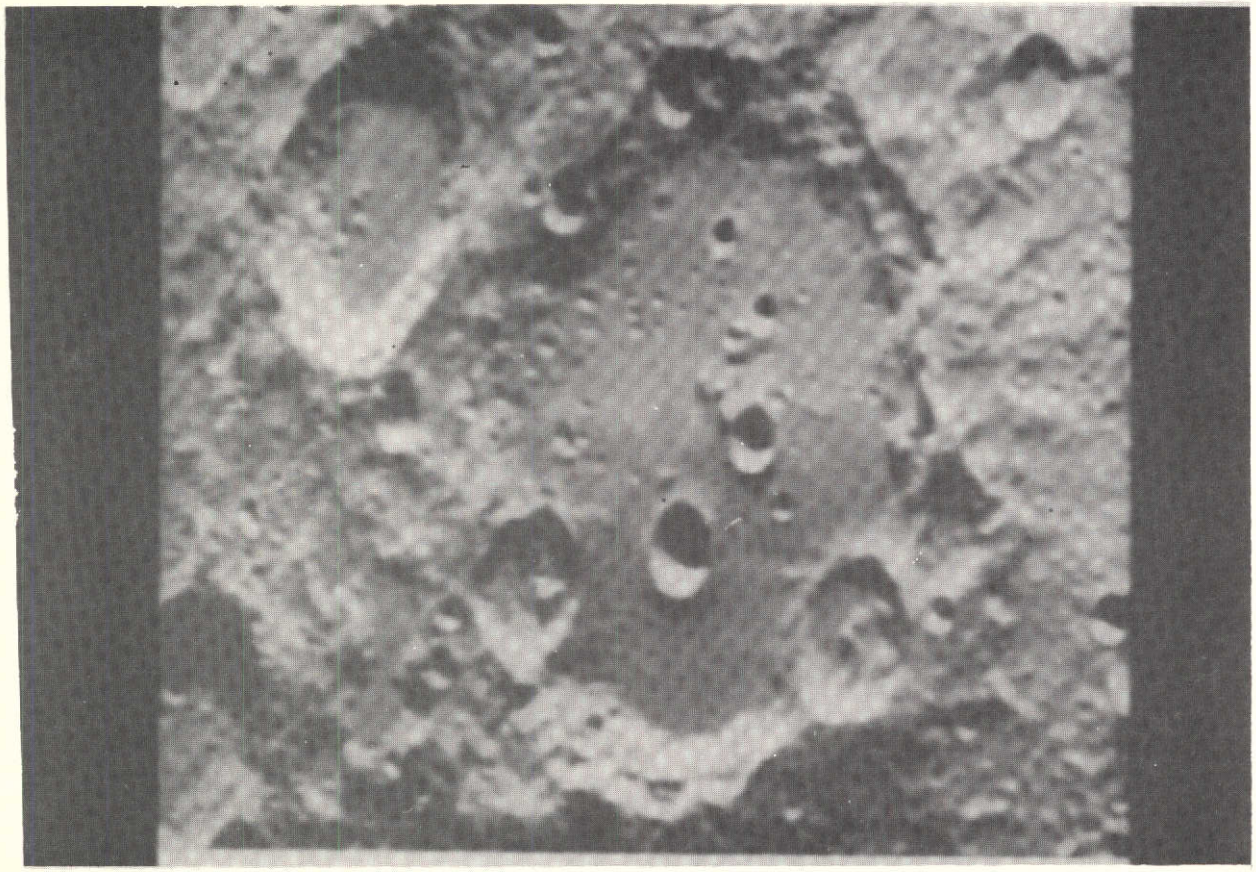

FIGURE 58. – SIMULATED IMAGERY OF EUROPA FROM CLOSE RANGE, TEST NO. 73-9B (SPACECRAFT SPIN RATE = 5 rpm)

FIGURE 59. – SIMULATED IMAGERY OF TITAN FROM LONG RANGE, TEST NO. 73-8A (SPACECRAFT SPIN RATE = 2 rpm)

FIGURE 60. – SIMULATED IMAGERY OF URANUS FROM LONG RANGE, TEST NO. 73-7B (SPACECRAFT SPIN RATE = 2 rpm)

In the image simulating an observation of Jupiter from close range (Figure 56), the quality from a subjective standpoint is much higher. This can be explained by the greater contrast of the photographic test pattern (Section 7.3.1)

In the simulation of Io imagery (Figure 57), a lunar photograph was used for the satellite without an atmosphere. In this case, the high contrast of the test pattern resulted in an image of excellent quality. Simulation of Europa imagery (Figure 58) also yielded an image of excellent quality when a lunar photograph was used as a test pattern. The simulated imagery of Titan, at approximately one-half the exposure of that used in the Io simulation (Table XXVIII), closely approximates the quality of the Io image. In comparing the simulation of Uranus (Figure 60) with that of Jupiter (Figure 55), the quality of the two images is similar, although the exposure level of the Uranus simulation was only one-seventh of that used in the Jupiter simulation (Table XXVIII).

In summary, the planetary and satellite imagery in all cases varies in quality from acceptable to excellent, and is highly dependent on the contrast of the scene being viewed. This imagery was obtained with phototransistor arrays that are currently in a mature state of development. With improvements anticipated in photodetector technology that indicate an improvement in sensitivity (lower dark noise) by a factor of approximately six, capability will be available to obtain imagery of planets at greater distances from the sun than those considered here. For example, with improved detectors, the imagery obtained in the Uranus simulation can be considered representative of that which would be obtained from observations of Neptune.

7.5.2
Quantitative Analysis of Imagery

The two records of a resolution test of the photo-imaging system are presented in Figures 61 and 62. The modulation contrast of the test pattern was 100%. The exposure used in the first record approximates that used with the Jupiter imagery, with the highlight level at one-half the dynamic range of the photo-imaging system. The exposure used in the second record approximates that used with the Uranus imagery, lower than the first record by a

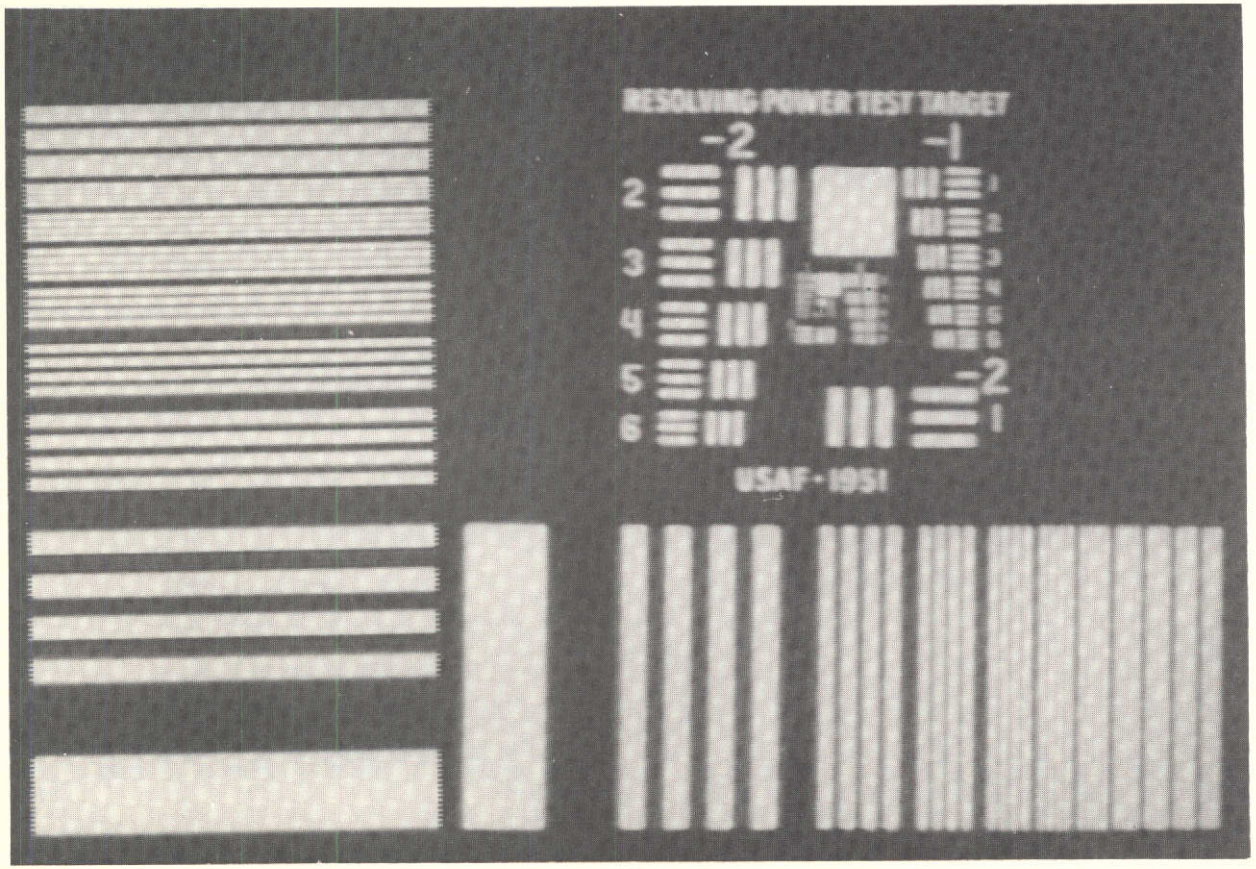

FIGURE 61. – RESOLUTION CHART AT EXPOSURE LEVEL OF JUPITER, TEST NO. 73-10A

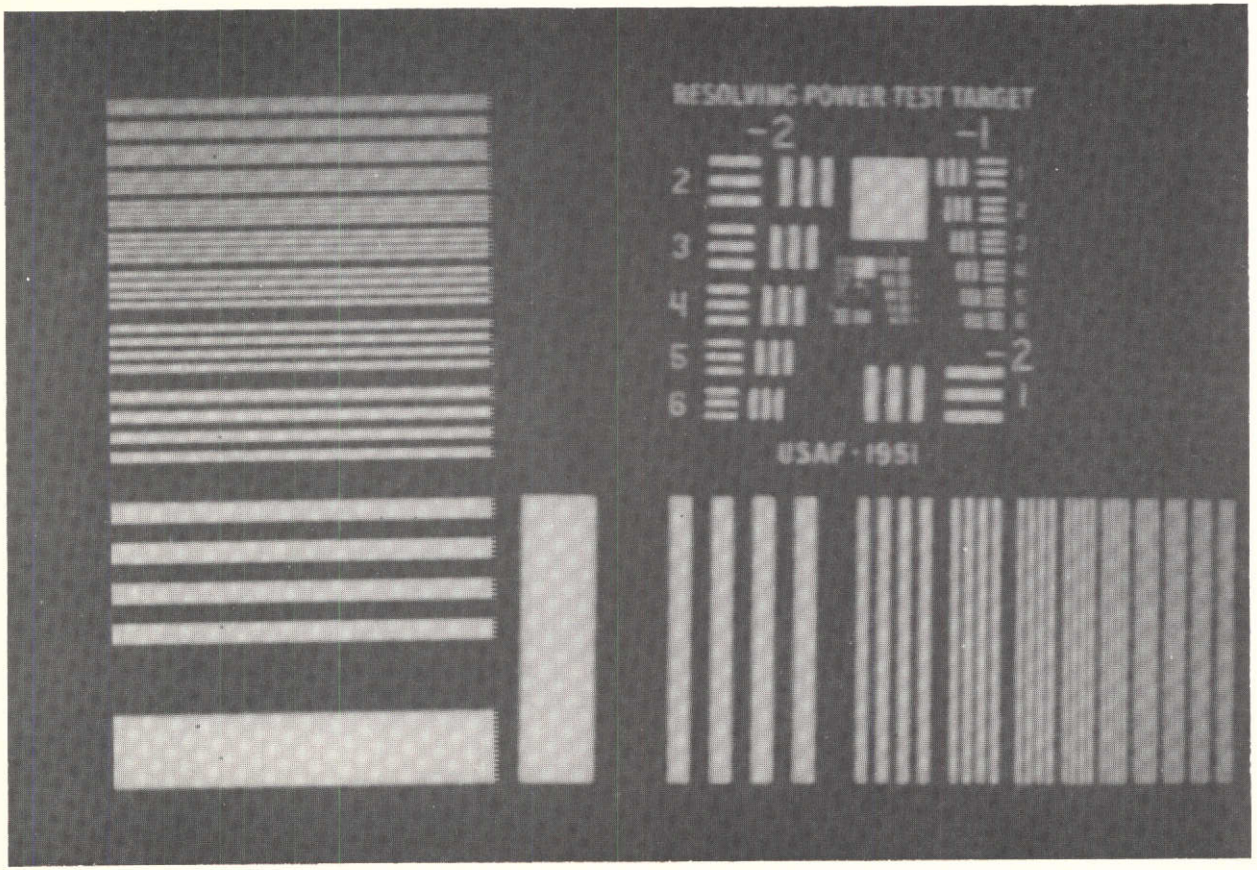

FIGURE 62. – RESOLUTION CHART AT EXPOSURE LEVEL OF URANUS, TEST NO. 73-10B

factor of 5.6, and using approximately seven percent of the dynamic range of the photo-imaging system. (See Table XXVIII for exact exposure values.)

The resolution chart was a composite of a television burst pattern and a USAF three-bar pattern. The line densities of the patterns at the sensor image plane (on the phototransistor array) are listed in Table XXIX.

The phototransistor array was oriented vertically with respect to the pattern. The vertical burst pattern record (on the left side of the photographs) was obtained with the photo-imaging system in a nonscanning mode, with 160 lines of data being recorded on magnetic tape and the rotary table stationary. This accounts for the "picket fence" pattern on the ends of the burst pattern bars – the software used in data processing was compensating for the offset between the two rows of phototransistors (see Figure 23).

The horizontal burst pattern records and the 3-bar pattern records were obtained with the photo-imaging system scanning in a horizontal direction, by driving the rotary table in azimuth. The spatial sampling frequency, determined by the pitch spacing of the elements of the phototransistor array (15.2 μm), is 32.8 lpm. Thus the limit of resolution, determined by the sampling or Nyquist frequency, above which aliasing will occur, is 32.8 lpm. This corresponds closely to the eighth bar group of the burst pattern and group zero, number 2, of the 3-bar pattern.

In the original record taken at the high exposure level (Figure 61), in the direction parallel to the phototransistor array (the vertical burst pattern), the bar patterns are distinguishable to the seventh group, at 27.7 lpm. In the direction of scanning, normal to the array, modulation to the sixth group (23.7 lpm) is discernible. On the 3-bar pattern, modulation in group zero, number 2 (upper right hand corner of inner spiral pattern) is barely discernible at a spatial frequency of 31.8 lpm.

In the original record taken at the lower exposure level (Figure 62), on the vertical burst pattern the bars are barely distinguishable at the eight group, at 31.6 lpm, and in the horizontal burst pattern are barely visible at the eighth group, also 31.6 lpm. In the 3-bar pattern, group zero, number 1 (lower left hand corner of inner spiral pattern) is barely discernible at 28.4 lpm. Higher values of resolution were obtained in the record taken at the lower exposure

TABLE XXIX. – RESOLUTION CHART DATA

Pattern		Density at image plane, lpm
Burst Pattern		
Wide bar group		–
1		3.96
2		7.92
3		11.9
4		15.8
5		19.7
6		23.7
7		27.7
8		31.6
9		35.6
10		39.6
Three-Bar Pattern		
Group	Number within group	
-2	1	7.09
	2	7.97
	3	8.99
	4	10.1
	5	11.3
	6	12.6
-1	1	14.2
	2	15.9
	3	18.0
	4	20.2
	5	22.6
	6	25.2
0	1	28.4
	2	31.8
	3	35.7
	4	40.0
	5	45.0
	6	50.5

level, and this can probably be explained by degradation in the photographic reproduction of the record obtained at the higher light level. Using the data from the low light level record, the resolution obtained may be summarized as follows:

	Spatial Resolution (lpm)
Parallel to Array (nonscan direction)	31.6
Normal to Array (scan direction)	31.6
Sampling (spatial) frequency (determined by detector element spacing)	32.8

In the following section a more precise estimate of the photo-imaging system performance is presented from an analysis of the video signals recorded on data tapes. This estimate is more definitive because the effects of the photographic reproduction processes have been eliminated.

7.5.3 Quantitative Evaluation of Photo-Imaging System Performance

To obtain a quantitative evaluation of the performance of the experimental photo-imaging system, a software routine was developed to permit analysis of the electronic video signals recorded on data tapes during the laboratory tests. In this manner, the performance of the sensor can be evaluated without the effects of subsequent degradation of the quality of the data by the transfer functions and limitations in dynamic range imposed by the recording of data on photographic film.

The basis for this evaluation was the two records obtained of the burst patterns on the resolution chart (at high and low illumination levels). The software routine selected one horizontal line scan and one vertical line scan from the data recorded on magnetic tape, and the signal current values at each data point along the two lines were printed out, in units of equivalent exposure, in $\mu J/m^2$. In addition, the software routine computed the NES, or dark noise level, under conditions of no illumination on the phototransistor array. The data thus obtained were used to determine (a) the S/N ratios at zero spatial frequency,

and (b) the MTFs from zero spatial frequency to the spatial sampling frequency of 32.8 lpm. In addition, a theoretical computation was performed to obtain estimated values of the S/N ratios at zero spatial frequency.

Comparison of Predicted and Measured S/N Ratios

When observing the resolution chart composed of a bar pattern, the average noise level from the sensor is

$$\overline{NES} = \left[(NES)^2 + \left(\frac{n_{max} - n_{min}}{2} \right) \right]^{1/2} \tag{7-3}$$

where

$\overline{NES}$ = average noise level

NES = dark noise level

n_{max} = electron charge induced by test pattern high-light

n_{min} = electron charge induced by test pattern low-light

with all terms being expressed in terms of the photoelectron equivalent values.

The signal-to-noise ratio at zero spatial frequency is

$$S/N = \frac{n_{max} - n_{min}}{\overline{NES}} \tag{7-4}$$

In the first four data columns of Table XXX, a theoretical estimate of the S/N ratio at zero spatial frequency is computed from the following input data:

a. The scale factor, from exposure in $\mu J/m^2$ to equivalent photoelectrons (Section 7.4)

b. NES value of 1.2 $\mu J/m^2$ (Section 7.2.1)

c. The high-light exposure levels (Table XXVIII)

d. The low-light exposure levels (Table XXVII).

TABLE XXX. – COMPARISON OF PREDICTED AND MEASURED SIGNAL-TO-NOISE RATIOS

Test Pattern Illumination Level	Theoretical Values				Measured Values			
	High		Low		High		Low	
Test Number	73-10 A		73-10 B		73-10 A		73-10 B	
	$\mu J/m^2$	Photoelectrons	$\mu J/m^2$	Photoelectrons	$\mu J/m^2$	Photoelectrons	$\mu J/m^2$	Photoelectrons
Scale Factor $\mu J/m^2$ to photoelectrons (from Section 7.4)	1.0	660[a]	1.0	660	1.0	660	1.0	660
NES Noise Equivalent Signal (Dark Noise)	1.2[b]	792	1.2[b]	792	0.7	462	0.7	462
E_{mex} Highlight Exposure from Test Pattern on Phototransistor Array	321[c]	211 860	57[c]	37 620	285	118 100	50.7	33 462
E_{min} Lowlight Exposure from Test Pattern on Phototransistor Array	0[d]	0	0[d]	0	4.2	2752	0.74	488
$\overline{NES}$ Average Noise Equivalent Signal	1.31	856	1.22	804	0.84	557	0.73	480
Signal-to-Noise Ratio at Zero Spatial Frequency	248		46.8		332		68.6	

[a] From Section 7.4.

[b] From Section 7.2.1.

[c] From Table 7-18.

[d] From Table 7-17.

For test number 73-10A, using the resolution chart with a high level of illumination, the S/N ratio is calculated as 248/1. For test number 73-10B, using the resolution chart with a low level of illumination, the S/N ratio is calculated as 46.8.

In the second set of four data columns in Table XXX, the same computation is performed using measured values obtained by the software routine from the video data tapes. Under the high level of illumination, the S/N ratio is calculated as 332, and under the low level of illumination as 68.6.

The results, illustrating that the measured performance was better than the theoretical estimate, can be accounted for by a conservative estimate of the NES in the theoretical calculation (1.2 $\mu J/m^2$), compared with the measured value of 0.7 $\mu J/m^2$.

Comparison of Predicted and Measured Modulation Transfer Functions

The value of the modulation transfer function at any spatial frequency is given by

$$m_0 = \frac{n_{max} - n_{min}}{n_{max} + n_{min}} \tag{7-5}$$

where n_{max} is the electron charge induced by the test pattern high light; n_{min} is the electron charge induced by the test pattern low light; and the S/N ratio at any spatial frequency is given by Equation (7-4). The spatial frequency at the image plane for each of the 10 four-bar bursts is given by

$$f = 3.96\ n\ (lpm)$$

where n is the burst pattern group number as it changes arithmetically from 1 through 10.

The MTFs corresponding to the spatial frequencies at the image plane, computed by the use of Equation (7-5) with the data from the video recording on magnetic tape, is illustrated in Figure 63 for the direction normal to the phototransistor array (the direction of the mechanical azimuth scan) and in Figure 64 for the direction parallel to the array. For comparison, the theoretical values of the MTFs previously computed in Section 7.2.1 are also shown.

A comparison of the theoretical and measured MTFs shows that the measured values in each direction are lower than predicted. Part of the reduction can be explained by slight out-of-focus conditions in the laboratory tests. When the test pattern was observed at a conjugate distance of 100 cm from the objective lens, and the mechanical scan with the rotary table in azimuth was used, a flat object plane was also used, whereas the plane should be curved for precise focus. This may explain the greater reduction of the MTF in the direction normal to the array, in the direction of the azimuth scan. The reduction of the MTF parallel to the array (vertical in the laboratory tests), is probably due to difficulty in obtaining a precise focus on the test pattern.

In Figures 65 and 66, the measured S/N ratios are plotted as a function of spatial frequency for both of the tests, using the resolution chart. These S/N ratios were also obtained from values of the video data on magnetic tape, and from substituting values in Equation (7-4).

Note that the S/N ratios obtained, ranging up to 332/1, are approximately three times higher than those available with conventional television camera systems, which are limited to values in the order of one hundred to one.

8.0
CONCLUSIONS

The results of this study have demonstrated that it is feasible to obtain high resolution imagery of the outer planets and satellites at distances up to 19.2 AU from the sun, using currently available linear arrays of silicon phototransistors in a solid state photo-imaging system on a spinning spacecraft of the Pioneer type. Improvements anticipated in photodetector performance within the near future will provide the capability of obtaining imagery at distances from the sun up to 30 AU.

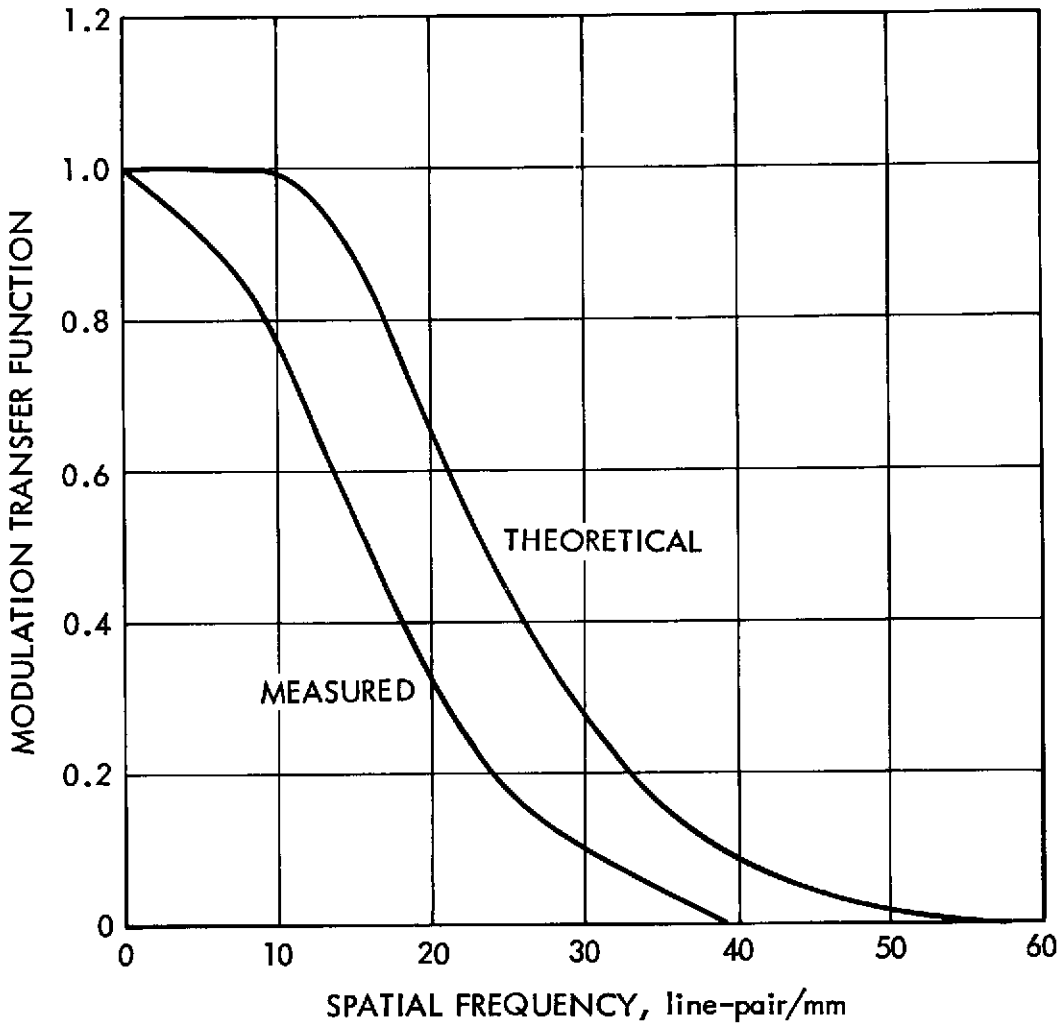

FIGURE 63. – MODULATION TRANSFER FUNCTIONS NORMAL TO PHOTOTRANSISTOR ARRAY

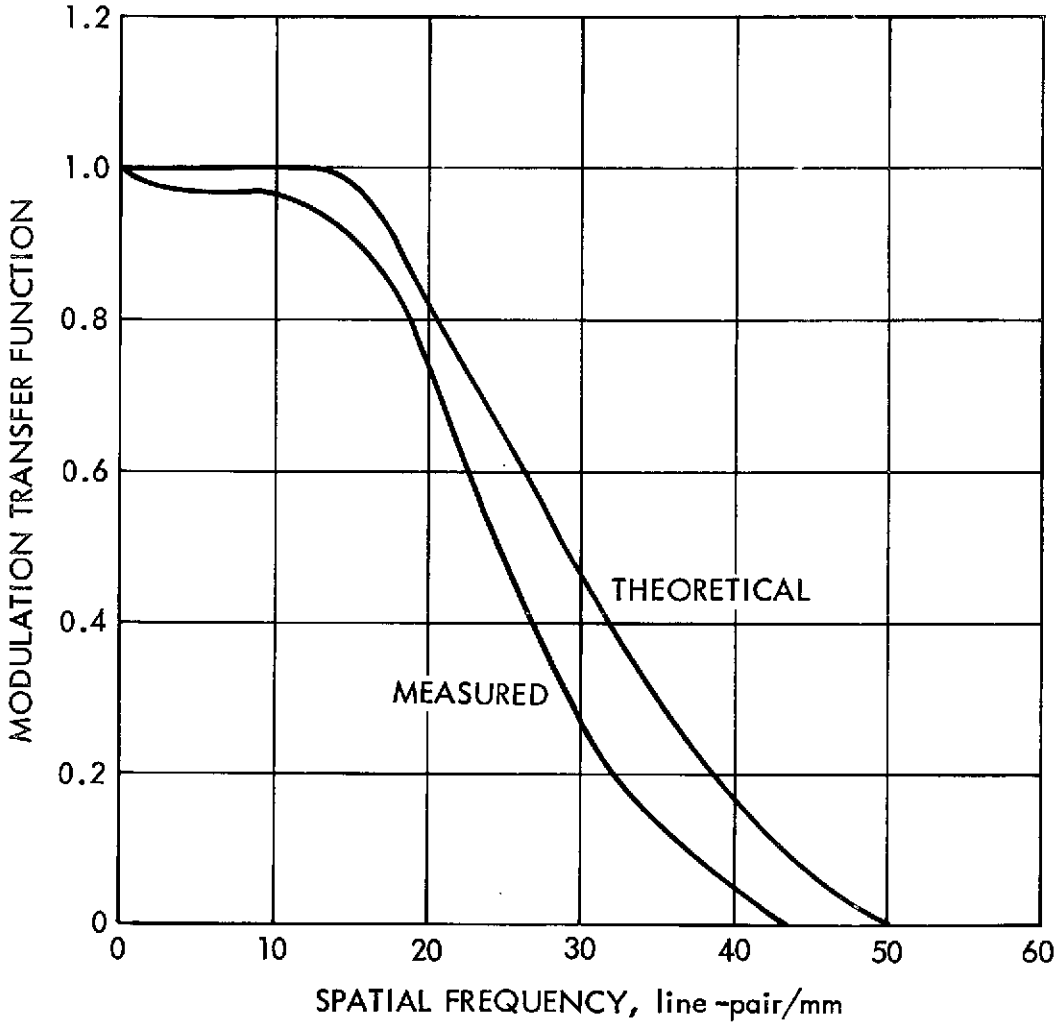

FIGURE 64. – MODULATION TRANSFER FUNCTIONS PARALLEL TO PHOTOTRANSISTOR ARRAY

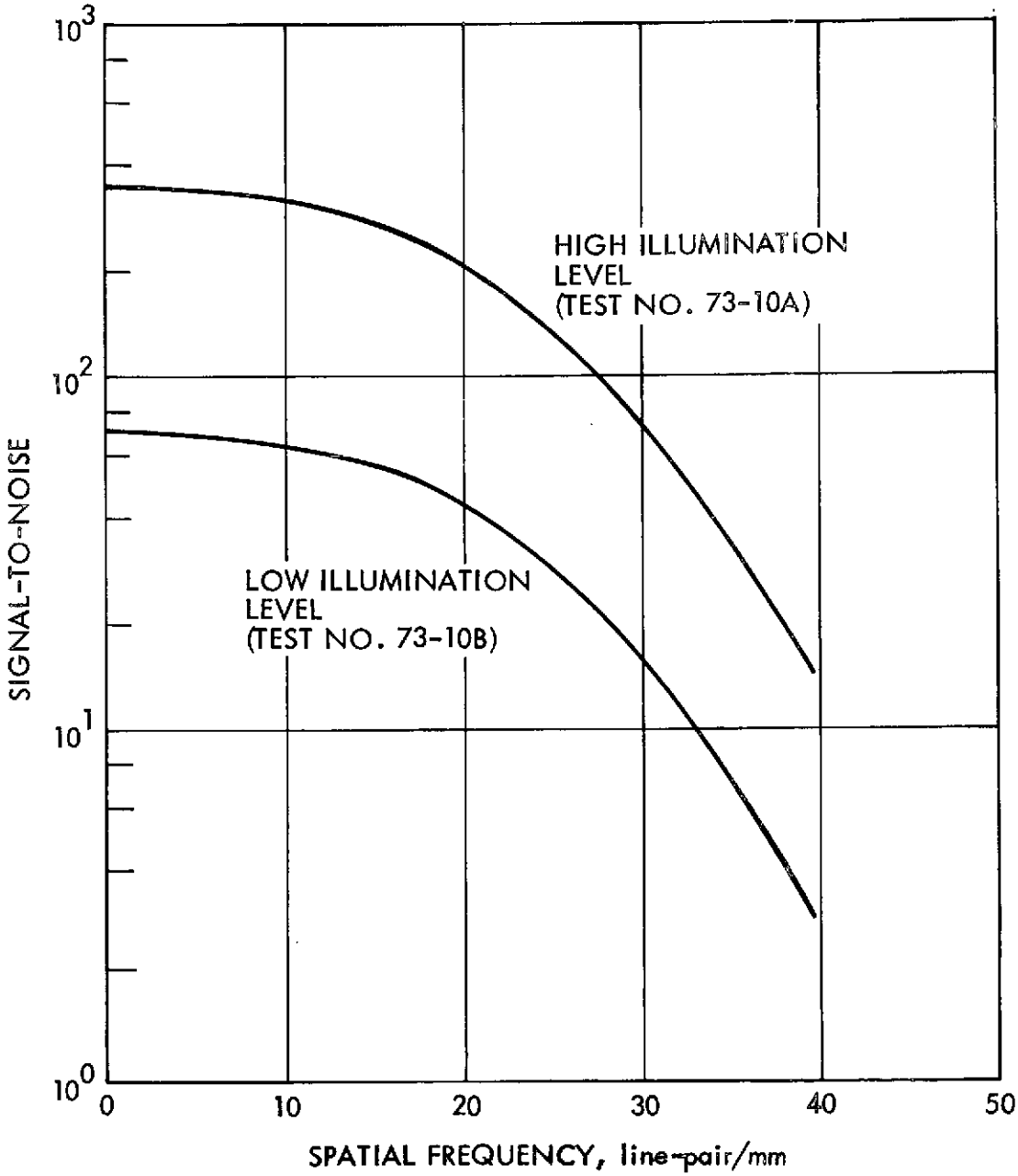

FIGURE 65. – MEASURED SIGNAL-TO-NOISE RATIOS NORMAL TO PHOTOTRANSISTOR ARRAY

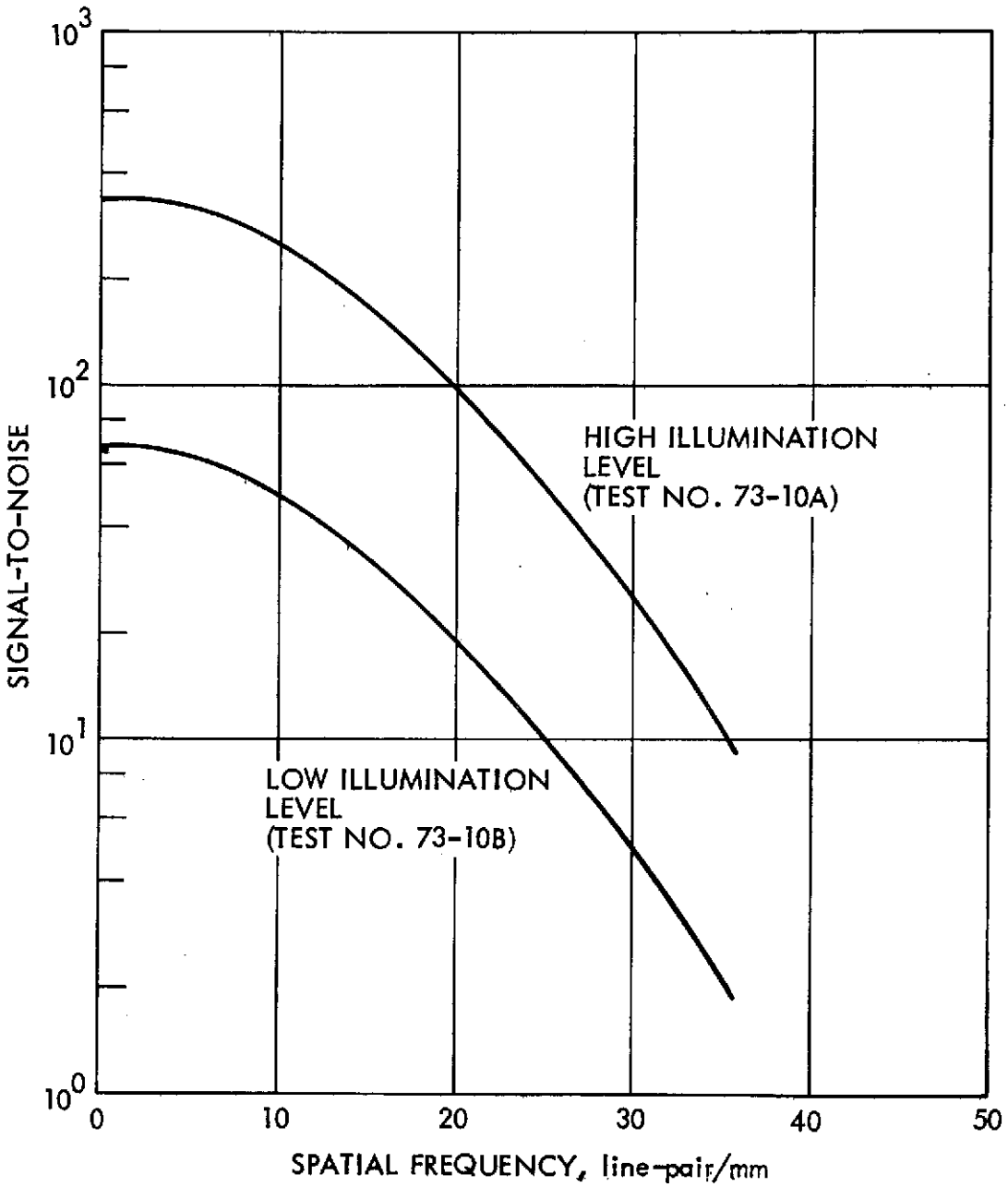

FIGURE 66. – MEASURED SIGNAL-TO-NOISE RATIOS PARALLEL TO PHOTOTRANSISTOR ARRAY

The quality of the imagery is highly dependent upon the optical contrast at the surface of the planet or satellite. With high optical contrast, the image quality is comparable in spatial resolution and contrast to that of commercial television displays.

Sequential multispectral imagery can be obtained in five spectral bands, from 0.4 to 1.1 μm, when observing planets at distances from the sun up to 9.5 AU with lower image quality than that obtained with the sensor operating in a broad-band monochrome mode. Improvements anticipated in the near-future in photodetector technology may permit multispectral imagery to be obtained when planets are observed at distances from the sun up to 19.2 AU.

Analysis of the photographic reproductions of simulated imagery obtained in the laboratory has shown that image quality varies from acceptable to excellent, depending on the contrast of the photographic test patterns used to simulate the characteristics of the planets. In reproductions of photographic resolution charts, spatial resolution up to the sampling (or Nyquist) frequency of the sensor is discernible.

Analysis of the video signals from the photo-imaging system, recorded in digital form on magnetic tape, shows that the S/N ratios at low spatial frequencies are in excess of predicted values. S/N ratios in excess of 300/1 have been obtained, approximately three times higher than the S/N ratios available using contemporary television camera tubes.

However, the measured modulation transfer functions are somewhat lower than predicted. This is attributed to difficulties encountered in achieving a precise focus of the optical system in laboratory tests.

A preliminary design configuration and preliminary specifications have been developed for a photo-imaging system compatible with the constraints of a Pioneer type of spacecraft for use in future outer planets missions. During typical encounters with the planets Jupiter, Saturn, and Uranus, the number of frames of imagery that can be transmitted are 2980, 605, and 42, respectively. If on-board data compression is used, reducing the data load per frame by a factor of 2.5, these values can be increased to 7491, 1515, and 106.

The proposed photo-imaging system offers a reduction in the complexity of reconstruction of imagery in ground data processing, in that an entire frame of imagery is obtained during a fraction of one revolution of the spacecraft, thus minimizing the geometric corrections that would otherwise be required to account for the motion of the spacecraft and the rotation of the planets during the photo-imaging sequence.

9.0
REFERENCES

1. Allen, C. W.: Astrophysical Quantities. Second ed., University of London, The Athlone Press, 1955, pg. 145.

2. Russell, Dugan, and Steward: Astronomy. Vol. I, The Solar system. Ginn and Co., Boston, USA, 1945, pp. 383, 393.

3. Russell, E., and Tomasko, M.: Final Presentation, Study of Spin Scan Imaging for Outer Planets Missions (for NASA Ames Research Center, By Santa Barbara Research Center and Lunar and Planetary Laboratory).

   The following are primary sources of data. (Albedo data is a composite of information obtained from these sources.)

   a. Harris, D. L.: Planets and Satellites. (Publisher and date not specified.)

   b. Appleby, J. F., and Irvine, W. M.: Astrophysical Journal. vol. 76, 1971, pg. 617.

   c. Irvine, W. M.: Astrophysical Journal. vol. 73, 1968, pg. 251.

   d. Binder, A. C., and McCarthy, E. W.: Astrophysical Journal. vol. 171, 1962, L1 to L3.

4. Outer Planets Pioneer Spacecraft, prepared for the National Aeronautics and Space Administration, Ames Research Center, Moffett Field, California, by TRW Systems, One Space Park, Redondo Beach, California, 23 March 1973.

5. Outer Planets Pioneer Spacecraft, National Aeronautics and Space Administration, Ames Research Center, Moffett Field, California. 23 March 1973.

6. Shade, Otto H., Sr.: The Resolving-Power Function and Quantum Processes of Television Cameras. RCA Review, vol. XXVIII, No. 3 September 1967, pp. 460-535.

7. Soule, Harold V.: Electro-Optical Photography at Low Illumination Levels. John Wiley & Sons, Inc., N.Y., 1968, pp. 321-344.

8. Richardson, Robert J.; Martin Co., Denver, Colo.: Quantization of Noisy Signals. IEE Transactions on Aerospace and Electronic Systems, May 1968, pp. 362.

9. O'Neill, E. L.: Transfer Function for an Annular Aperture. J.O.S.A. vol. 46, no. 4, April 1956, pp. 285-288.

10. Rosell, F. A., and Willson, R. H.: Performance Synthesis (Electro-Optical Sensors. Westinghouse Defense and Space Center, Aerospace and Electronic System Division, Baltimore, Md., Technical Report AFAL-TR-71-137, May 1971, pg. 96.

10.0
APPENDIXES

APPENDIX A

CALIBRATION OF TEST PATTERN ILLUMINATION SOURCE

Description of Illuminator

The illuminator consists of 10 showcase bulbs approximately twenty-five centimeters long in a planar array with approximately two and a half centimeters between the filaments. The array is enclosed with an opal glass diffuser on one side and a matte aluminum reflector on the other side. A blower supplies cooling air. Initially, a piece of heat-absorbing glass was placed between the light bulbs and the opal glass, but it fractured because of uneven heating and the calibration was finally done without heat-absorbing glass. The bulbs supply a nominal power of 75 watts each.

Measurement Method

The spectral irradiance of the illuminator was measured by comparing the output of the illuminator with the output of a Gamma Scientific irradiance source, using OCLI narrowband spectral filters to define the wave bands. When the same filter is used with each source, the filter bandwidth (if reasonably narrow) does not significantly affect the measurement; only the ratio of the measured output for the two sources is significant. A one-square-centimeter silicon solar cell, which energizes an operational amplifier with a 250 K feedback resistor to give an output of 0.25 V/μA of photocurrent, was used as a reference detector. The illuminator area viewed by the detector was masked to expose only a 5.1 x 5.1 cm square. The raw data for the measurement are given in Table A-I. The output of the reference detector as the detector observes the Gamma Scientific irradiance source, is given in Table A-II. The center wavelengths of the filters deviate slightly from the nominal values, as shown in Table A-III.

The ratio of output of the reference detector for the two sources was calculated at each wavelength, the published calibration of the gamma source was corrected by the inverse square law for the different distance, and the absolute irradiance at the reference cell for the 5.1 x 5.1 cm area of the illuminator was computed (Table A-IV). The irradiance values in column 3 of

Table A-IV represent the irradiance on the reference detector from the illumination source area of 5.1 x 5.1 cm at the test distance. From the measured irradiance, we calculate the irradiance at the illuminator surface, assuming the inverse square law and a labertian radiator:

$$H_{measured} = \frac{H_{surface}}{\pi} \times \frac{A_{source}}{S^2} = H_{surface} \times \frac{(5.1)^2}{\pi(91.8)^2}$$

$$H_{surface} = 1024\, H_{measured}$$

These data, presented in Table A-V, define the spectral irradiance at the surface of the test pattern illuminator.

TABLE A-I. — OUTPUT OF SILICON REFERENCE DETECTOR ON OBSERVATION OF TEST PATTERN ILLUMINATION SOURCE

λ (approx)	V_{Light}	V_{DK}	Repeat
Open	+5.658	-0.00203	+5.654
0.700	+0.06201	-0.00203	+0.0618
0.600	+0.03354	-0.00204	+0.03346
0.500	+0.00420	-0.00204	+0.00420
0.433	-0.00039	-0.00206	-0.00040
0.466	+0.00120	-0.00205	+0.00120
0.533	+0.01317	-0.00204	+0.01316
0.566	+0.02003	-0.00204	+0.02000
0.666	+0.07242	-0.00204	+0.07243
0.8	+0.11716	-0.00204	+0.11716
0.9	+0.14172	-0.00205	+0.14172
1.0	+0.10725	-0.00206	+0.10730
1.1	+0.02067	-0.00206	+0.02065
Open	+5.669		

Note

Reference cell: 4
Distrance from source: 91.8 cm
Nominal dc operating voltage: 120
Volts across 50 mV/10μA shunt: 0.03076 V

TABLE A-II. – OUTPUT OF SILICON REFERENCE DETECTOR ON OBSERVATION OF GAMMA SCIENTIFIC IRRADIANCE SOURCE

λ (approx)	V_{Light}	V_{DK}	Repeat
Open	+5.487	-0.00206	+5.488
0.700	+0.06685	-0.00208	+0.06685
0.600	+0.04478	-0.00209	+0.04477
0.500	+0.00918	-0.00209	+0.00918
0.433	+0.00174	-0.00210	+0.00174
0.466	+0.00465	-0.00209	+0.00466
0.533	+0.02189	-0.00209	+0.02188
0.566	+0.02920	-0.00209	+0.02928
0.666	+0.08282	-0.00209	–
0.8	+0.11715	-0.00208	+0.11714
0.9	+0.13007	-0.00209	+0.13006
1.0	+0.08199	-0.00209	+0.08199
1.1	+0.01315	-0.00209	+0.01314
Open	+5.475	-0.00208	–

Note. Distance from source: 107 cm from detector

TABLE A-III. – NOMINAL AND MEASURED CENTER WAVELENGTH VALUES OF NARROWBAND OCLI FILTERS

Wavelength λ, nm	
Nominal	Measured
0.433	0.433
0.466	0.474
0.500	0.506
0.533	0.538
0.566	0.553
0.600	0.605
0.666	0.673
0.700	0.705
0.8	0.790
0.9	0.885
1.0	0.995
1.1	1.095

TABLE A-IV. – IRRADIANCE AT REFERENCE DETECTOR FROM GAMMA SCIENTIFIC IRRADIANCE SOURCE AND TEST PATTERN ILLUMINATION SOURCE

λ, nm	$H_{gamma, (\lambda)}$ $\mu W/cm^2$-nm	$H_{5.1 \times 5.1 \text{ cm } (\lambda)}$, $\mu W/cm^2$-nm	Ratio
0.433	0.0197	0.0086	0.435
0.474	0.0260	0.0125	0.482
0.506	0.0370	0.0204	0.552
0.538	0.0482	0.0306	0.634
0.553	0.539	0.0379	0.704
0.605	0.0748	0.0568	0.759
0.673	0.110	0.0969	0.878
0.705	0.121	0.113	0.929
0.790	0.139	0.1416	1.018
0.885	0.150	0.163	1.088
0.995	0.155	0.201	1.300
1.095	0.140	0.208	1.49

TABLE A-V. – MEASURED IRRADIANCE AT REFERENCE DETECTOR, AND CALCULATED IRRADIANCE AT SURFACE OF TEST PATTERN ILLUMINATOR

λ, nm	$H_{measured, (\lambda)}$ ($\mu W/cm^2$-nm)	$H_{surface, (\lambda)}$ ($\mu W/cm^2$-nm)
443	0.0086	8.81
474	0.0125	12.81
506	0.0204	20.90
538	0.0306	31.36
553	0.0379	38.84
605	0.0568	58.20
673	0.0969	99.29
705	0.113	115.79
790	0.142	145.50
885	0.163	167.02
995	0.201	205.96
1095	0.208	213.13

APPENDIX B

ANALYSIS OF BROAD-BAND PERFORMANCE OF PHOTOTRANSISTOR PHOTO-IMAGING SYSTEM IN SPACE APPLICATION

Run 1	Spacecraft Spin Rate = 5 rpm
Run 2	Spacecraft Spin Rate = 3.5 rpm
Run 3	Spacecraft Spin Rate = 2 rpm

TABLE B-I. — SIGNAL-TO-NOISE RATIO ON JUPITER, IO, AND EUROPA WITH SPACECRAFT SPIN RATE OF 5 rpm (RUN 1)

THE OPTICS HAVE AN F/# OF 1.23 AND TRANS OF .54
AND THE INTEGRATION TIME IS .405 M-SEC

DARK NOISE, PHOTOELECTRONS RMS = 789.29411

THIS CASE CONSIDERS JUPITER WITH ALBEDO AT 0.525 U OF .51
WITH 5.2AU SOLAR DISTANCE AND .785RAD PHASE ANGLE

MODULATION CONTRAST	REFLECT DIFFERENCE	PK-PK SIGNAL PHOTOELECTRONS	RMS NOISE	S/N RATIO (PK-PK/RSS) AT 0 LPM	AT 32.8 LPM
1.000	1.020	441774	1218	363	80
.500	.510	220887	1218	181	40
.250	.255	110443	1218	91	20
.100	.102	44177	1218	36	8
.050	.051	22089	1218	18	4

QUANTIZATION NOISE,PHOTOELECTRONS RMS= 890.03743

THIS CASE CONSIDERS IO WITH ALBEDO AT 0.525 U OF .92
WITH 5.2AU SOLAR DISTANCE AND .785RAD PHASE ANGLE

MODULATION CONTRAST	REFLECT DIFFERENCE	PK-PK SIGNAL PHOTOELECTRONS	RMS NOISE	S/N RATIO (PK-PK/RSS) AT 0 LPM	AT 32.8 LPM
1.000	1.840	859312	1308	657	145
.500	.920	429656	1308	329	72
.250	.460	214828	1308	164	36
.100	.184	85931	1308	66	14
.050	.092	42966	1308	33	7

QUANTIZATION NOISE,PHOTOELECTRONS RMS= 890.03743

THIS CASE CONSIDERS EUROPA WITH ALBEDO AT 0.525 U OF .85
WITH 5.2AU SOLAR DISTANCE AND .785RAD PHASE ANGLE

MODULATION CONTRAST	REFLECT DIFFERENCE	PK-PK SIGNAL PHOTOELECTRONS	RMS NOISE	S/N RATIO (PK-PK/RSS) AT 0 LPM	AT 32.8 LPM
1.000	1.700	793929	1293	614	135
.500	.850	396965	1293	307	68
.250	.425	198482	1293	153	34
.100	.170	79393	1293	61	14
.050	.085	39696	1293	31	7

QUANTIZATION NOISE,PHOTOELECTRONS RMS= 890.03743

TABLE B-II. — SIGNAL-TO-NOISE RATIO ON SATURN, TITAN, AND URANUS WITH SPACECRAFT SPIN RATE OF 5 rpm (RUN 1)

THIS CASE CONSIDERS SATURN WITH ALBEDO AT 0.525 U OF .44
WITH 9.5AU SOLAR DISTANCE AND .785RAD PHASE ANGLE

MODULATION CONTRAST	REFLECT DIFFERENCE	PK-PK SIGNAL PHOTOELECTRONS	RMS NOISE	S/N RATIO (PK-PK/RSS) AT 0 LPM	AT 32.8 LPM
1.000	.880	111277	1148	97	21
.500	.440	55639	1148	48	11
.250	.220	27819	1148	24	5
.100	.088	11128	1148	10	2
.050	.044	5564	1148	5	1

QUANTIZATION NOISE,PHOTOELECTRONS RMS= 890.03743

THIS CASE CONSIDERS TITAN WITH ALBEDO AT 0.525 U OF .34
WITH 9.5AU SOLAR DISTANCE AND .785RAD PHASE ANGLE

MODULATION CONTRAST	REFLECT DIFFERENCE	PK-PK SIGNAL PHOTOELECTRONS	RMS NOISE	S/N RATIO (PK-PK/RSS) AT 0 LPM	AT 32.8 LPM
1.000	.680	94352	1145	82	18
.500	.340	47176	1145	41	9
.250	.170	23588	1145	21	5
.100	.068	9435	1145	8	2
.050	.034	4718	1145	4	1

QUANTIZATION NOISE,PHOTOELECTRONS RMS= 890.03743

THIS CASE CONSIDERS URANUS WITH ALBEDO AT 0.525 U OF .55
WITH19.2AU SOLAR DISTANCE AND .785RAD PHASE ANGLE

MODULATION CONTRAST	REFLECT DIFFERENCE	PK-PK SIGNAL PHOTOELECTRONS	RMS NOISE	S/N RATIO (PK-PK/RSS) AT 0 LPM	AT 32.8 LPM
1.000	1.100	24431	1131	22	5
.500	.550	12215	1131	11	2
.250	.275	6108	1131	5	1
.100	.110	2443	1131	2	0
.050	.055	1222	1131	1	0

QUANTIZATION NOISE,PHOTOELECTRONS RMS= 890.03743

TABLE B-III. – SIGNAL-TO-NOISE RATIO ON JUPITER, IO, AND EUROPA WITH SPACECRAFT SPIN RATE OF 3.5 rpm (RUN 2)

THE OPTICS HAVE AN F/# OF 1.23 AND TRANS OF .54
AND THE INTEGRATION TIME IS .580 M-SEC

DARK NOISE, PHOTOELECTRONS RMS = 789.29411

THIS CASE CONSIDERS JUPITER WITH ALBEDO AT 0.525 U OF .51
WITH 5.2AU SOLAR DISTANCE AND .785RAD PHASE ANGLE

MODULATION CONTRAST	REFLECT DIFFERENCE	PK-PK SIGNAL PHOTOELECTRONS	RMS NOISE	S/N RATIO (PK-PK/RSS) AT 0 LPM	AT 32.8 LPM
1.000	1.020	638664	1259	503	111
.500	.510	316332	1259	251	55
.250	.255	158166	1259	126	28
.100	.102	63266	1259	50	11
.050	.051	31633	1259	25	6

QUANTIZATION NOISE,PHOTOELECTRONS RMS= 890.03743

THIS CASE CONSIDERS IO WITH ALBEDO AT 0.525 U OF .93
WITH 5.2AU SOLAR DISTANCE AND .785RAD PHASE ANGLE

MODULATION CONTRAST	REFLECT DIFFERENCE	PK-PK SIGNAL PHOTOELECTRONS	RMS NOISE	S/N RATIO (PK-PK/RSS) AT 0 LPM	AT 32.8 LPM
1.000	1.840	1230619	1389	886	195
.500	.920	615310	1389	443	97
.250	.460	307655	1389	221	49
.100	.184	123062	1389	89	19
.050	.092	61531	1389	44	10

QUANTIZATION NOISE,PHOTOELECTRONS RMS= 890.03743

THIS CASE CONSIDERS EUROPA WITH ALBEDO AT 0.525 U OF .85
WITH 5.2AU SOLAR DISTANCE AND .785RAD PHASE ANGLE

MODULATION CONTRAST	REFLECT DIFFERENCE	PK-PK SIGNAL PHOTOELECTRONS	RMS NOISE	S/N RATIO (PK-PK/RSS) AT 0 LPM	AT 32.8 LPM
1.000	1.700	1136995	1368	831	183
.500	.850	568493	1368	415	91
.250	.425	284246	1368	208	46
.100	.170	113699	1368	83	18
.050	.085	56849	1368	42	9

QUANTIZATION NOISE,PHOTOELECTRONS RMS= 890.03743

TABLE B-IV. — SIGNAL-TO-NOISE RATIO ON SATURN, TITAN URANUS WITH SPACECRAFT SPIN RATE OF 3.5 rpm (RUN 2)

THIS CASE CONSIDERS SATURN WITH ALBEDO AT 0.525 U OF .44
WITH 9.5AU SOLAR DISTANCE AND .785RAD PHASE ANGLE

MODULATION CONTRAST	REFLECT DIFFERENCE	PK-PK SIGNAL PHOTOELECTRONS	RMS NOISE	S/N RATIO (PK-PK/RSS) AT 0 LPM	AT 32.8 LPM
1.000	.880	159360	1158	138	30
.500	.440	79680	1158	69	15
.250	.220	39840	1158	34	8
.100	.088	15936	1158	14	3
.050	.044	7968	1158	7	2

QUANTIZATION NOISE,PHOTOELECTRONS RMS= 890.03743

THIS CASE CONSIDERS TITAN WITH ALBEDO AT 0.525 U OF .34
WITH 9.5AU SOLAR DISTANCE AND .785RAD PHASE ANGLE

MODULATION CONTRAST	REFLECT DIFFERENCE	PK-PK SIGNAL PHOTOELECTRONS	RMS NOISE	S/N RATIO (PK-PK/RSS) AT 0 LPM	AT 32.8 LPM
1.000	.680	135128	1153	117	26
.500	.340	67561	1153	59	13
.250	.170	33780	1153	29	6
.100	.068	13512	1153	12	3
.050	.034	6756	1153	6	1

QUANTIZATION NOISE,PHOTOELECTRONS RMS= 890.03743

THIS CASE CONSIDERS URANUS WITH ALBEDO AT 0.525 U OF .55
WITH19.2AU SOLAR DISTANCE AND .785RAD PHASE ANGLE

MODULATION CONTRAST	REFLECT DIFFERENCE	PK-PK SIGNAL PHOTOELECTRONS	RMS NOISE	S/N RATIO (PK-PK/RSS) AT 0 LPM	AT 32.8 LPM
1.000	1.100	34987	1133	31	7
.500	.550	17493	1133	15	3
.250	.275	8747	1133	8	2
.100	.110	3499	1133	3	1
.050	.055	1749	1133	2	0

QUANTIZATION NOISE,PHOTOELECTRONS RMS= 890.03743

TABLE B-V. — SIGNAL-TO-NOISE RATIO ON JUPITER, IO, AND EUROPA WITH SPACECRAFT SPIN RATE OF 2 rpm (RUN 3)

THE OPTICS HAVE AN F/# OF 1.23 AND TRANS OF .54
AND THE INTEGRATION TIME IS 1.010 M-SEC

DARK NOISE, PHOTOELECTRONS RMS = 789.29411

THIS CASE CONSIDERS JUPITER WITH ALBEDO AT 0.525 U OF .51
WITH 5.2AU SOLAR DISTANCE AND .785RAD PHASE ANGLE

MODULATION CONTRAST	REFLECT DIFFERENCE	PK-PK SIGNAL PHOTOELECTRONS	RMS NOISE	S/N RATIO (PK-PK/RSS) AT 0 LPM	AT 32.8 LPM
1.000	1.020	1101707	1361	810	178
.500	.510	550854	1361	405	89
.250	.255	275427	1361	202	45
.100	.102	110171	1361	81	18
.050	.051	55085	1361	40	9

QUANTIZATION NOISE, PHOTOELECTRONS RMS= 890.03743

THIS CASE CONSIDERS IO WITH ALBEDO AT 0.525 U OF .92
WITH 5.2AU SOLAR DISTANCE AND .785RAD PHASE ANGLE

MODULATION CONTRAST	REFLECT DIFFERENCE	PK-PK SIGNAL PHOTOELECTRONS	RMS NOISE	S/N RATIO (PK-PK/RSS) AT 0 LPM	AT 32.8 LPM
1.000	1.840	2142975	1591	1347	296
.500	.920	1071487	1591	674	148
.250	.460	535744	1591	337	74
.100	.184	214297	1591	135	30
.050	.092	107149	1591	67	15

QUANTIZATION NOISE, PHOTOELECTRONS RMS= 890.03743

THIS CASE CONSIDERS EUROPA WITH ALBEDO AT 0.525 U OF .85
WITH 5.2AU SOLAR DISTANCE AND .785RAD PHASE ANGLE

MODULATION CONTRAST	REFLECT DIFFERENCE	PK-PK SIGNAL PHOTOELECTRONS	RMS NOISE	S/N RATIO (PK-PK/RSS) AT 0 LPM	AT 32.8 LPM
1.000	1.700	1379923	1555	1273	280
.500	.850	989961	1555	637	140
.250	.425	494981	1555	319	70
.100	.170	197992	1555	127	28
.050	.085	98996	1555	64	14

QUANTIZATION NOISE, PHOTOELECTRONS RMS= 890.03743

TABLE B-VI. — SIGNAL-TO-NOISE RATIO ON SATURN, TITAN, AND URANUS WITH SPACECRAFT SPIN RATE OF 2 rpm (RUN 3)

THIS CASE CONSIDERS SATURN WITH ALBEDO AT 0.525 U OF .44
WITH 9.5AU SOLAR DISTANCE AND .785RAD PHASE ANGLE

MODULATION CONTRAST	REFLECT DIFFERENCE	PK-PK SIGNAL PHOTOELECTRONS	RMS NOISE	S/N RATIO (PK-PK/RSS) AT 0 LPM	AT 32.8 LPM
1.000	.880	277507	1183	235	52
.500	.440	138753	1183	117	26
.250	.220	69377	1183	59	13
.100	.088	27751	1183	23	5
.050	.044	13875	1183	12	3

QUANTIZATION NOISE,PHOTOELECTRONS RMS= 990.03743

THIS CASE CONSIDERS TITAN WITH ALBEDO AT 0.525 U OF .34
WITH 9.5AU SOLAR DISTANCE AND .785RAD PHASE ANGLE

MODULATION CONTRAST	REFLECT DIFFERENCE	PK-PK SIGNAL PHOTOELECTRONS	RMS NOISE	S/N RATIO (PK-PK/RSS) AT 0 LPM	AT 32.8 LPM
1.000	.680	235298	1174	200	44
.500	.340	117649	1174	100	22
.250	.170	58824	1174	50	11
.100	.068	23530	1174	20	4
.050	.034	11765	1174	10	2

QUANTIZATION NOISE,PHOTOELECTRONS RMS= 990.03743

THIS CASE CONSIDERS URANUS WITH ALBEDO AT 0.525 U OF .55
WITH19.2AU SOLAR DISTANCE AND .785RAD PHASE ANGLE

MODULATION CONTRAST	REFLECT DIFFERENCE	PK-PK SIGNAL PHOTOELECTRONS	RMS NOISE	S/N RATIO (PK-PK/RSS) AT 0 LPM	AT 32.8 LPM
1.000	1.100	60926	1138	54	12
.500	.550	30463	1138	27	6
.250	.275	15231	1138	13	3
.100	.110	6093	1138	5	1
.050	.055	3046	1138	3	1

QUANTIZATION NOISE,PHOTOELECTRONS RMS= 990.03743

APPENDIX C

ANALYSIS OF PERFORMANCE OF EXPERIMENTAL PHOTOTRANSISTOR PHOTO-IMAGING SYSTEM IN THE LABORATORY

This appendix lists the results of a performance analysis of the experimental model of the photo-imaging system using a simplified analytical model of the system.

The objective of this analysis is to determine the increase in apparent planet radiance required to obtain the same signal-to-noise ratios as the flight model. (This approach is discussed in detail in Section 7.2.3.) The following notes apply to the analyses:

1. Exposure time used in all runs is 4.8 ms.
2. Run 1 uses a test pattern radiance level corresponding to the radiance of the planets and satellites in space (Jupiter, Io, Europa, Saturn, Titan, and Uranus).
3. Run 2 uses a test pattern radiance level 4.5 times higher than the radiance of the planets and satellites in space (Jupiter, Io, Europa).
4. Run 3 uses a test pattern radiance level 11 times higher than the radiance of the planets and satellites in space (Saturn, Titan, and Uranus).

RUN 1

THE OPTICS HAVE AN F/# OF 4.40 AND TRANS OF .35
AND THE INTEGRATION TIME IS 4.800 M-SEC

DARK NOISE, PHOTOELECTRONS RMS = 789.29411

THIS CASE CONSIDERS JUPITER WITH ALBEDO AT 0.525U OF .51
WITH 5.2AU SOLAR DISTANCE AND .785RAD PHASE ANGLE

MODULATION CONTRAST	REFLECT DIFFERENCE	PK-PK SIGNAL PHOTOELECTRONS	RMS NOISE	S/N RATIO (PK-PK/RSS) AT 0 LPM	AT 32.8 LPM
1.000	1.020	85138	1010	84	19
.500	.510	42569	1010	42	9
.250	.255	21284	1010	21	5
.100	.102	8514	1010	8	2
.050	.051	4257	1010	4	1

QUANTIZATION NOISE,PHOTOELECTRONS RMS= 445.01872
PLANET IRRADIANCE INCREASED BY FACTOR OF 1
OBJECT RADIANCE, W/SQ.METER-STER(0.5-0.6U)= .852

THIS CASE CONSIDERS IO WITH ALBEDO AT 0.525U OF .92
WITH 5.2AU SOLAR DISTANCE AND .785RAD PHASE ANGLE

MODULATION CONTRAST	REFLECT DIFFERENCE	PK-PK SIGNAL PHOTOELECTRONS	RMS NOISE	S/N RATIO (PK-PK/RSS) AT 0 LPM	AT 32.8 LPM
1.000	1.840	147902	1025	144	32
.500	.920	73951	1025	72	16
.250	.460	36975	1025	36	8
.100	.184	14790	1025	14	3
.050	.092	7395	1025	7	2

QUANTIZATION NOISE,PHOTOELECTRONS RMS= 445.01872
PLANET IRRADIANCE INCREASED BY FACTOR OF 1
OBJECT RADIANCE, W/SQ.METER-STER(0.5-0.6U)= 1.479

THIS CASE CONSIDERS EUROPA WITH ALBEDO AT 0.525U OF .85
WITH 5.2AU SOLAR DISTANCE AND .785RAD PHASE ANGLE

MODULATION CONTRAST	REFLECT DIFFERENCE	PK-PK SIGNAL PHOTOELECTRONS	RMS NOISE	S/N RATIO (PK-PK/RSS) AT 0 LPM	AT 32.8 LPM
1.000	1.700	136648	1022	134	29
.500	.850	68324	1022	67	15
.250	.425	34162	1022	33	7
.100	.170	13665	1022	13	3
.050	.085	6832	1022	7	1

QUANTIZATION NOISE,PHOTOELECTRONS RMS= 445.01872
PLANET IRRADIANCE INCREASED BY FACTOR OF 1
OBJECT RADIANCE, W/SQ.METER-STER(0.5-0.6U)= 1.366

RUN 1 (Concluded)

THIS CASE CONSIDERS SATURN WITH ALBEDO AT 0.525U OF .44
WITH 9.5AU SOLAR DISTANCE AND .785RAD PHASE ANGLE

MODULATION CONTRAST	REFLECT DIFFERENCE	PK-PK SIGNAL PHOTOELECTRONS	RMS NOISE	S/N RATIO (PK-PK/RSS) AT 0 LPM	AT 32.8 LPM
1.000	.880	21951	994	22	5
.500	.440	10976	994	11	2
.250	.220	5488	994	6	1
.100	.088	2195	994	2	0
.050	.044	1098	994	1	0

QUANTIZATION NOISE,PHOTOELECTRONS RMS= 445.01872
PLANET IRRADIANCE INCREASED BY FACTOR OF 1
OBJECT RADIANCE, W/SQ.METER-STER(0.5-0.6U)= .220

THIS CASE CONSIDERS TITAN WITH ALBEDO AT 0.525U OF .34
WITH 9.5AU SOLAR DISTANCE AND .785RAD PHASE ANGLE

MODULATION CONTRAST	REFLECT DIFFERENCE	PK-PK SIGNAL PHOTOELECTRONS	RMS NOISE	S/N RATIO (PK-PK/RSS) AT 0 LPM	AT 32.8 LPM
1.000	.680	16240	992	16	4
.500	.340	8120	992	8	2
.250	.170	4060	992	4	1
.100	.068	1624	992	2	0
.050	.034	812	992	1	0

QUANTIZATION NOISE,PHOTOELECTRONS RMS= 445.01872
PLANET IRRADIANCE INCREASED BY FACTOR OF 1
OBJECT RADIANCE, W/SQ.METER-STER(0.5-0.6U)= .162

THIS CASE CONSIDERS URANUS WITH ALBEDO AT 0.525U OF .55
WITH19.2AU SOLAR DISTANCE AND .785RAD PHASE ANGLE

MODULATION CONTRAST	REFLECT DIFFERENCE	PK-PK SIGNAL PHOTOELECTRONS	RMS NOISE	S/N RATIO (PK-PK/RSS) AT 0 LPM	AT 32.8 LPM
1.000	1.100	5533	990	6	1
.500	.550	2766	990	3	1
.250	.275	1383	990	1	0
.100	.110	553	990	1	0
.050	.055	277	990	0	0

QUANTIZATION NOISE,PHOTOELECTRONS RMS= 445.01872
PLANET IRRADIANCE INCREASED BY FACTOR OF 1
OBJECT RADIANCE, W/SQ.METER-STER(0.5-0.6U)= .055

RUN 2

THE OPTICS HAVE AN F/# OF 4.40 AND TRANS OF .35
AND THE INTEGRATION TIME IS 4.800 M-SEC

DARK NOISE, PHOTOELECTRONS RMS = 789.29411

THIS CASE CONSIDERS JUPITER WITH ALBEDO AT 0.525U OF .51
WITH 5.2AU SOLAR DISTANCE AND .785RAD PHASE ANGLE

MODULATION CONTRAST	REFLECT DIFFERENCE	PK-PK SIGNAL PHOTOELECTRONS	RMS NOISE	S/N RATIO (PK-PK/RSS) AT 0 LPM	AT 32.8 LPM
1.000	1.020	383119	1081	354	79
.500	.510	191560	1081	177	39
.250	.255	95780	1081	89	19
.100	.102	38312	1081	35	8
.050	.051	19156	1081	18	4

QUANTIZATION NOISE,PHOTOELECTRONS RMS= 445.01872
PLANET IRRADIANCE INCREASED BY FACTOR OF 4.5
OBJECT RADIANCE, W/SQ.METER-STER(0.5-0.6U)= 3.834

THIS CASE CONSIDERS IO WITH ALBEDO AT 0.525U OF .92
WITH 5.2AU SOLAR DISTANCE AND .785RAD PHASE ANGLE

MODULATION CONTRAST	REFLECT DIFFERENCE	PK-PK SIGNAL PHOTOELECTRONS	RMS NOISE	S/N RATIO (PK-PK/RSS) AT 0 LPM	AT 32.8 LPM
1.000	1.840	665558	1144	582	128
.500	.920	332779	1144	291	64
.250	.460	166390	1144	145	32
.100	.184	66556	1144	58	13
.050	.092	33278	1144	29	6

QUANTIZATION NOISE,PHOTOELECTRONS RMS= 445.01872
PLANET IRRADIANCE INCREASED BY FACTOR OF 4.5
OBJECT RADIANCE, W/SQ.METER-STER(0.5-0.6U)= 6.654

THIS CASE CONSIDERS EUROPA WITH ALBEDO AT 0.525U OF .85
WITH 5.2AU SOLAR DISTANCE AND .785RAD PHASE ANGLE

MODULATION CONTRAST	REFLECT DIFFERENCE	PK-PK SIGNAL PHOTOELECTRONS	RMS NOISE	S/N RATIO (PK-PK/RSS) AT 0 LPM	AT 32.8 LPM
1.000	1.700	614918	1133	543	119
.500	.850	307459	1133	271	60
.250	.425	153729	1133	136	30
.100	.170	61492	1133	54	12
.050	.085	30746	1133	27	6

QUANTIZATION NOISE,PHOTOELECTRONS RMS= 445.01872
PLANET IRRADIANCE INCREASED BY FACTOR OF 4.5
OBJECT RADIANCE, W/SQ.METER-STER(0.5-0.6U)= 6.148

RUN 3

THE OPTICS HAVE AN F/# OF 4.40 AND TRANS OF .35
AND THE INTEGRATION TIME IS 4.800 M-SEC

DARK NOISE, PHOTOELECTRONS RMS = 789.29411

THIS CASE CONSIDERS SATURN WITH ALBEDO AT 0.525U OF .44
WITH 9.5AU SOLAR DISTANCE AND .785RAD PHASE ANGLE

MODULATION CONTRAST	REFLECT DIFFERENCE	PK-PK SIGNAL PHOTOELECTRONS	RMS NOISE	S/N RATIO (PK-PK/RSS) AT 0 LPM	AT 32.8 LPM
1.000	.880	241465	1048	230	51
.500	.440	120733	1048	115	25
.250	.220	60366	1048	58	13
.100	.088	24147	1048	23	5
.050	.044	12073	1048	12	3

QUANTIZATION NOISE,PHOTOELECTRONS RMS= 445.01872
PLANET IRRADIANCE INCREASED BY FACTOR OF 11
OBJECT RADIANCE, W/SQ.METER-STER(0.5-0.6U)= 2.416

THIS CASE CONSIDERS TITAN WITH ALBEDO AT 0.525U OF .34
WITH 9.5AU SOLAR DISTANCE AND .785RAD PHASE ANGLE

MODULATION CONTRAST	REFLECT DIFFERENCE	PK-PK SIGNAL PHOTOELECTRONS	RMS NOISE	S/N RATIO (PK-PK/RSS) AT 0 LPM	AT 32.8 LPM
1.000	.680	178635	1033	173	38
.500	.340	89318	1033	87	19
.250	.170	44659	1033	43	10
.100	.068	17864	1033	17	4
.050	.034	8932	1033	9	2

QUANTIZATION NOISE,PHOTOELECTRONS RMS= 445.01872
PLANET IRRADIANCE INCREASED BY FACTOR OF 11
OBJECT RADIANCE, W/SQ.METER-STER(0.5-0.6U)= 1.786

THIS CASE CONSIDERS URANUS WITH ALBEDO AT 0.525U OF .55
WITH19.2AU SOLAR DISTANCE AND .785RAD PHASE ANGLE

MODULATION CONTRAST	REFLECT DIFFERENCE	PK-PK SIGNAL PHOTOELECTRONS	RMS NOISE	S/N RATIO (PK-PK/RSS) AT 0 LPM	AT 32.8 LPM
1.000	1.100	60863	1004	61	13
.500	.550	30431	1004	30	7
.250	.275	15216	1004	15	3
.100	.110	6086	1004	6	1
.050	.055	3043	1004	3	1

QUANTIZATION NOISE,PHOTOELECTRONS RMS= 445.01872
PLANET IRRADIANCE INCREASED BY FACTOR OF 11
OBJECT RADIANCE, W/SQ.METER-STER(0.5-0.6U)= .606

APPENDIX D

CALCULATION OF INTEGRATED IRRADIANCE OF ILLUMINATOR, SCALE FACTORS FOR ESTABLISHING INCANDESCENT ILLUMINATOR RADIANCE LEVELS, AND EXPOSURE ON PHOTO-TRANSISTOR ARRAYS FROM ILLUMINATOR

This computer program is used to compute the scale factors for establishing the radiance levels of the test patterns used in laboratory tests. This subject is discussed in Section 7.2.4. The program is used to obtain solutions to the three equations defined in Table XXIII for computations of the scale factors. In addition, the program computes the integrated irradiance level of the illuminator, using equation (7-1) of Section 7.2.4; and it also computes the exposure on the phototransistor array from the illuminator by the use of equation (7-2) of Section 7.2.4. The symbols used in these equations are defined in Section 3.0 of this report. Corresponding symbols used in the computer program are defined in lines 150 through 320 of the program.

The organization of the program is as follows:

a. Lines 700 to 785 contain data entries for the program. Sources of these data have been defined in the text of Section 7.2.4

b. The terms of the numerator of equation (1) of Table XXIII are contained in lines 800 and 870, and the denominator is contained in line 886 of the program

c. The terms of the numerator of equation (2) of the table are contained in lines 810 and 910, and the denominator is contained in line 920 of the program

d. Equation (3) of the table is contained in line 1000 of the program

e. Equation (7-1) of Section 7.2.4 is contained in line 937 of the program

f. Equation (7-2) of Section 7.2.4 is contained in line 1200 of the program.

A printout and a run of the program appears in this appendix.

RUN 1

```
100 REM PROGRAM, NORM 24
110 REM  PROGRAM COMPUTES SCALE FACTOR OF ILLUMINATOR IRRADIANCE
120 REM      TO EQUIVALENT SOLAR IRRADIANCE
130 REM    ALSO COMPUTES EXPOSURE ON ARRAY FROM ILLUMINATOR
135 REM      IN MICROJOULES/ SQ. METER
140 REM  **********DEFINITION OF SYMBOLS AND UNITS*********
150 REM A = AREA OF DETECTOR ELEMENT IN SQ. METERS
160 REM T1= EXPOSURE TIME IN SECONDS
180 REM F1= EFFECTIVE FOCAL RATIO IN LAB TESTS
190 REM H = PLANCK'S CONSTANT, IN JOULE-SECONDS
200 REM C= VELOCITY OF LIGHT IN MICRONS/SECOND
210 REM H(I)=SOLAR SPECTRAL IRRADIANCE(1 SOLAR CONST.),W/SQ.M.-20 NM
215 REM R$(I,J)=SPECTRAL ALBEDO OF PLANET OR SATELLITE
220 REM S(I)=ILLUMINATOR SPECTRAL IRRADIANCE, W/SQ.M.-20NM
230 REM T(I)=OPTICAL TRANSMISSION OF CAMERA(SQ. PASSBAND,0.5-0.9U)
240 REM L(I)=OPTICAL TRANSMISSION OF CAMERA(TRUE SPECTRAL PASSBAND)
260 REM E(I)=SPECTRAL QUANTUM EFFICIENCY OF PHOTOTRANSISTORS
270 REM W(I)=WAVELENGTH IN MICRONS
280 REM N1=PHOTOELECTRONS/UNIT OF SOLAR SOURCE IRRADIANCE(.5-.6 U)
290 REM N9=PHOTOELECTRONS/UNIT OF ILLLUMINATOR IRRADIANCE(.5-.7 U)
300 REM R(I)=SCALE FACTOR,ILLUMINATOR/PLANETARY RADIANCE
310 REM E= EXPOSURE ON PHOTOTRANSISTOR ARRAY FROM ILLUMINATOR
320 REM    WITHOUT TEST PATTERN OR N. D. FILTERS, IN U-JOULES/SQ. M.
400 DIM H(10),S(10),T(10),L(10),E(10),W(10)
401 DIM R$(6,10)
402 DIM Z(6)
410 A=412 E-12
420 T1=4.8 E-3
440 F1=4.4
450 H=6.624 E-34
460 C=3.0 E14
500 FOR I=1 TO 10
510 READ H(I)
520 NEXT I
530 FOR I=1 TO 10
540 READ T(I)
550 NEXT I
560 FOR I= 1 TO 10
570 READ E(I)
580 NEXT I
590 FOR I=1 TO 10
600 READ W(I)
610 NEXT I
620 FOR I=1 TO 10
630 READ S(I)
640 NEXT I
650 FOR I= 1 TO 10
660 READ L(I)
670 NEXT I
671 FOR I=1 TO 6
672 FOR J=1 TO 10
673 READ R$(I,J)
674 NEXT J
675 NEXT I
700 DATA 38.9,39.2,39.0,38.2,37.9,  35.7,34.2,33.0,32.1,30.3
710 DATA .35,.35,.35,.35,.35,        0,0,0,0,0
720 DATA .69,.67,.65,.62,.59,         .56,.53,.50,.46,.43
730 DATA .51,.53,.55,.57,.59,         .61,.63,.65,.67,.69
740 DATA 4.4,5.6,7.0,8.4,10.4,        12.4,14.4,16.6,18.8,20.8
750 DATA .103,.235,.314,.359,.322,   .213,.150,.094,.058,.017
760 DATA .50,.52,.53,.54,.55,       .55,.54,.53,.50,.47
765 DATA .92,.92,.92,.92,.92,        .92,.92,.92,.92,.92
770 DATA .85,.85,.85,.85,.85,        .85,.85,.85,.85,.85
775 DATA .42,.44,.46,.47,.48,         .48,.47,.45,.43,.41
780 DATA .32,.32,.32,.32,.32,         .32,.32,.32,.32,.32
785 DATA .56,.50,.44,.38,.32,          .28,.23,.20,.16,.12
```

RUN 1 (Concluded)

```
800 K1=(A*T1)/(4*F1*F1*H*C)
860 FOR I=1 TO 6
862 H1=0
865 FOR J=1 TO 5
870 H1=H1+H(J)*R$(I,J)*T(J)*E(J)*W(J)
872 NEXT J
876 Z(I)=H1
880 NEXT I
883 FOR I=1 TO 6
884 H2=0
885 FOR J=1 TO 5
886 H2=H2+H(J)*R$(I,J)
887 NEXT J
889 X(I)=H2
891 NEXT I
895 S1=0
896 S2=0
900 FOR K=1 TO 10
910 S1=S1+S(K)*L(K)*E(K)*W(K)
920 S2=S2+S(K)
930 NEXT K
935 H3=0
936 FOR I=1 TO 5
937 H3=H3+H(I)
938 NEXT I
940 PRINT"SOLAR IRRADIANCE,ONE SOLAR CONSTANT,0.5-0.6U=",H3
950 PRINT "ILLUMINATOR IRRADIANCE, 0.5-0.7 U=",S2
990 FOR I=1 TO 6
1000 R(I)=(Z(I)/X(I))/(S1/S2)
1010 NEXT I
1018 PRINT "RATIO OF 2860 K RADIATION(.5-.7U)/PLANET RADIATION(.5-.6U)"
1019 PRINT "    TO GENERATE SAME NUMBER OF PHOTOELECTRONS IN LAB SENSOR"
1020 PRINT "          AS IN FLIGHT MODEL OF SENSOR"
1021 PRINT "    FOR JUPITER,   IO,  EUROPA,  SATURN,  TITAN, URANUS"
1022 Z="      %.%%%    %.%%%  %.%%%    %.%%%   %.%%%   %.%%%"
1023 PRINT IN IMAGE Z: R(1),R(2),R(3),R(4),R(5),R(6)
1200 E=(K1*S1)/660
1300 PRINT "EXPOSURE ON ARRAY FROM ILLUMINATOR,U-JOULES/SQ.M =",E
1400 END
```

```
$ RUN
SOLAR IRRADIANCE,ONE SOLAR CONSTANT,0.5-0.6U=  193.2
ILLUMINATOR IRRADIANCE, 0.5-0.7 U=             118.8
RATIO OF 2860 K RADIATION(.5-.7U)/PLANET RADIATION(.5-.6U)
    TO GENERATE SAME NUMBER OF PHOTOELECTRONS IN LAB SENSOR
          AS IN FLIGHT MODEL OF SENSOR
    FOR JUPITER,   IO,  EUROPA,  SATURN,  TITAN, URANUS
      2.363    2.363  2.363    2.363   2.363   2.365
EXPOSURE ON ARRAY FROM ILLUMINATOR,U-JOULES/SQ.M =          1210.2319
```

APPENDIX E

CALIBRATION OF THE OPTICAL TRANSMISSION OF NEUTRAL DENSITY FILTERS USED FOR GRAY-SCALE CALIBRATION OF THE EXPERIMENTAL PHOTO-IMAGING SENSOR

The accompanying table lists the measured transmission of the photographic film used as neutral density filters in the solid state camera tests. The measurements were made at three wavelengths, using a double quartz prism monochromator and a silicon solar cell detector. Measurements were made of the solar cell output with no filter, and with the filter in front of the exit slit of the monochromator. The zero offset of the detector/preamplifier system was measured in each instance. The transmission was taken as the ratio of the detector output with and without filters in place.

The results show reasonable spectral flatness up to a measured density of about 1.0, with progressively larger deviations across the band for higher measured densities. Estimated errors of measurements are indicated. These estimates are based on the resolution of the digital voltmeter, since this, rather than noise, seeemed to be the limitation.

TABLE E-I. – OPTICAL TRANSMISSION OF NEUTRAL DENSITY FILTERS

Nominal Density	Wavelength λ, μ	T	D	Estimated Uncertainty in T, %
0.2	0.50	0.543	0.26	±0.5
	0.55	0.549	0.26	±0.2
	0.60	0.548	0.26	±0.2
0.4	0.50	0.291	0.54	±1
	0.55	0.284	0.55	±0.4
	0.60	0.286	0.54	±0.3
0.6	0.50	0.161	0.79	±2
	0.55	0.156	0.80	±1
	0.60	0.151	0.82	±0.3
0.8	0.50	0.100	1.0	±2
	0.55	0.091	1.03	±1
	0.60	0.093	1.03	±0.5
1.0	0.50	0.058	1.24	±5
	0.55	0.051	1.29	±2
	0.60	0.051	1.29	±1
1.2	0.50	0.040	1.4	±6
	0.55	0.034	1.47	±2.5
	0.60	0.034	1.47	±1
1.4	0.50	0.029	1.5	±8
	0.55	0.020	1.7	±5
	0.60	0.019	1.7	±2.5
1.6	0.50	0.022	1.65	±11
	0.55	0.014	1.83	±6
	0.60	0.013	1.89	±3
1.8	0.50	0.020	1.7	±12
	0.55	0.011	1.95	±7
	0.60	0.009	2.0	±5

TABLE E-I. – OPTICAL TRANSMISSION OF NEUTRAL DENSITY FILTERS - Concluded

Nominal Density	Wavelength λ, μ	T	D	Estimated Uncertainty in T, %
2.0	0.50	0.016	1.8	±15
	0.55	0.0077	2.1	±11
	0.60	0.0057	2.2	±8
2.2	0.50	0.015	1.8	±16
	0.55	0.0064	2.2	±12
	0.60	0.0041	2.4	±10
2.4	0.50	0.015	1.8	±16
	0.55	0.0060	2.2	±12
	0.60	0.0033	2.5	±10

11.0
ACKNOWLEDGMENTS

The cooperative support of the following personnel in support of this program is acknowledged:

G. F. Koester	Documentation of configuration of experimental photo-imaging system and data collection facility; direction of laboratory tests
D. L. Hall	Support of laboratory test program
J. W. Burkig	Radiometric calibration of test pattern illuminator
L. W. Hobrock	Development of flight model signal processing electronic circuit configuration
H. F. Dodge	Development of software requirements for processing of digital video data
D. G. Michaels	Computer processing of digital video data
E. R. Moore	Densimetric analysis of photographic test patterns
J. L. Nelson	Analysis of performance of experimental photo-imaging system from digital video data
C. E. Shaw	Technical writing, editing, and publication
General Dynamics, Electro Dynamic Division	Reproduction of imagery on photographic film, by laser beam film recorder